Synthesis and Characterization of Novel Composite Photoelectrodes based on Chalcopyrite and Silicon for the Visible Light-driven Hydrogen and Oxygen Evolution

vorgelegt von
Dipl.-Ing.
Anahita Azarpira
geb. in Tehran

von der Fakultät III- Prozesswissenschaften- Institut für Energietechnik
der Technischen Universität Berlin
zur Erlangung des akademischen Grades

Doktor der Ingenieurwissenschaften

-Dr.-Ing.

genehmigte Dissertation

Promotionsausschuss:
Vorsitzender: Prof. Dr. John Banhart
Gutachter: Prof. Dr. Frank Behrendt
Gutachter: Assoc. Prof. Dr. Thomas Schedel-Niedrig

Tag der wissenschaftlichen aussprache: 9. May 2016

Berlin 2016

Eidesstaatliche Erklärung

Hiermit versichere ich an Eides statt, die vorliegende Arbeit selbstständig und eigenhändig angefertigt zu haben.

Anahita Azarpira
09.05.2016

Acknowledgement

First of all I would like to express my deepest gratitude to my advisors Prof. Dr. Thomas Schedel-Niedrig and Dr. Michael Lublow for their patience, motivation, enthusiasm and continuous support throughout my thesis work. Their guidance and training in research using various methods, their support in analysis, interpretation and discussions of the results, presented in this thesis, is highly appreciated.

I would like to give a heartfelt, special thanks to Dr. Michael Lublow for his detailed advice in electrochemistry and surface science. His creativity and perseverance makes him an outstanding mentor and helped me solving even most intricate problems.

I am very grateful to Prof. Dr. Frank Behrendt who made it possible to complete this work in an inspiring atmosphere. It has been an honor to be his Ph.D. student. Many valuable results were achieved and new ideas were developed during discussions in seminars under his supervision.

I would also like to thank Prof. Dr. Roel van de Krol for giving me the opportunity to realize this thesis in his department at the Helmholtz-Zentrum Berlin and Ms. Mirjam Guerra for assistance with organizational issues.

I would like to thank Dr. Peter Bogdanoff for his kind assistance for DEMS and IPCE measurements and Dr. Sebastian Fiechter for giving me detailed introduction to XRD measurements and data analysis. The assistance by Dr. Aafke Bronneberg for deposition of TiO_2 by means of ALD and by Christian Höhn and Alex Steigert for XPS measurements is highly appreciated. I appreciate very much, too, the support by Dr. Daniel Abou-Ras and Ulrike Bloeck for SEM and TEM measurements.

I am very thankful for the collaboration with all my colleagues at the Helmholtz-Zentrum Berlin who, each of them in his or her respective field, provided assistance and advice. Particularly the support given by Katarzyna Olech and Dianna Stellmach in DEMS measurements is highly appreciated.

I would also like to thank Prof. Dr. Christian Herbert-Fischer to let me work in his ILGAR laboratory. I want to thank present and former members of the ILGAR team for their support and kindness.

I am very thankful to Dr. Christian Kaufmann for providing me with chalcopyrite substrates and supporting my project with his expertise in analysis of semiconductor properties. I am deeply thankful to Prof. Dr. Matthias Driess and Johannes Pfrommer from Technical University Berlin for providing me with ZnO:Co catalyst powders.

Above all, I am extraordinarily grateful to my parents, Kian and Mohammad for believing in me and for being the mentors in my life. I deeply appreciate their efforts in raising me always in a thoughtful and warm-hearted way and making me what I am today. I deeply hope to meet always their expectations to full extent, now and in the future.

Kurzfassung

In dieser Arbeit werden effiziente und stabile Mehrschicht-Halbleiter-Elektroden beschrieben, die für die beiden Halbzellenreaktionen der lichtgestützten Wasserspaltung, d.h. die Entwicklung von Wasserstoff (HER) bzw. Sauerstoff (OER), entwickelt wurden.

Für die effiziente und stabile Entwicklung von Wasserstoff in sauren Elektrolyten wurden neuartige Photokathoden entwickelt, die hochqualitative Dünnschicht-Absorber aus $Cu(In,Ga)Se_2$ mit TiO_2-Schichten verbinden, welche zusätzlich mit Pt dotiert wurden. Variierte Konzentrationen von Pt wurden systematisch untersucht, um eine simultane Optimierung zu erzielen bzgl. i) der Leitfähigkeit der $Pt-TiO_2$- Schichten, ii) der elektrokatalytischen Aktivität und iii) der Lichteinkopplung in den Chalkopyrit Absorber. Es wird nachgewiesen, dass die graduelle Erhöhung der Pt-Konzentration durch ein Effizienz- und Stabilitäts-Maximum der resultierenden Photokathode läuft (bei etwa 5 vol. % der Pt-haltigen Präparationslösung). Bei diesem Maximum wird eine optimierte Lichteinkopplung in den Chalkopyrit-Absorber realisiert, die Photostromdichten von 15 $mAcm^{-2}$ am thermodynamischen Potential der Wasserstoffentwicklung ermöglicht. Photokathoden, die diesem Parameter entsprechend hergestellt werden, arbeiten stabil über mehr als 24 Stunden ohne Zeichen von Degradation.

Für die entsprechende Präparation von Halbleiter-basierten Photoanoden wurde das Verfahren der elektrophoretischen Abscheidung angewendet. Hiermit wurden zwei Wasseroxidationskatalysatoren, ZnO:Co und RuO_2, auf Halbleitersubstraten immobilisiert. Für die Sauerstoffentwicklung in alkalischen Lösungen wurde eine detaillierte Analyse durchgeführt, um optimale Parameter für die Abscheidung von ZnO:Co Katalysatoren auf fluoridierte Zinnoxidschichten aus verschiedenen organischen Lösungen zu bestimmen. Die nachfolgende Auswertung der elektrochemischen Aktivität zeigte eine deutliche Abhängigkeit von der verwendeten organischen Lösung mit höchster Aktivität nach Abscheidung aus Acetonitril und geringster Aktivität nach Abscheidung aus Ethanol. Die detaillierte Analyse der jeweiligen Schichten mit Hilfe verschiedener Analyseverfahren zeigte, dass die Veränderung der elektrochemischen Aktivität durch eine entsprechende Veränderung der Grösse der aktiven Oberfläche verursacht wird. Es konnte weiterhin gezeigt werden, dass die weniger aktiven aber deutlich lichtdurchlässigeren ZnO:Co-Phasen, die durch Abscheidung aus Ethanol gewonnen wurden, erfolgreich in einer kombinierten Anordnung mit einer kostensparenden Dreifach-Solarzelle verwendet werden können. Durch diese Anordnung wurde eine Effizienz von 5% in der Umwandlung von Lichtenergie in chemische Energie, d.h. Wasserstoff, erzielt. Um schliesslich eine Silicium-basierte Photoanode herzustellen, die für die Sauerstoffentwicklung in sauren Elektrolyten geeignet ist, wurde eine neuartige Herangehensweise entwickelt: die Anwendbarkeit des effizientesten Wasseroxidationskatalysators, RuO_2, zur Polymerisation von Alkoholen wurde hierzu ausgenutzt. Dadurch konnte eine stabile organische Schutzschicht hergestellt werden, welche zum ersten Mal den Langzeitbetrieb eines Silicium-RuO_2 Schichtsystems als OER-Photoanode ermöglichte. Die organische Schutzschicht wurde hierbei durch eine Iod-gestützte elektrochemisch-reduzierende Polymerisation realisiert, die zeitgleich mit der elektrophoretischen Abscheidung von RuO_2 stattfand. Eine Analyse der möglichen Reaktionswege legt nahe, dass die RuO_2-induzierte Katalyse auf E_2-Eliminationsschritten beruht, welche für eine sp^3-sp^2 Umformung der Kohlenstoffbindungen innerhalb des

Filmes sorgen. Für die beiden photoelektrochemischen Anwendungsformen, die photovoltaische und die photoelektrokatalytische, wurden Photostromdichten von 20 $mAcm^{-2}$ bzw. 15 $mAcm^{-2}$ sowie Stabilitäten von 8 bzw. 24 Stunden erzielt. Die organische Schutzschicht ermöglicht schliesslich Silicium-Photo-spannungen von 500 mV, was auf eine ausserordentlich hohe Grenzflächenqualität hindeutet.

Abstract

In the presented work, efficient and stable multi-junction semiconductor electrodes are introduced for the two half-cell reactions of photo-assisted splitting of water, the hydrogen evolution reaction (HER) and the oxygen evolution reaction (OER).

For efficient and stable HER in acidic electrolytes, novel composite photocathodes were developed which functionalize device-grade $Cu(In, Ga)Se_2$ thin-film absorbers in conjunction with electrocatalytic Pt-implemented TiO_2 layers. Varying Pt-concentrations were systematically investigated in order to optimize simultaneously (i) the conductivity of the $Pt - TiO_2$ films, (ii) the electrocatalytic activity, and (iii) light-guidance toward the chalcopyrite absorber. It is shown that the gradual increase of the Pt-concentration passes through an efficiency- and stability-maximum of the device (at about 5 vol.% Pt of the precursor solution). At this maximum, optimized light-incoupling into the chalcopyrite light-absorber was achieved and 15 $mAcm^{-2}$ at the thermodynamic potential for H_2-evolution (0 V vs. RHE) were realized. Devices, fabricated according to this optimized parameter, operated over more than 24 hours with no sign of degradation.

For the corresponding preparation of semiconductor-based photoanodes, electrophoretic deposition was used for formation of two different water oxidation catalysts, ZnO:Co and RuO_2 on semiconductor supports. Firstly, for OER in alkaline solutions, an extensive analysis was carried out in order to determine optimized parameters for electrophoretic deposition of pre-synthesized ZnO:Co catalysts from varied organic solvents on fluorinated tin oxide. Evaluation of the electrochemical activity proved a clear solvent-dependence with highest activity upon deposition from acetonitrile and lowest activity upon deposition from ethanol. Detailed analysis of the respective films by various methods showed that the change in electrochemical activity is caused by a corresponding variation in the size of the active surface area. It is furthermore shown that less active but highly transparent ZnO:Co phases, prepared from ethanol-containing suspensions, can be successfully employed in a stacking configuration with low-cost triple-junction solar cells. Thereby, solar-to-hydrogen efficiencies of up to 5.0% were achieved. Secondly, for devising a silicon-based photoanode, applicable to OER in acidic media, a novel approach was developed: the capacity of the most efficient water oxidation catalyst in acidic electrolytes, RuO_2, was exploited towards alcohol polymerization. Thereby, a stable organic protection layer could be formed which allows for the first time long-term operation of silicon-RuO_2 junction as OER-photoanode. The interfacial layers are generated via iodine-mediated electro- reductive polymerization of alcohols, simultaneously forming during electrophoretic transport of RuO_2. Reaction chemistry analyses suggest that the RuO_2-induced catalysis introduces E2-elimination reactions which result in a carbon sp^3-sp^2 transformation within the film. For the two modes of photoelectrochemical operation, the photovoltaic and the photoelectrocatalytic mode, $20mAcm^{-2}$ and $15mAcm^{-2}$ photocurrent densities, respectively, were obtained with operational stability for 8 and 24 hrs. The interfacial organic-protection layer enables Si photovoltages of 500mV, demonstrating an extraordinary electronic interface quality.

Contents

1 Introduction 1

2 Concept of photoelectrochemical water splitting 7
- 2.1 Principle of photoelectrochemical cells 7
- 2.2 Semiconductor photoelectrode material 11
- 2.3 Description of electrolytes used for splitting of water 12
- 2.4 Semiconductor (SC)/ electrolyte junctions: 13

3 Introduction to photoelectrode architectures based on Si and chalcopyrite supports 17
- 3.1 Introduction to the used material combinations for HER 17
  - 3.1.1 $Cu(In,Ga)Se_2$ chalcopyrite for HER 17
  - 3.1.2 Pt-doped TiO_2 as electrocatalytic protection layer on CIGSe supports 18
- 3.2 Introduction to the used materials combinations for OER 19
  - 3.2.1 n-Silicon as an absorber for OER 19
  - 3.2.2 ZnO:Co as catalyst for OER in alkaline electrolytes 20
  - 3.2.3 RuO_2 as catalyst for OER in acidic electrolytes 20

4 Experimental section 23
- 4.1 Sample preparation 23
  - 4.1.1 Ion-Layer-Gas-Reaction (ILGAR) 23
  - 4.1.2 Electrophoretic deposition (EPD) 24
- 4.2 Analytical methods 27
  - 4.2.1 Electrochemical analysis 27
    - 4.2.1.1 Current-Voltage (CV) behavior 27
    - 4.2.1.2 Incidence photon to charge carrier conversion efficiency (IPCE) 28
    - 4.2.1.3 Mott-Schottky measurements 29
    - 4.2.1.4 Differential electrochemical mass spectroscopy (DEMS) . 30
  - 4.2.2 Spectroscopic analysis 31
    - 4.2.2.1 Grazing incidence X-ray diffraction (XRD) 31
    - 4.2.2.2 Surface photoelectron spectroscopy(PES) 32
  - 4.2.3 Morphological-chemical analysis 34
    - 4.2.3.1 Scanning Electron Microscopy coupled with Energy Dispersive X-ray (SEM/EDX) Analysis 34
    - 4.2.3.2 Transmission Electron Microscopy (TEM) 35
  - 4.2.4 Optical analysis 36
    - 4.2.4.1 Ultraviolet-visible spectroscopy 36
    - 4.2.4.2 Fourier Transform Infrared Spectroscopy (FTIR) 37
    - 4.2.4.3 Surface photovoltage spectroscopy (SPV) 37

5 Results and discussions 39
- 5.1 Characterization of doped $TiO_2/Cu(In,Ga)Se_2$ photocathodes 39
  - 5.1.1 $Cu(In,Ga)Se_2$ as an absorber in heterojunction photocathode . . 40
  - 5.1.2 Effect of the TiO_2 deposition temperature on the device performance 42
  - 5.1.3 The Pt-doped TiO_2 layer: variation of the doping density 44
    - 5.1.3.1 The twofold functionality of Pt as dopant and catalyst . 46

5.1.3.2 Correlation of optical behavior with doping density . . . 50
5.1.3.3 Dependence of the energy of the tail states on the doping density 52
5.1.3.4 IPCE - DEMS measurements 54
5.1.3.5 pH dependent performance: CV and stability measurements 55
5.1.4 Interface engineering by thin interfacial TiO_2 deposited by Atomic Layer Deposition (ALD) 57
5.2 EPD-prepared semiconductor electrodes for electrocatalytic and photo-assisted evolution of oxygen 61
5.2.1 ZnO:Co on FTO as electrocatalyst in alkaline electrolytes 62
5.2.1.1 Effect of the electrophoretic mobility on the quality of the EPD process 62
5.2.1.2 Effect of the organic solvent on the catalytic activity of ZnO:Co electrodes 66
5.2.1.3 Optical analysis of ZnO:Co on FTO by UV-VIS and SPV 69
5.2.1.4 Morphological analysis by SEM/ EDX/ TEM 74
5.2.2 Characterization of RuO_2 on FTO as electrocatalyst in acidic electrolytes 79
5.2.3 RuO_2 /Si photoanode for acidic electrolytes 80
5.2.3.1 RuO_2/Si: formation principles 82
5.2.3.2 Characterization of the RuO_2/Si photoanode 90
5.2.3.3 pH dependent performance of the RuO_2/n-Si photoanodes 94
5.2.3.4 Photoelectrochemical solar cell application 94

6 Summary and outlook 97

7 Appendices 99
7.1 References 99
7.2 List of figures 107
7.3 List of publications 113
7.4 Patents 115
7.5 Conference contributions 115
7.6 Curriculum Vitae 117

1 Introduction

Clean production of hydrogen fuel from sunlight and water is the most desirable approach for establishing a green economy for future generations [1]. Hydrogen (H_2) represents a very attractive, emission-free alternative fuel, whose energy density per mass unit (143 kJ/g) is approximately 100 times higher than for batteries and approximately three times higher than for standard liquid fuels [2]. Therefore, H_2 is assumed to be a very promising candidate for substitution of fossil energy resources. Most of the conventional techniques for H_2 production require a source of carbon. One of the sustainable and environmental friendly methods for H_2 production is solar water splitting. Water is an abundant source of hydrogen, and approximately $\sim 3.5 \times 10^{13}$ L of water is needed to store the energy the world uses in one year (4.7×10^{20} J) in the form of hydrogen. This corresponds to 0.01% of the annual rainfall, or 0.000002% of the amount of water in the world's oceans [3]. The overall reaction for water splitting is written as:

$$2H_2O \longleftrightarrow 2H_2 + O_2 \qquad \Delta G = +237\ \mathrm{kJ/moleH_2} \tag{1.1}$$

This reaction with positive Gibbs energy, G, is an endothermic reaction, which means that external energy has to be provided to the system in order to realize the splitting of water.

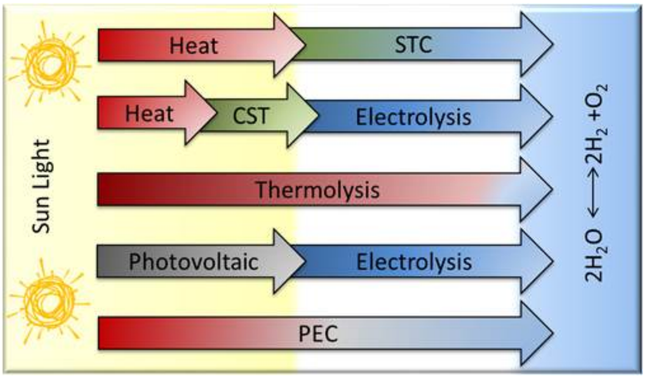

Figure 1.1: solar to hydrogen pathways.

Several different conversion routes can be followed in order to utilize sun light for splitting of water. Figure 1.1 summarizes these pathways. The first three routes are based on solar thermal systems. The solar thermochemical route STC)[4] is based on photon-to-thermal energy conversion followed by a thermal-to-chemical conversion step. The concentrating solar thermal route (CST) [5] is a three steps process involving photon-to-heat, heat-to-electricity and electricity-to-chemical conversion steps. The third route is ultra-high temperature thermolysis [6], a one-step process, being performed at elevated temperatures of 2200°C-3000°C or at 900°C -1200°C with the assistance of Pt/Ru catalysts [7]. The fourth route is a two-step process that combines photovoltaics (PV) with electrolysis. The conversion of light to electricity is realized by PV while the conversion of electrical to chemical energy is carried out in electrolysers. Although all these pathways provide hydrogen as alternative fuel, most of them require multi-step processing and efficiency losses occur at each step. Moreover, ultra-high temperature treatments as in thermolysis represent further energetic disadvantages. Therefore, from an economic point of view, the application of photocatalytic and photoelectrocatalytic (PEC) conversion processes using state-of-the-art semiconductors is an appealing alternative approach to produce hydrogen from water and light [8]. For this purpose, semiconductor-based architectures (as used in high-efficient photovoltaics) are employed in order to efficiently separate photoinduced charge carriers (electrons and holes) and to drive subsequently the water-splitting reaction [9]. This photoelectrochemical (PEC) route is a one-step process and is usually performed at room temperature and under ambient pressure conditions. In 1972 A. Fujishima and K. Honda reported for the first time direct water splitting in a photoelectrochemical cell using a crystalline TiO_2 (rutile) anode and a Pt cathode under ultraviolet (UV) irradiation and at an external bias of 840 mV [10-11]. Since then, considerable efforts have been devoted to accomplish further advancements in this field. In 1981 a PEC device based on single crystal p-InP, covered by a thin Ru layer and with solar-to-hydrogen (STH) efficiency of 12% was reported by A. Heller [12]. A comparable efficiency of 12.1% was reported by Lewerenz et al. [13] in 2010 for p-InP covered by Rh nanoparticles. In 2000, Turner et al. [14-15] and Licht et al. [16] reported 12% and 18% STH based on III-V ($p - GaInP_2/GaAs$) and Si/III-V monolithic devices, respectively. Very recently, May et al. [17] reported a very efficient monolithic device based on multi junction GaInAs/GaInP with Rh and RuO_2 cocatlaysts reaching an efficiency of 14%. However, all these high-efficiency architectures are based on rare and therefore expensive materials which make a scale-up process to large-area electrodes difficult. Since 2010, significant efforts have been done to replace noble-metals with earth-abundant materials and to substitute very expensive III-V semiconductors by other appropriate supports. In 2011, Nocera et al. [18] reported a monolithic device based on triple-junction amorphous silicon (a-Si) and Co catalysts for OER and NiMoZn catalysts for HER, realizing an STH of 2.5%. In 2013, van de Krol et al. reported 4.7% in STH employing photoactive $BiVO_4$ [19] coupled with double-junction a-Si and enhanced by Co catalyst, prepared according to the route developed by Nocera (so-called Co-pi catalysts). Other electrocatalytic metal oxides such as WO_3 [20] and Fe_2O_3 [21] are in the spotlight of ongoing research, too, due to their promising photoactivity.

In this context, one of the promising candidates as photocathode for HER within a PEC water splitting device is copper chalcopyrite. $Cu(In, Ga)Se_2$ has a band gap of 1.2 eV with suitable band position with respect to H_2 evolution, i.e. the conduction band minimum is located above the theoretical potential for proton reduction in acidic electrolytes (about 4.6 eV). The material can be furthermore fabricated by a relatively simple and low-cost preparation process and proves high chemical stability [22-26]. The advantage of chalcopyrite-based materials, besides having the right potential for hydrogen evolution, is their ability to absorb light in the entire visible range, resulting in high photocurrent densities with values of up to $38mA/cm^2$ for world record $Cu(In, Ga)Se_2$-based solar cells with a photovoltaic conversion efficiency beyond 20% [27]. The benefit and challenge of a chalcopyrite-based photocathode is the transfer of the unique photovoltaic performance to an efficient photocathode for competitive and cheap solar hydrogen production. According to very recent investigations, chalcopyrite thin films can be successfully employed as composite photocathode;in combination with organic thin films of polymeric carbon nitride as surface modification, they can be used for reduction of protons by light-induced photoelectrons [28-29]. Up to now, only a few studies have been reported in the literature concerning the capability of inorganic composites based on chalcopyrite thin films as photocathode for PEC water splitting devices [30-32]. In alkaline electrolytes, photocurrent densities of up to $8mAcm^{-2}$ at the thermodynamic potential for H_2-evolution have been reported recently [30]. However, the conversion of incident photons to excess minority charge carriers remained low. Very recently, it has been shown that the stability of $ZnO/CdS/Cu(In_xGa_{1-x})Se_2$ device-grade solar cells in water and under illumination imposes a severe problem due to photodegradation of the chalcopyrite under reducing conditions [32]. Hence, the development of a composite (or heterojunction) device based on p-type $Cu(In, Ga)Se_2$ thin films and an appropriate protection layer withstanding the photocorrosive conditions represents a considerable challenge for this novel type of composite. In the first part of this work, this challenge is addressed by systematic development of a TiO_2 protection layer with incorporated Pt as simultaneous H_2-catalyst and electronic dopant. In complemental efforts, extensive research has been carried out in order to also develop corresponding photoanodes for optimization of the counter-reaction, i.e. the oxygen evolution reaction. Due to the slower kinetics of the OER, this half-cell reaction is recognized as the bottleneck for efficient overall splitting of water [33-38]. The OER reaction requires, in general, higher overpotentials with respect to the thermodynamic potential (+1.23V vs. RHE at pH0) in comparison to the corresponding hydrogen evolution reaction. These overpotentials lead to partial loss of energy and reduce the overall efficiency of the water splitting reaction [39-41]. In order to enhance this reaction, combination of semiconductors with co-catalysts is therefore inevitable. In 2015 Jaramillo et al. [42] performed a comprehensive study on overpotential and stability of different electrocatalysts employed in HER and OER. Using electrocatalysts which are not responsive to illumination (e.g. $ZnO:Co, NiO_2, IrO_2, RuO_2$), the development of efficient photoelectrode architectures is facilitated: these materials permit individual testing of the catalytic activity in the dark, i.e. independent on light-absorption behavior and photon-to-charge-carrier transformation. Subsequently, those electrocatalysts, that combine most effectively electrochemical activity and beneficial optical properties, can be immobilized on photo-active supports in order to test the synergetic properties of the thereby fabricated junctions. This modular approach is usually termed in the literature as photo-assisted conversion process. Already many efforts have been done by Trasatti and Lodi [43] to realize efficient evolution of oxygen in acidic electrolytes employing IrO_2 and RuO_2. Although these catalysts are very efficient for the OER, the use of expensive iridium and ruthenium makes large-scale application cost-ineffective. Recent work on metastable cobalt-oxidic materials by Shao Horn. et al. showed the great potential in employing intrinsically metastable materials (e.g. $LiCoO_2$) for the in-situ formation of amorphous, cobalt-oxidic water oxidation catalysts (WOC) [44-46]. Pfrommer [47] and coworkers have shown that employing Co-substituted ZnO (ZnO:Co) as a precatalyst leads to higher hole-conductivity in the in-situ formed WOC nanocomposite due to the formation of core-shell structures with the polar ZnO:Co precatalyst integrated into the film [48]. It should be noted that pre-synthesized catalyst powders require a suitable immobilization method in order to functionalize the catalysts on appropriate semiconductors. In the case of ZnO:Co, electrophoretic deposition (EPD) from powder suspension in organic solvent has been successfully employed to fabricate electrodes with stable activity at pH7 and pH12. EPD represents in general a cost-effective technology for realization of colloidal coatings in many fields of application [49-50]. Powder materials are suspended in a chemically inert solvent and are transported under the influence of a (direct-current, DC) electric field towards the supporting electrode [49-53]. The key parameter in EPD is the velocity of the particles which determines the deposition rate and is dependent on the physical properties of the solvent. In the case of ZnO:Co, the influence of varied organic solvent on the properties of the resulting electrodes has not yet been sufficiently explored. Likewise, optimized preparation conditions for application of ZnO:Co films also in photo-assisted evolution of oxygen have not been identified. Particularly the latter research subject can help transferring efficient electrocatalysts to the important field of photoelectrolytic splitting of water.

For all semiconductor-based (photo-)electrodes, stability under operational (cathodic or anodic) conditions is of utmost importance. In recent approaches, nano-scaled water oxidation catalysts have been deposited on metallic overlayers or have been employed as compact oxide films in order to avoid oxidation of the substrate upon photoelectrochemical splitting of water [54-57]. Both schemes come with their individual disadvantages: metallic protection layers have to be devised sufficiently thick in order to compensate structural flaws upon unwanted self-oxidation. Increased thickness, however, limits the light reaching the semiconductor substrate. Oxide films of sufficiently pin-hole free quality, on the other hand, may introduce non-negligible serial resistance to the electrode and require mild and complex preparation conditions in order not to compromise the substrate [58]. For both materials, metals and oxides, junction formation with the semiconductor is critical since the achievable photovoltage is easily reduced by partial Fermi-level pinning at the interfacial region [59]. A third material class, organic protection layers, finally, is considered a promising alternative route for electrode protection in the future. Organic layers can offer nearly ideal electronic surface passivation but have been employed so far only in H_2O-containing electrolytes below the water oxidation potential due to their increased susceptibility to self-oxidation [60-61]. In this work, $Cu(In,Ga)Se_2$ and n-Si are chosen as absorber materials for application as photocathodes and photoanodes, respectively. In the first part, the development of transparent conductive oxide (TCO) films, composed of Pt-doped TiO_2, is described as simultaneously electrocatalytic and protective surface film on $Cu(In,Ga)Se_2$ absorbers. High STH efficiencies result from optimized light-guidance into the chalcopyrite support. The superior electrocatalytic performance is established by incorporation of nanoscaled Pt-clusters into the TiO_2 overlayer. The layers were deposited by chemical vapor deposition of undoped and Pt-doped TiO_2 thin films on $Cu(In,Ga)Se_2$ substrates. The synthesis is characterized by a molecular gas phase deposition technique, ILGAR (Ion Layer Gas Reaction)[62-63], at elevated temperatures of up to 400°C. Thereby, phase pure anatase Pt-doped and undoped TiO_2 thin films were obtained. The resulting $TiO_2/Cu(In,Ga)Se_2$ photocathodes showed high stability in acidic to neutral electrolytes.

In the second part of the project immobilization of presynthesized catalysts on FTO and n-Si by EPD is reported for preparation of electro/(photo-)anodes, stable in alkaline and acidic electrolytes. Nano-particulate ZnO:Co catalysts show high stability in alkaline electrolytes while RuO_2 catalysts are well-known OER catalyst in acidic electrolytes. The role of the organic solvent upon electrophoretic deposition of ZnO:Co and RuO_2 is investigated and structural, electrochemical as well as optical properties are correlated to the applied preparation procedure. In the case of ZnO:Co, it will be shown that the organic solvent considerably influences the size of the active surface area of the deposited films. It is thereby possible to identify acetonitrile as organic solvent which provides higher activity than the reported acetone solution [47]. Secondly, and most important, ethanol will be identified as promising solvent for deposition onto photo-active semiconductor supports: although the observed onset potentials of ethanol-prepared samples are lowest, optical transparency is highest. Consequently, it can be shown that light-incoupling into a triple-junction solar cell is improved which helps overcompensating the lower activity of the electrocatalytic layer. The resulting PV-electrocatalyst-device on the laboratory scale realizes 5.0% STH efficiency, demonstrating thereby the potential of low-cost and highly efficient solar-driven splitting of water. Strong light absorption by acetonitrile- and acetone-prepared samples, on the other hand, limits the corresponding efficiency to about 1%. In the case of RuO_2, a novel synthesis scheme for preparation of polymeric protection layers is reported. Suspensions of RuO_2 in alcohol/iodine are shown to allow for complex reactions such as dehydration of the alcohol [64], formation of terminal aldehyde groups and sp^3-sp^2 transformations under electrochemical conditions. A single-step fabrication route creates thereby an organic interface on silicon that integrates near-ideal electronic and electrochemical passivation in an ultrathin polymeric layer of 3-4 nm thickness and allows for extended operation of Si/Polymer/RuO_2 in acidic electrolytes for more than one day.

2 Concept of photoelectrochemical water splitting

2.1 Principle of photoelectrochemical cells

PEC cells utilize light energy i.e. photons to perform electrochemical reactions (here, splitting of water into H_2 and O_2). The PEC cell usually consists of an anode and a cathode, immersed into an electrolyte and connected to each other via an external wire. A power supply is added to the circuitry in order to drive, if necessary, the reaction in question with additional bias potential. In so-called monolithic configurations, both electrodes are integrated into a single device. In half-cell investigations for photoelectrochemical water splitting, typically either the anode or the cathode consists of a photoactive semiconductor while the other electrode is a Pt counter-electrode. Therefore semiconductors are considered to be the main component of a PEC cell. Fundamental process steps in a PEC cell under operational conditions are summarized below:

I) Absorption of incident light by the semiconductor and generation of charge carriers (electron-hole pairs). This process is based on the internal photo-effect requiring photons with energies higher than the band gap of the semiconductor.

II) Separation and transportation of generated charge carriers. Electron -hole pairs are separated due to the presence of an electric field inside of the semiconductor (space charge region, SRG) and transported under an external bias in opposite directions.

III) Extraction of generated charge carriers and production of H_2 at the cathode and O_2 at the anode. Electrons and holes accumulate at the respective solid-liquid junctions of cathode and anode and induce corresponding electrochemical reactions in the surface-near region.

All these processes as separation, transportation and extraction are due to the rectifying nature of the semiconductor/electrolyte junction and, if required, an additional external bias, all of which this described in detail in section 2.4. For an optimized, near-ideal case, suitable semiconductors have to be identified which not only absorb the highest portion of the solar spectrum (visible light) but also have appropriate positions of the respective minima of the conduction and valence band, C_B and V_B, i.e. straddling the thermodynamic potentials of H_2 and O_2 evolution, respectively. If no kinetic limitation induces additional overpotentials, no external driving potential is required in this case. In reality, the systems based on single light absorber components have low efficiency in optical absorption as, for instance, TiO_2. Although TiO_2 offers suitable band position for both H_2 and O_2 evolution the large band gap (~3.2 eV) restricts light absorption to UV, reducing thereby the usable amount of the solar spectrum to 4% only [65]. Figure 2.1 shows the relative positions of the conduction and valance band minima of several semiconductors. According to this scheme, not all of them are suitable for simultaneous HER and OER but only one of the half-reactions.

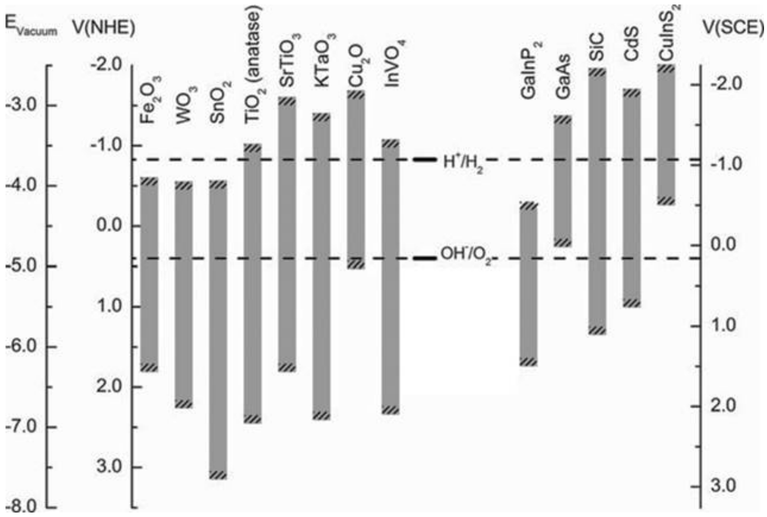

Figure 2.1: Position of conduction and valence band minima, C_B and V_B, of semiconductors with respect to the thermodynamic potentials for H_2 and O_2 evolution, respectively [69].

For those materials which surpass with their minima both redox potentials, the band gap is too large in order to absorb more than UV light. To overcome this low efficiency, the use of tandem PEC absorber was proposed. Such architecture contains two semiconductors, one suitable for H_2 evolution and one suitable for O_2 evolution. Recently, for two-junction PEC photoelectrodes, prototypes based on III-V semiconductors such as InGaP/GaAs [15], AlGaAs/Si [66] and InGaP/InGaAs [67] were reported, reaching STH efficiencies between 10 and 20% [68].

The overall water splitting reaction is divided in two half-cell reactions and depends on the pH value of the electrolyte (alkaline or acidic)[3]. For an alkaline electrolyte (pH14), the reduction and oxidation reactions with respect to the Normal Hydrogen Electrode, NHE, are:

$$4H_2O + 4e^- \longleftrightarrow 2H_2 + 4OH^- \qquad E^o_{red} = -0.828\,V\,vs.\,NHE \tag{2.1}$$

$$4OH^- + 4h^+ \longleftrightarrow 2H_2O + O_2 \qquad E^o_{ox} = -0.401\,V\,vs.\,NHE \tag{2.2}$$

For an acidic environment, the oxidation and reduction reactions are:

$$4H^+ + 4e^- \longleftrightarrow 2H_2 \qquad E^o_{red} = +0.000\,V\,vs.\,NHE \tag{2.3}$$

$$2H_2O + 4h^+ \longleftrightarrow 4H^+ + O_2 \qquad E^o_{ox} = -1.229\,V\,vs.\,NHE \tag{2.4}$$

This difference in anodic and cathodic reactions for acidic and alkaline electrolytes is due to the different concentrations of H^+ and OH^- ions in the respective media. For neutral electrolytes both pathways can be expected to occur simultaneously [70]. Depending on the conduction type of the semiconductor the motion of photogenerated electrons and holes is different. For n-type semiconductors, the photogenerated electrons are directed toward the back contact (proton reduction) and photogenerated holes are directed toward the semiconductor/electrolyte interface (oxygen evolution). The opposite scheme applies for p-type semiconductors. A PEC device may be composed of one semiconductor as photoelectrode and a metal as counter-electrode or may be composed of two semiconductors as photoanode and photocathode, respectively. Figure 2.2 shows the corresponding energy diagrams of different potential PEC configurations. The configuration can consist of one photoelectrode for oxygen (a) or hydrogen (b) evolution and a metal as counter electrode for the counter half-cell reaction. For this scheme, an optimal size of the photoanode's band gap was estimated to be ca. 2.0 eV. The maximum energy conversion efficiency for a single absorber is approximately 23% as calculated by Shockley and Queisser [71]. A further possible configuration consists of two photoelectrodes (c); one photoelectrode is acting as photocathode for evolution of hydrogen and the other as photoanode for evolution of oxygen [18,72-76]. In this case, the band gap of the respective semiconductors can be smaller than the required overall minimum potential of 1.23 V. Both semiconductors combine their light-absorption capabilities in a so-called Z-scheme to exceed with their respective contributions the value of 1.23 V. In all these three configurations, a complex and concerted activity of two electrodes, cathode and anode, under illumination is required [77-78]. An alternative configuration of a water splitting PEC cell is the back-to-back wireless design (d) in order to minimize the costs associated with fabricating monolithic devices [79-80].

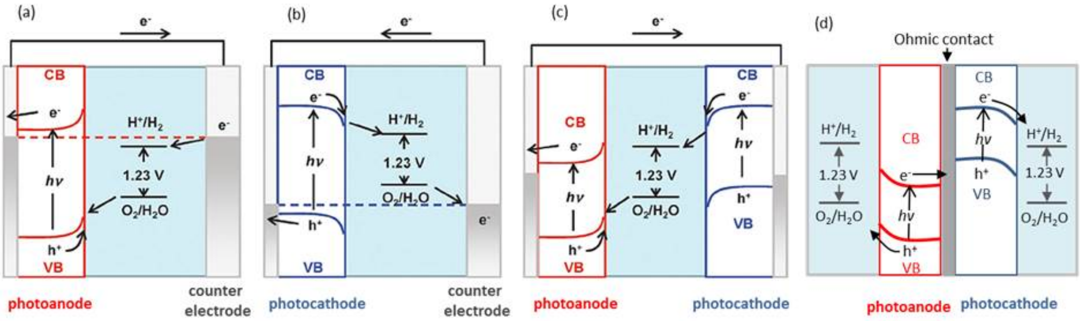

Figure 2.2: Different configurations of PEC cell.

Heterojunction devices prove increasing efficiency in solar-to-H_2 conversion but necessitate consideration of a number of serious boundary conditions [80-83]. The use of relatively small band gap materials (i.e., 1.1-1.7 eV) is desired in order to efficiently absorb light in the range of the terrestrial solar spectrum. Simultaneously, the respective positions of conduction band minimum and valence band maximum have to be adapted to the standard potentials of H_2 and O_2 evolution to provide the necessary overall photovoltage (>1.23 V). Beside a suitable band gap, they should particularly prove stability in aqueous electrolytes, small ohmic losses for charge carrier transport, and the water oxidation/reduction kinetics should proceed faster than surface-mediated charge-carrier recombination. Photocorrosion or photopassivation under cathodic conditions represents a potential risk for some semiconductors [84], but almost all semiconductors are susceptible to rapid oxidation under anodic conditions [85,64]. Therefore, surface protection of the supporting semiconductor has to be realized such that long-term operation in aqueous electrolytes is guaranteed. In order to facilitate the oxidation and reaction kinetics, and minimize the recombination of photogenerated charge carriers, suitable co-catalysts are deposited on the semiconductor surface to provide a high density of active sites for HER and OER [86]. Furthermore, the electrode design has to ensure that photons are efficiently converted to charge carriers and that charge transport is not limited by junction barriers or ohmic losses. In order to assess the efficiency of a (stable) PEC system quantitatively, the solar to hydrogen (STH) conversion efficiency is used:

$$\mathsf{STH} = \left(\frac{(|J_{sc}(mAcm^{-2}| \times 1.23(V) \times \eta_F)}{P(mWcm^{-2})}\right)_{AM1.5} \tag{2.5}$$

Here, J_{sc} denotes the short-circuit photocurrent density, measured at the thermodynamic potential for H_2 evolution, η_f the Faradaic efficiency, i.e. the percentage of charge flow consumed exclusively for HER, and P the incident illumination power density. All these parameters have to be measured under standard solar illumination conditions (AM1.5G) [87]. If the photocurrent in Eq. 2.5 is not determined at the thermodynamic potential, the “Applied Bias Photon-to Current Efficiency (ABPE)“ is used instead:

$$ABPE = \left(\frac{(|J_{photo}(mAcm^{-2}| \times (1.23(V) - V))}{P_{total}(mWcm^{-2})}\right)_{AM1.5} \tag{2.6}$$

Here, V is the additional voltage that is applied to the cell and J_{photo} denotes the photocurrent measured at this voltage.

High efficiency photoelectrochemical water splitting devices require the integration of electrocatalysts (ECs) with light absorbing semiconductors (SCs) [64, 86-98]. Electrocatalysts at the surface of the SCs are minimizing the kinetic losses associated with oxygen- or hydrogen evolution [88]. Although the amount of the catalyst determines the active sites for reaction, this amount should be well chosen in order to prevent unwanted blockage of the incoming light in its passage toward the absorber surface. Figure 2.3 shows the activity and stability of several electrocatalysts for hydrogen evolution (red) and oxygen evolution (green) for alkaline and acidic electrolytes [42].

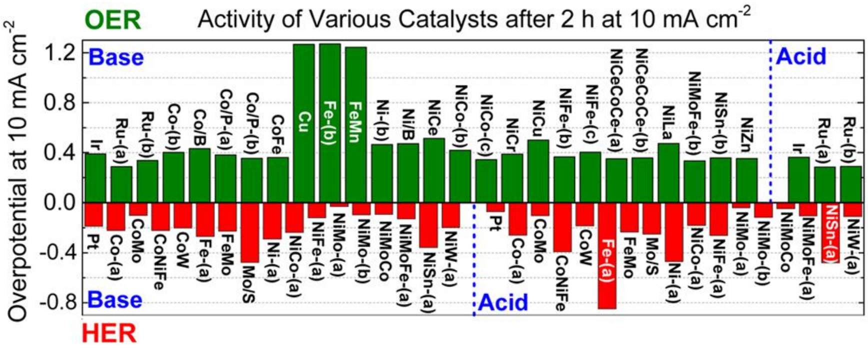

Figure 2.3: Activity of Various catalysts for HER and OER in acidic and alkaline electrolytes.

As shown in the image, the lowest overpotential for HER catalysts in acidic electrolyte (1M H_2SO_4) are Pt [99], NiMo [100] and NiMoCo [101]. For alkaline electrolytes, NiMo proves the highest activity [102]. For OER, most of the non-noble metals show instability under oxidative conditions in acidic electrolytes. Only Ir [103] and Ru [103-104] catalyst are stable in acids. Under alkaline conditions, most catalysts operate with comparable activity for OER. It has been postulated that oxide-based OER catalysts operate via a common mechanism that includes the formation of a OH^* surface hydroxide intermediate which is oxidized to a surface hydroperoxy OOH^* intermediate [105-108]. Although many of these catalysts are comparable in activity, NiMoFe-(b) was observed to be the most stable catalyst for OER in alkaline electrolytes [109].

The key point in the performance of these hetero-structure devices is the type of the junction formed between SCs and ECs and also between SCs and the electrolyte. These junctions are described in detail in section 2.4. First, different types of the semiconductor-electrolyte junctions are explained and subsequently the effect of SCs-ECs junctions with respect to the performance of the resulting photoelectrodes is described. In absence of an electrocatalyst, the semiconductor forms a liquid junction with the aqueous electrolyte.

The difference between the isolated SC Fermi level $E_{f,n}$ and the solution redox potential, E_{O_2/OH^-} , determines the band bending under equilibrium conditions and thus the upper limit of the attainable photovoltage.

When an EC is added on the SC surface, the EC layer modifies not only the rate of electron transfer to and from the solution but also the equilibrium and non-equilibrium interface energetics. Some ECs, such as Pt or dense crystalline RuO_2 and IrO_2, are metallic or metallic-like, respectively, and thus the SC/EC interface is expected to behave according to the well-developed theory of SC/metal Schottky contacts [88].

2.2 Semiconductor photoelectrode material

Solid materials depend on their electron distribution and are classified as metals, semiconductors or insulators. This classification is shown schematically in Figure 2.4. The valence band represents the highest energy range of occupied electron states and the conduction band represents correspondingly the lowest range of vacant electronic states. The difference in energy between the minima of C_B and V_B is called band gap (E_g) and determines the properties of the material. The band gap can be determined by measurement of the absorption coefficient vs. wavelength [110] according to:

$$\alpha = \frac{(h\nu - E_g)^m}{h\nu} \tag{2.7}$$

Here, m depends on the nature of the optical transition: m = 1/2 is applied for a direct band gap, and m = 2 for an indirect gap. Furthermore, h denotes the planck constant and ν is the frequency of light. By extrapolation of a plot of $(\alpha h\nu)^{m^{-1}}$ vs. $h\nu$ to zero absorption, the band gap is determined [3].

As shown in Figure 2.4, there exists an overlap of C_B and V_B in the case of metals. If both bands are separated by a sufficiently large value (>4eV), on the other hand, the material behaves like an insulator. When the difference is smaller, the material is called a semiconductor and the electrons can be excited by visible light into the conduction band. The vacant position of an excited electron in the valance band is called “hole“ and can move through space by transfer of an electron to the vacancy. Beside position of the conduction and valence band of a semiconductor, the “Fermi level“ is a further key parameter. It is defined as the energy level at which the probability of occupation by an electron is 1/2 and shows strict dependence on the doping concentration of the material [110].

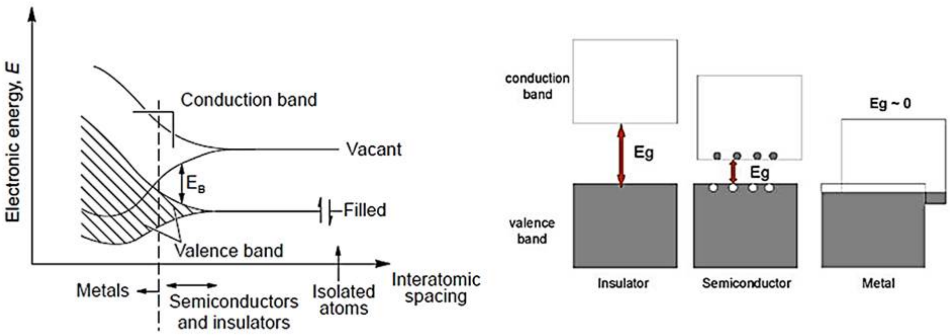

Figure 2.4: Comparison of V_B and C_B positions of a metal, a semiconductor and an insulator[3].

Depending on the nature of the impurities in a semiconductor which give rise to additional electronic states, the semiconductors are classified in two groups: (I) in intrinsic semiconductors, crystal defects generate additional states within the band gap close to C_B and V_B, respectively. At a rate, increasing with temperature, these states can be filled either with electrons to generate excess holes in the valence band or by holes to generate excess conduction electrons. Consequently, the Fermi level position is lowered or raised, respectively, to indicate the nature of the conductivity (p-type or n-type, respectively). In absence of these states, the Fermi level assumes a mid-gap position $E_F = 1/2(E_V + E_C)$ [111]. (II) For extrinsic semiconductors, atoms of another material have to be added to induce corresponding states within the band gap. The resulting conductivity of the material is given by[3]: $\sigma = ne\mu_e + pe\mu_h$, where n and p denote the respective carrier concentration (cm^{-3}), while e is the charge of an electron $= 1.602 \times 10^{-19}$ C and $\mu_e(\mu_h)$ the electron (hole) mobility ($cm^2/(Vs)$). Semiconductor doping can be realized by different methods like epitaxy, diffusion or ion implantation. Depending on whether the added impurities are electron donors or acceptors, the semiconductor's Fermi level is shifted toward the conduction band or valance band, respectively. Figure 2.5 schematically shows the energy levels of n- and p-type semiconductors.

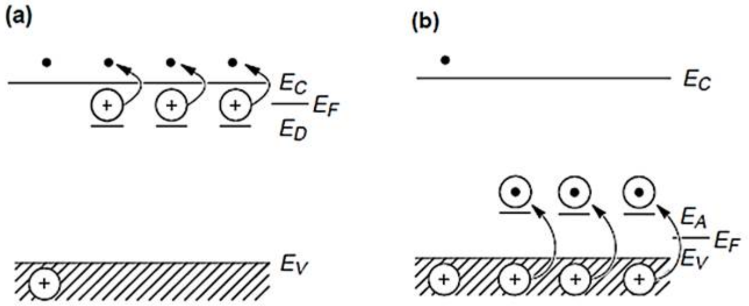

Figure 2.5: Schematic diagram of the energy levels of an n-type semiconductor (a) and a p-type semiconductor (b).

The concentration of electrons in the C_B and holes in the V_B, under equilibrium is given by:

$$n = N_c e^{-(E_C - E_F)/kT} \; with \; N_c = 2(\frac{2\pi m_e^* KT}{h^2})^{3/2} \tag{2.8}$$

$$p = N_v e^{-(E_F - E_v)/kT} \; with \; N_v = 2(\frac{2\pi m_h^* KT}{h^2})^{3/2} \tag{2.9}$$

If the defect state lies within $\sim 2k_B T$ near C_B or V_B, almost all states are ionized at room temperature. Those dopants are called shallow dopants. If the electronic defect state is located at a larger distance, then the dopants are called deep-level donors or acceptors and may act as recombination centers for light-induced electron-hole pairs [111].

2.3 Description of electrolytes used for splitting of water

An electrolyte provides cations and anions in order to conduct electricity by the motion of ions. The electrolyte may be subject to reversible processes as an iodide/triiode containing electrolytes where charges are consumed to oxidize I^- (anion) to I_3^- (cation) and vice versa, or to irreversible processes as in water electrolysis. Due to the low conductivity of neutral water (pH7), the equilibrium of H^+ and OH^- concentration is shifted to more acidic or alkaline conditions. This change is realized by additions of salts and thereby ion dissociation. The addition of these salts, however, introduces further chemical species to the electrolyte which then are in competition with the desired reactions of hydrogen and oxygen evolution: an anion from the electrolyte is in competition with hydroxide ions (OH^-) to give up an electron. If the electrolyte anion has a lower standard potential than hydroxide, it will be oxidized rather than the hydroxide and no oxygen gas will be produced. The corresponding competitive conditions hold true for cations with a higher standard potential than a hydrogen ion. Consequently, cations with lower electrode potentials than H^+ like Li^+, K^+, Ba^{+2}, Na^+ have to be used and anions with higher electrode potentials than OH^- like SO_4^-. Common electrolytes are therefore sulfuric acid, potassium hydroxide, sodium sulfate, and potassium phosphate. The redox potential of water electrolysis shows pH dependence and can be calculated by:[112]

$$E = E_0 - pH \times 0.059 - E_{ref} \tag{2.10}$$

Here, E_0 is equal to 1.23V at 25°C and E_{ref} is the potential of the used reference electrode.

2.4 Semiconductor (SC)/ electrolyte junctions:

Depending on the position of the Fermi energy of the semiconductor and the chemical potential of the solution (redox potential), the direction of the band bending in the semiconductor varies. Figure 2.6 shows the different energy levels for p-type (a) and n-type (b) semiconductors and the redox potential position of the electrolyte (c) on the common vacuum scale. In this picture, χ and ϕ are the semiconductor electron affinity and work function, respectively. When a semiconductor is immersed in the redox electrolyte, depending on the position of the Fermi level of the semiconductor and the redox potential of the electrolyte, the resulting band banding in the semiconductor interface varies.

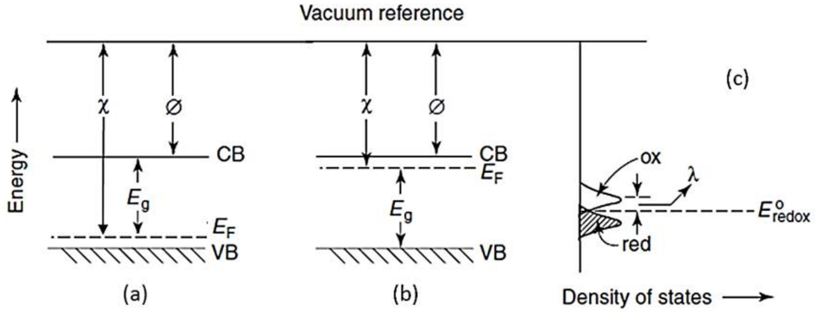

Figure 2.6: energy levels in (a) p-type semiconductor, (b) n-type semiconductor and (c) redox electrolyte [113].

Figure 2.7 shows the three scenarios for semiconductor-electrolyte junctions in the dark under equilibrium for n-type (a, c) and p-type (d, f) SCs. The first scenario holds when in the n-type or p-type semiconductor, the Fermi level and E_{redox} of the electrolyte is at the same energy (a/d); therefore, after contact formation, no net charge transfer occurs and this situation is named as flat band potential (E_{FB}). The determination of the flat band potential and charge carrier concentration (N_D), can be performed via Mott-Schottky measurements as explained in section 4.2.1.3. The second scenario holds when the Fermi level for an n-type semiconductor is higher than E_{redox} of the electrolyte (b). After contact formation the electrons flow from the semiconductor to the electrolyte. During this process, positive charges are left behind in the semiconductor. As a consequence, a space charge region (depletion layer) is formed within the semiconductor which results in an upward band bending. This argument applies to p-type semiconductor when the Fermi level is lower than the redox potential. In this case, holes flow from the semiconductor to the electrolyte. Therefore the semiconductor is depleted of majority charge carriers and a downward band bending in the semiconductor occurs.

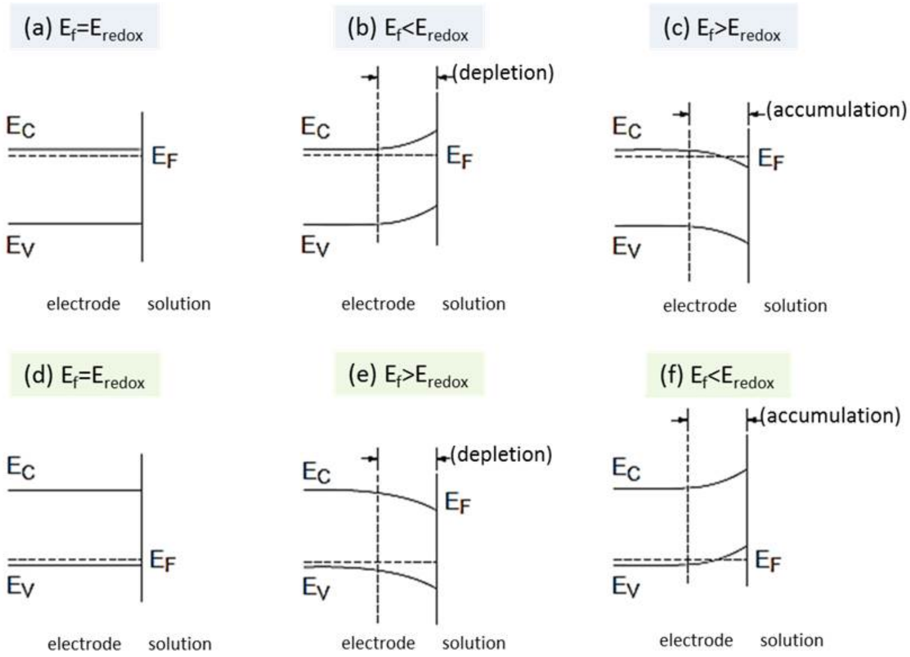

Figure 2.7: Effect of the energy levels of semiconductor and electrolyte on the band edges in the interior of an n-type (a,c) and a p-type (d,f) semiconductor upon contact formation [114].

The third scenario has to be considered when the Fermi level in the n-type semiconductor is lower than the redox potential of the electrolyte or for p-type SCs if the Fermi level is higher than the redox potential of the electrolyte. In this case, electrons and holes from the electrolyte flow to the n-type and p-type SCs, respectively. Therefore, an excess of majority charge carriers accumulates in the space charge region. As a consequence, a downward and upward band bending in the n-type and p-type SCs are observed, respectively. The charge transfer behavior of the semiconductor (as mentioned above) depends on the type of its junction. If there is accumulation of majority charge carriers at the surface, the semiconductor behaves like a metal. But if the semiconductor is in depletion, then only few charge carriers are available. Then, the reaction rate is very slow, unless the electrode is exposed to radiation with photon energies higher than E_g. Under illumination photo-induced charge carriers are generated and electrons are excited to the conduction band. For n-type SCs, exhibiting an upward band bending, electrons move toward the back contact and holes move toward the solid-liquid interface. There, electrons from the redox couple can be extracted and the semiconductor acts as photoanode.

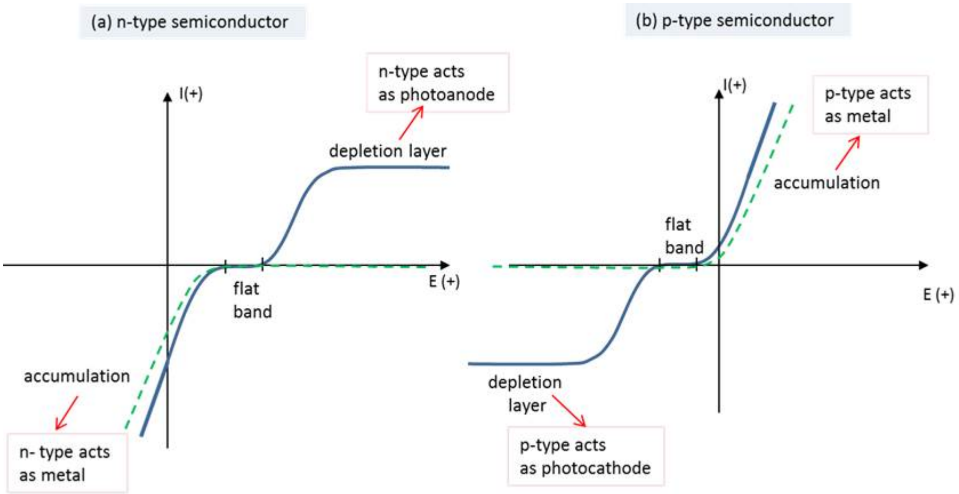

Figure 2.8: Ideal current-voltage behavior of an n-type semiconductor (a) and p-type semiconductor (b) under illumination (solid blue curve) and in the dark (dashed green curve).

For p-type semiconductors with downward band bending, electrons move toward the solid-liquid interface and react with reduction species in the solution whereas holes move toward the back contact. In this situation, the p-type SC acts as photocathode. Figure 2.8 shows the ideal behavior of n-type (a) and p-type (b) semiconductors under illumination (solid blue curve) and in the dark (dashed green curve). In these graphs, all the three situations for the space charge region are depicted. In depletion, no current is flowing in the dark due to the band bending and the low amount of available charges. Under illumination and after the flat band region is passed the current increases and reaches finally saturation values which reflect the limit given by the illumination intensity. In accumulation and in the dark, the behavior of the semiconductors is similar to metals.
In reality, the onset of currents is limited by low reaction kinetics and not as fast as shown in Figure 2.8. Therefore, the increase in current density is considerably slower. To improve sluggish charge transfer kinetics, co-catalysts are coupled to the semiconductor. Figure 2.9 shows the performance of n-type (a) and p-type (b) semiconductors with co-catalysts (red dashed curve) and without (solid blue curve). As shown in this figure, the use of co-catalysts shifts the onset potential to the left for anodic conditions and to the right for cathodic conditions. In other words, the respective overpotential is decreased. Depending on the transparency of the catalysts and the amount of coverage of the surface, the saturation current density varies. When catalysts absorb some portion of the incident light, the saturation current density is reduced.

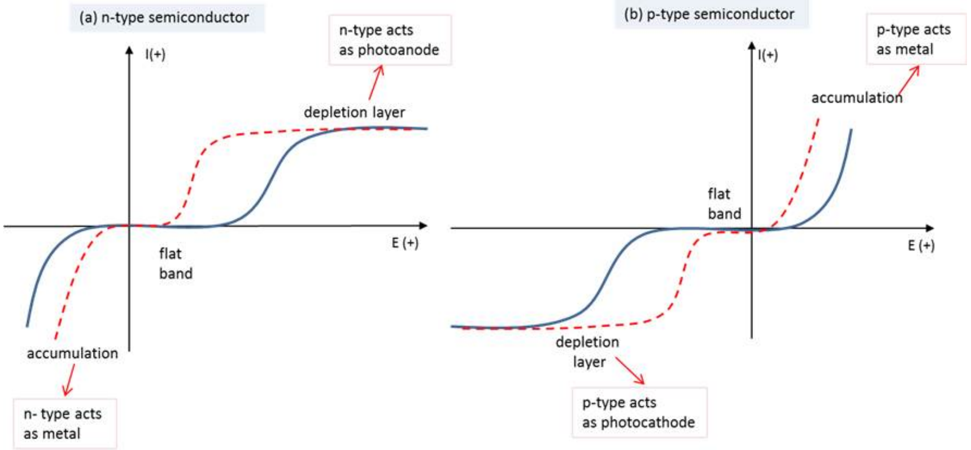

Figure 2.9: behavior of (a) n-type semiconductor, (b) p-type semiconductor under illumination (solid blue curve) and with co-catalysts (dashed red curve).

Based on previous studies, the aim of this work is to develop and to optimize novel photoelectrodes for HER and OER using earth abundant semiconductors. In chapter 3, materials used in this project are introduced. In chapter 4, experimental techniques are described in detail. Chapter 5 presents results and detailed discussions. This chapter is divided in two main sub-sections. Section 5.1 shows the performance of $\mathsf{Pt:TiO_2/Cu(In,Ga)Se_2}$ photocathodes. The results are shown to prove the twofold functionality of Pt as catalyst and dopant in the $\mathsf{TiO_2}$ layer. Section 5.2, focuses on the immobilization of pre-synthesized catalysts on conductive substrates and demonstrates that EPD is a promising deposition method for nanoparticulate catalysts at room temperature. Two pre-synthesized catalysts, ZnO:Co for alkaline electrolytes and $\mathsf{RuO_2}$ for acidic electrolytes were investigated for preparation.

3 Introduction to photoelectrode architectures based on Si and chalcopyrite supports

3.1 Introduction to the used material combinations for HER

3.1.1 $Cu(In, Ga)Se_2$ chalcopyrite for HER

Solar cells based on CIGSe thin films have yielded the highest conversion efficiency among all thin film technologies [115]. Their recent record efficiencies, realized by alkali metal post-deposition treatment (PDT), reached 21.7% [116]. They are designed in a substrate configuration and the deposition temperature is observed to have great impact on their efficiency. In contrast to silicon, CIGSe is a direct semiconductor material which means that the thickness needed for sufficient light absorption is in the range of micrometers and does not require additional light trapping concepts like silicon.

The CIGSe material used in this work was prepared by Ch. Kaufmann et al. [117], Mo layers were sputtered on glass substrates to form a non-blocking contact with the deposited CIGSe film. The CIGSe deposition process is characterized by a three-stage Physical Vapor Deposition (PVD) process [118-121]. In the first stage, two different precursors of In-Se and Ga-Se are evaporated and deposited at 330°C, thereby forming a homogeneous layer in the form of In-Ga-Se. The second and third stages are performed using a sequence of different temperatures ranging from 330°C to 525°C. In the second stage, Cu-Se precursors are deposited until the ratios of [Cu]/ ([In]+[G])-Se) reach 1.15. During the third stage the precursor of (In,Ga)-Se is deposited until the layer becomes Cu-poor and the ratio of [Cu]/([In]+[G])-Se) reaches around 0.84-0.88. The CIGSe layer is p-type and has a band gap of 1.12 eV and a thickness of 3 nm. The CIGSe solar cell is completed when a CdS buffer layer (E_g = 2.4 eV) and a ZnO window layer are deposited by chemical bath deposition and Radio Frequency sputtering (RF-sputtering), respectively. ZnO has a band gap of 3.3 eV. It is therefore transparent for visible light and due to its high doping level it provides high electron conductivity.

âŮŃFigure 3.1(a) shows the current-voltage behavior of a CIGSe solar cell in the dark and under illumination. Its saturation current density and open circuit voltage reaches 37 $mAcm^{-2}$ and +0.6V under illumination, respectively. Figure 3.1(b) shows the external quantum efficiency of the CIGSe solar cell of up to 90%. Figure 3.1(c) shows a SEM cross-section and Figure 3.1(d) shows the band alignment of the CIGSe solar cell under zero-bias voltage. During the growth of CIGSe on Mo, a thin interface layer of $MoSe_2$ is formed. This layer acts as a quasi-ohmic contact [115]. By deposition of n-type layers of CdS and ZnO, band bending occurs in the junction according to n/p-heterojunctions. Furthermore, two regions are formed inside of the CIGSe absorber: one is the space charge region with depletion of majority charge carriers and the second one is a quasi-neutral region (QNR). Despite the suitable band alignment of CIGSe solar cells with the ZnO window layer with respect to potential usage as photocathode for hydrogen evolution, both of the window layer (ZnO) and the buffer layer (CdS) suffer from serious photocorrosion in long-term photocatalytic reactions [122]. Therefore, a new stable TCO is to be developed for replacement of the ZnO:CdS layer. As one of the most promising stable oxides, TiO_2 was chosen and its functionalization on the CIGSe absorber for evolution of hydrogen is described in the next section [123].

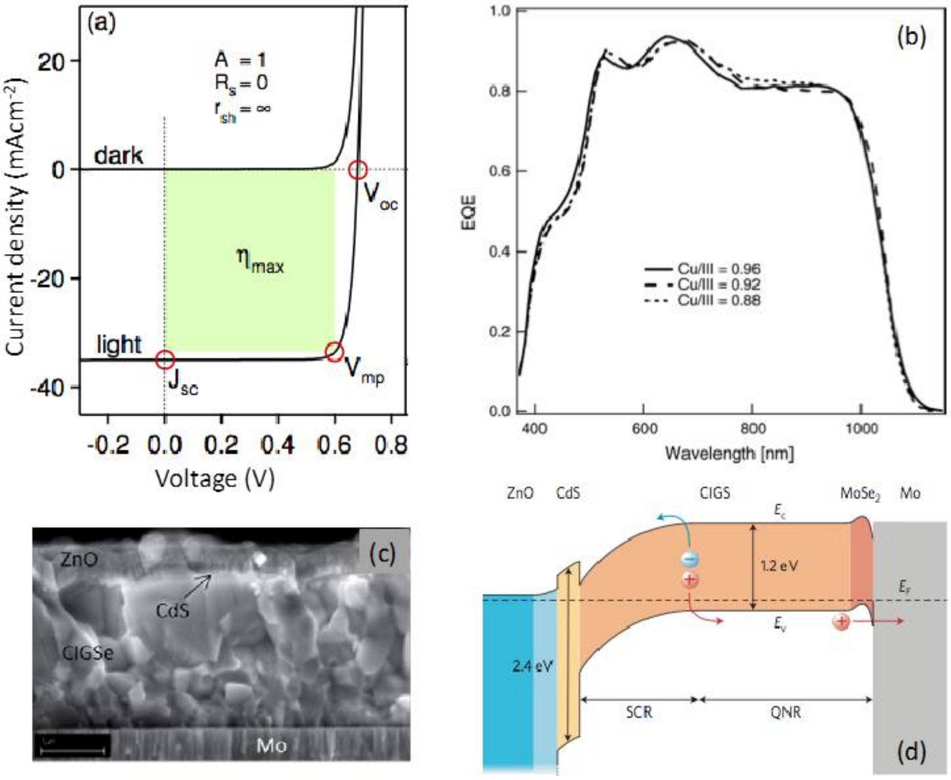

Figure 3.1: (a) Light and dark C-V curves for an ideal solar cell. (b) External quantum efficiency of CIGSe-based solar cell devices with layers with different Cu/(In+Ga) ratios. (c) SEM cross section of a CIGSe solar cell. (d) Schematic band diagram of a CIGS solar cell under zero-bias voltage [115].

3.1.2 Pt-doped TiO_2 as electrocatalytic protection layer on CIGSe supports

TiO_2 is a versatile material that is widely used for coatings in industrial applications such as plastic, paper, inks, fibers, food and pharmaceutical production and processing. Furthermore, TiO_2 is abundantly available, one of the most stable oxides in aqueous electrolytes, non-corrosive, environmentally friendly and cost-effective. In 1972 the photolysis of water on TiO_2 was discovered by Honda-Fujishima [124]. TiO_2 has a large band gap of 3.05 eV for the rutile and 3.2 eV for the anatase crystal structure. Its energy levels make it suitable for water splitting i.e. the conduction band minimum of TiO_2 is more negative than the reduction energy level of water ($E_{H^+/H_2} = 0$ V), while the valance band maximum is more positive than the oxidation energy level of water ($E_{O_2/H_2O} = +1.23$ V) [125]. Therefore it has been considered for decades as candidate for photocatalytic water splitting. A schematic of the TiO_2 band alignment for both rutile and anatase is shown in Figure 3.2.

Despite the many advantageous of TiO_2, there are several issues to be addressed in order to maximize the potential of TiO_2. First of all, its large bang gap enables it to harvesting just 4% of the solar spectrum in the range of UV light whereas the visible light is around 50% of the solar spectrum. A second issue is the fast recombination of C_B electrons and V_B holes to release energy in the form of unproductive heat or photons [126]. A third issue is the high probability of facilitating the backward reaction (recombination of hydrogen and oxygen into water) after decomposition of water into its elements. Due to poor absorption of TiO_2 and the rapid recombination of photogenerated C_B electrons and V_B holes, its maximum theoretical STH efficiency is limited to 2.2% [127].

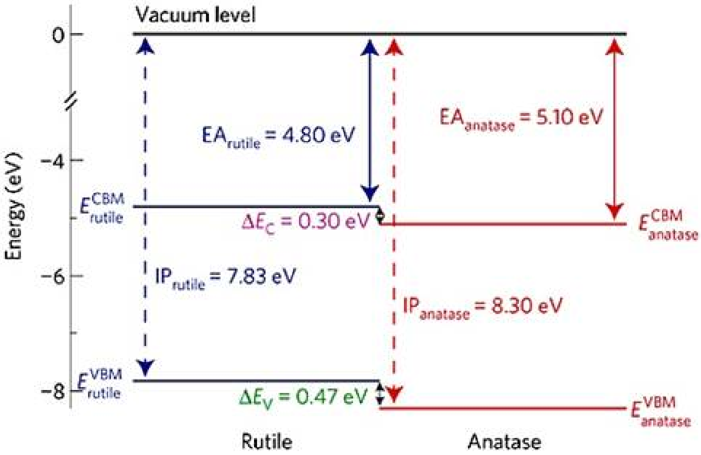

Figure 3.2: TiO_2 band alignment [126].

In order to solve the problems mentioned above, several approaches have been proposed:[128] elemental doping (using transition metals: Cu, Co, Ni, Cr, Mn, Au, Ag, Pt)[129-131], hydrogen treatment of TiO_2 [132-133], non-metal doping of TiO_2 (N, S, C, B) [134-137], composites of TiO_2 with semiconductors having lower band energies (CdS, $Cu(In,Ga)Se_2$), sensitization of TiO_2 with dyes [138-139], TiO_2 doping with an up-conversion luminescence agent [140-141] and adding electron donors or sacrificial reagents to react with photo-generated V_B holes and thereby to enhance electron-hole separation. In this work, two different methods were combined to achieve high efficient photocathodes for hydrogen evolution. TiO_2 prepared by the ILGAR process (section 4.1.1) was doped with platinum as co-catalyst for hydrogen evolution, in order to minimize the recombination rate, and deposited on $Cu(In,Ga)Se_2$. The role of the co-catalyst is to lower the electrochemical overpotential associated with the multi-electron water reduction reaction and to provide an interface with enhanced electron-hole separation. Therefore, the TiO_2 layer acts as catalytically active TCO layer for the CIGSe absorber. The electrochemical analysis is shown in section 5.1.

3.2 Introduction to the used materials combinations for OER

3.2.1 n-Silicon as an absorber for OER

Silicon-based electrodes are earth abundant and low in production costs. They absorb a wide range of the solar spectrum and can directly convert solar energy into chemical energy. Therefore, they have attracted great attention for preparation of artificial photosynthetic systems. Silicon atoms are arranged at the corners of a tetrahedron with a center silicon atom [110]; its lattice constant is 5.43 Å. Its electronic configuration is characterized by filled K and L shells with extra four valance electrons in the $3s^2, 3p^2$ state. Silicon has an indirect band gap of 1.12 eV. The bulk properties of silicon depend on the crystal growth technique and also on further addition of electronically active impurities [142]. However, using silicon as photoanode is demanding. First because of the position of its valance band maximum (5.17 eV) which is smaller than the oxygen evolution potential at pH0 (5.83 eV). Therefore transferring holes from the valance band to water molecules requires an external bias potential. Due to this problem, silicon has been used generally as secondary layer in tandem cell configurations in connection with other semiconductors with suitable band alignment. The second problem of silicon-based photoanodes is its poor electrochemical stability under anodic conditions. As soon as the electrolyte reaches the silicon surface, a passivating SiO_2 film is formed. The formation of pinhole-free free passivation or protection layers is therefore inevitable. The third problem is the lack of its catalytic functionality. Since water oxidation requires a high activation potential, it is necessary to increase the activity of silicon by deposition of catalytic layers.

So far many candidates like metals such as Ni, Pt, Ru and Ir [143-144] and metal oxides such as NiO, RuO_2, MnO, TiO_2, FeNiO and NiCrO [145-146] were explored as protection layers for silicon. These metal and metal oxides mostly have higher work functions than silicon that can form Schottky junctions upon contact with silicon and introduce a built-in electric field at the interface which promotes separation and transport of photogenerated carriers [145]. Apart from these metal and metal oxides, other materials also can be used as protection layer for n-silicon photoelectrodes such as metal silicide [147-148], Co-Pi [149-150] and conductive polymers [151-152]. In this work, n-type silicon is used as the primary light absorption material and photo-carrier generation layer. ZnO:Co and RuO_2 pre-synthesized catalysts were used as catalytic material at pH14 and pH0.3, respectively. It will be shown that side-reactions, occurring concomitantly during EPD, result in simultaneous formation of an interfacial carbon-rich films sufficiently stable to prevent photocorrosion of the silicon substrates.

3.2.2 ZnO:Co as catalyst for OER in alkaline electrolytes

Compunds of earth abundant Co (e.g. Co_3O_4) have received considerable attention in both electrochemical and photochemical applications for catalytic water oxidation. An amorphous cobalt phosphate based material (Co-Pi) was discovered by Nocera et al. which catalyzes water oxidation at pH7 with low overpotentials. The Co-Pi catalysts is formed during electro-deposition from solutions containing Co^{+2} and 0.1 M potassium phosphate buffered at pH7 [34]. Its catalytic performance was associated with oxygen vacancies at the surface and the presence of Co oxo/hydroxyl species, whose oxidation numbers vary between 2, 3 and 4. Therefore, minimizing the size of the particles enhances the surface activity of the catalyst. Recently, Nocera et al. showed that $LiCoO_2$ and $LiCoPO_4$ upon certain anodization conditions transformed into amorphous catalytically active cobalt oxide materials similar to electrodeposition of amorphous cobalt-oxide (Co-Pi) [33,46].

In this context Pfrommer et al. showed that Co-substituted ZnO structures (ZnO:Co) is an interesting electrocatalyst for oxygen evolution. The substitution leads to higher p-type conductivity and higher hole density. ZnO:Co nanoparticles were synthesized by solvolysis of a heterobimetallic single-source precursor (SSP) mixture composed of tetranuclear cubanodic clusters of the di-2-pyridylmethandiolate-ligand [153-154]. The solvolytic reaction commenced in benzylamine at low temperature (180°C) for 10 minutes [17]. The green powder of ZnO:Co has an average crystal size of 17.2 nm, 42.2% cobalt content and 47.3 m^2g^{-1} surface area and a band gap of 2.4 eV.

3.2.3 RuO_2 as catalyst for OER in acidic electrolytes

Ruthenium (IV) oxide has a rutile crystal structure. It is highly stable at low pH values and has great capacity to store charges when used in aqueous solutions. It shows a very low overpotential for oxygen evolution in acidic electrolytes. It can have two different crystal surface orientations (110) and (100). According to the literature, the OER activity of RuO_2 (100) is higher than the activity of (110) surfaces. This observation is accounted for by the higher density of active metal sites on the (100) surface in comparison to the

(110) orientation.
The key parameter that indicates the behavior of RuO_2 is its chemical surface state. Highly hydrated ruthenium dioxide ($H_2O > 24\%$) is not a good oxygen evolution catalyst and under anodic conditions degradation and transformation to RuO_4 is observed. By annealing highly hydrated ruthenium dioxide at 144°C for 5 hours, a partially dehydrated form of $RuO_2.xH_2O$ can be formed. This state is highly catalytically active and stable under anodic conditions. This catalytic activity, however, decreases upon increase of the annealing temperature due to full dehydration of the particles. Thereby, the specific surface area becomes smaller and the degree of crystallinity is increased. At 900°C annealing temperature an anhydrous black powder will be formed. This anhydrous form of RuO_2 is well-known to be corrosion-resistant but due to its very low specific area it has a low catalytic activity for O_2 generation [155]. Here, in this work, nominally anhydrous RuO_2 is deposited on n-type Si to simultaneously protect it from degradation under anodic conditions and to provide an efficient O_2 catalyst for water oxidation.

4 Experimental section

4.1 Sample preparation

4.1.1 Ion-Layer-Gas-Reaction (ILGAR)

The ion layer gas reaction (ILGAR) process [156] is patented by the Helmholtz-Zentrum Berlin für Materialien und Energie. It is a cyclic process involving decomposition of an aerosol on a heated substrate followed by sulfurization to form a highly pure and conformal sulfide layer such as In_2S_3, Sb_2S_3, Bi_2S_3 and $CuInS_2$. The ILGAR method was first developed as dip-ILGAR [157] and later improved by an improved spray ILGAR technique [63] which allows deposition of sulfides on different substrates including planar and structured surfaces. The deposition rate is limited by the adhesion of the liquid film. To better control the deposition rate and for application in in-line processes the spray version of the ILGAR technique proved to be extremely valuable.

The spray ILGAR technique also can be modified for deposition of metal oxides in a way similar to spray pyrolysis. By this technique a precursor solution is nebulized with an ultrasonic nebulizer and directed towards a hot substrate by a nitrogen (N_2) flow as carrier gas. On the heated substrate the solution dries, decomposes and forms a metal oxide mixture in intimate contact with the substrate. Because of the simplicity of this method which does not require vacuum equipment it has been employed for deposition of thin films of metal oxides, spinel oxides, chalcogenides and superconducting compounds [158]. In this project, this technique was used for deposition of crystalline TiO_2 layers on $Cu(In, Ga)Se_2$ (CIGSe) substrates, using the setup shown in Figure 4.1. The precursor solution was 80 mL of titanium solution 0.01 M prepared by dissolving titanium diisopropoxide ($Ti(OCH(CH3)_2)_4$) from ALDRICH in ethanol (99.99%) and mixing in an ultrasonic bath for 10 min. The precursor solution was nebulized by the ultrasonic generator into a fine mist; the mist was then transported sequentially through the glass tube to the heated substrate (CIGSe) by the N_2 gas flow and decomposed and oxidized there.

Different spray times and temperatures were tested in order to find the optimum deposition parameters with respect to the resulting photoelectrochemical activity and stability upon evolution of hydrogen. Those optimal conditions were 40 min of spraying at 400°C. The thickness of the layer deposited at these conditions is around 300 nm. According to analysis by x-ray diffraction (XRD), surface-photovoltage measurements (SPV) and x-ray photoelectron spectroscopy (XPS), this layer is crystalline and contains high concentrations of carbon resulting from the organic solvent. In order to furthermore optimize the performance of the photocathodes, the TiO_2 layers were doped with Pt as hydrogen evolution catalyst. The 0.001 M Pt precursor was prepared by dissolving platinium-hexachloride from Sigma-Aldrich in ethanol. Three doping levels (2, 5 and 10 vol.% of the precursor solution) were tested to determine the optimum concentration level (results will be shown in 5.1.3).

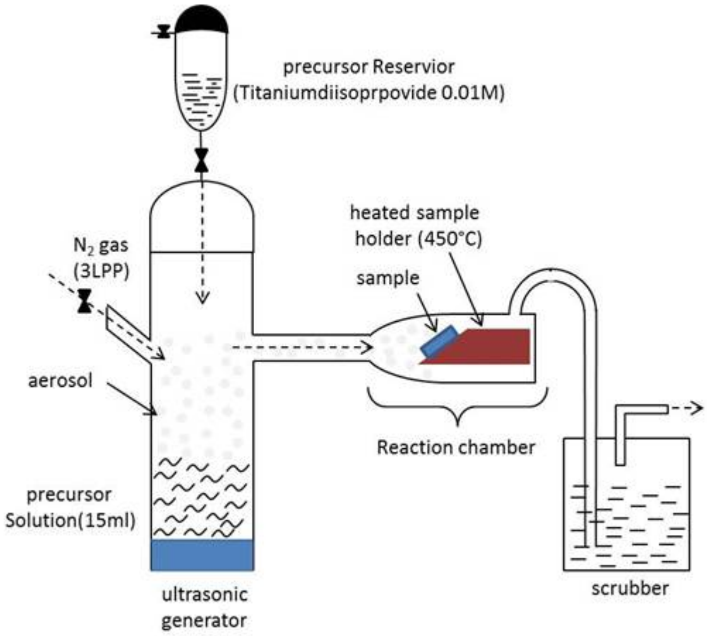

Figure 4.1: Schematic of the Ion-Layer-Gas (ILGAR) set-up for deposition of $\mathrm{TiO_2}$.

4.1.2 Electrophoretic deposition (EPD)

Electrophoretic deposition (EPD) is a deposition technique for nanoparticulate films [49-50,159], which is known since the work by Ruess et al. in 1808 by observing an electric field induced movement of clay particles in water. In this process powder material is dispersed in an organic solvent. Upon electrochemical equilibrium conditions surface charges form around the powder particles (lyoshphere formation) giving them a corresponding net momentum in the presence of an electrostatic field. There are several mechanisms causing charge formation on the particles [160] like (a) selective adsorption of ions onto the solid particle from the liquid (b) dissociation of ions from the solid phase into the liquid (c) adsorption or orientation of dipolar molecules at the particle surface and (d) electron transfer between the solid and the liquid phase due to differences in their work functions. This charge induction yields a net electrical charge on one side of the interfacial region and a charge of opposite sign on the other side, which is known as electrical double layer. The charged particles in the suspension, under the influence of a DC electric field, migrate in the bulk of the suspension towards the conductive electrodes. This migration step depends on the bulk properties of the suspension like conductivity, viscosity, particle concentration and the surface charge density of the particles (so-called zeta potential of the particles). Depending on which electrode the deposition occurs, two types of EPD are defined. I) Cathodic electrophoretic deposition: when the particles are positively charged and deposited on the cathode and II) anodic electrophoretic deposition: when the deposition of negatively charged particles occurs on the positive electrode (anode). The last step of the process is the coagulation and deposition of the particles on the electrode. The schematic of the EPD process is illustrated in Figure 4.2.

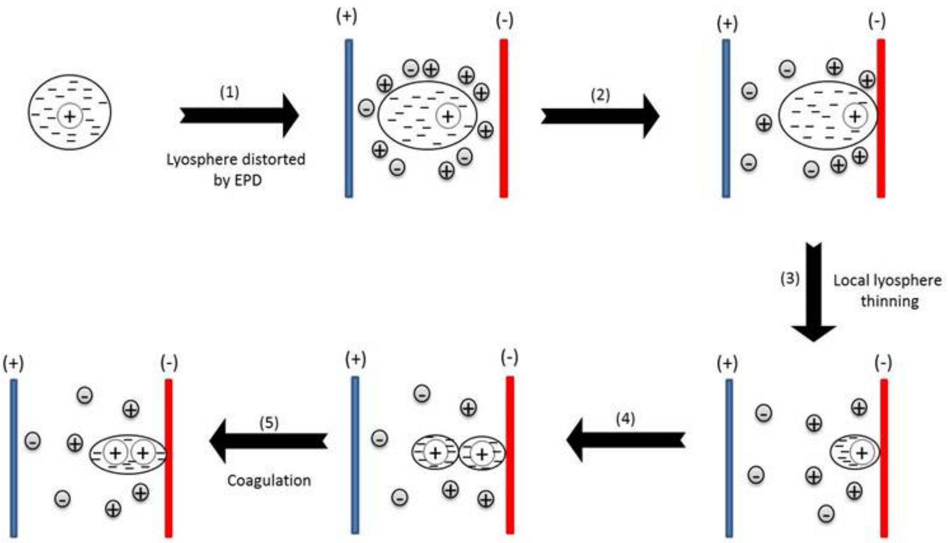

Figure 4.2: Schematic of the EPD process.

The quality of the EPD process depends on the amount of the particles reaching the electrode at a certain amount of time which is subject to the quality of the suspension. The parameters affecting the quality of the suspension are divided in two main groups, the ones related to the chemistry of the suspension such as particle size, conductivity, viscosity of the suspension and dielectric constant of the liquid and those related to the physical parameters such as the deposition time and the applied voltage. All these parameters are correlated in the well-known and widely used theory of electrophoresis as developed by Hamaker, [49-50, 159-160] Ishihara et al. [161] and Chen and Liu [162]. The Hamaker law states a direct relation between the deposited mass and the electrophoretic mobility of the solvent. The electrophoretic mobility (μ_e) of the particles in the suspension under the influence of a uniform electric field, determines the EPD rate and the velocity of the particles in suspension, as given by Eq. (4.1):

$$w(t) = \int_{t_1}^{t_2} \mu_e E A C_s dt \tag{4.1}$$

Here w(kg) is the deposited yield, $\mu_e(m^2V^{-1}s^{-1})$ is the electrophoretic mobility, E(Vm^{-1}) is the field strength, A(m^2) is the electrode surface area and C_s(kg/m^3) is the concentration in suspension. Ishihara et al. [161] and Chen and Liu [162] correlated the electrophoretic mobility (μ_e) to the zeta potential of the particles in suspension. The zeta potential indicates the amount of the charge on the surface of the particles suspended in the solvent and plays a role in the stabilization of the suspension by determining the intensity of repulsive interaction between the particles. The stability of the suspension is governed by the sum of attractive and repulsive forces between the particles, mainly of electrostatic and van der Waals nature. In order to prevent particle agglomeration, a high electrostatic repulsion due to high particle charge is required determining (i)the direction and migration velocity of the particles during EPD and (ii) the density of the deposit. The Zeta potential [163] is calculated according to Eq. (4.2):

$$\zeta = 3\mu_e \eta/(2\epsilon_0 \epsilon_r) \tag{4.2}$$

Here,ϵ_0 is the permittivity of free space (8.854e^{-12}(C/Vm)), ϵ_r and η are, respectively, the permittivity and viscosity of the suspension medium, ζ(mV) is the zeta potential of particles in suspension and μ_e ($m^2V^{-1}s^{-1}$) is the electrophoretic mobility of the particles in the solvent. The viscosity of the suspension is calculated by Einstein's formula [164] for the effective viscosity of a dilute suspension of rigid spherical particles in an ambient fluid, given by Eq. (4.3):

$$\hat{\eta} \approx \eta(1 + 2.5\Phi) \tag{4.3}$$

Here, η and Φ are the viscosity of the ambient fluid and volume fraction of spheres in the suspension respectively.

In this project, the EPD technique was used for preparation of (photo-)anodes. For alkaline electrolytes, ZnO:Co was chosen as catalyst for oxygen evolution. The pre-synthesized ZnO:Co catalyst (6 mg) was dispersed in 15 mL of an organic solvent and 3 mg iodine was added to the mixture as an oxidizing agent and stirred for 5 min in an ultrasonic bath. The electrophoretic deposition was carried out in a 10 mL beaker. Two fluorine-doped tin-oxide (FTO) samples (Solaronix, Suisse, sheet resistance (7 Ωcm^{-2})) were pre-cleaned by acetone and used as working and counter electrodes, respectively. The EPD set-up is schematically shown in Figure 4.3. After filling the beaker with the suspension, the electrophoretic deposition was carried out by applying -10 V to the support electrode using a BioLogic potentiostat, model VSP-300.

In order to investigate the effect of the organic solvents on the quality of the EPD process, three different organic solvents, ethanol, acetone and acetonitrile were used (results are shown in section 5.2). The chemical properties of these solvents are listed in Table 4.1.

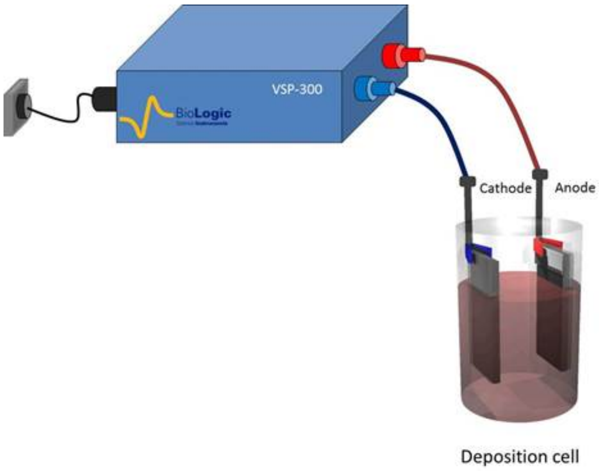

Figure 4.3: Schematic illustration of the electrophoretic deposition (EPD) set-up.

Silicon samples (n-type Si(111) and Si(100), doping density $N_D \sim 6 \times 10^{15}$, ABC Company, Germany) were pre-cleaned by ethanol and water and chemically etched in HF(50%) or NH_4F (40%) depending on the respective surface orientation: (I) Si(111) was etched in consecutive steps by NH_4F (100 s and 10 min, respectively) and finally dipped in HF (50%). (II) Si(100) was etched in a 3:1 solution of HF(50%) and ethanol for 30 s and 10 s with intermediate rinsing with water and drying with N_2.

Solvent	Chemica formula	Density	Dielectric constant	Viscosity	Dipole moment
Ethanol	$CH_3 - CH_2 - OH$	0.789 g/ml	24.55	1.2cP	1.7
Acetone	$CH_3 - C(=O) - CH_3$	0.786 g/ml	21	0.32cP	2.7
Acetonitrile	$CH_3 - C \equiv N$	0.786 g/ml	37.5	0.37cP	3.44
Toluene	$C_6H_5 - CH_3$	0.867 g/ml	2.38	0.59cP	0.36

Table 4.1: chemical and physical properties of the used solvents.

4.2 Analytical methods

4.2.1 Electrochemical analysis

Electrochemistry studies the chemical reactions taking place at the interface of an electrode and an ionic conductor called electrolyte. The charge flow, comprising ionic conduction in the electrolyte and electron flow in the outer circuitry is then monitored for analysis.

4.2.1.1 Current-Voltage (CV) behavior

Cyclic voltammetry (CV) is a technique for studying the electrochemical activity of the catalysts. In this method, the voltage is repeatedly scanned between two potential values and applied between the sample under investigation (the working electrode) and the counter-electrode. The absolute energetic position of the working electrode is measured against a calibrated reference electrode. This potential (E_1) is ramped linearly with time toward the second predetermined limit ($\mathsf{E}_2 = \mathsf{E}_1 + \Delta\mathsf{E}$). Simultaneously the current density is measured between the working electrode and the counter electrode and plotted vs. the applied potential. The forward scan will end when the potential reaches the final value (E_2). Then, the direction of the scanning steps is reversed and the backward scan continues toward the initial value (E_1) to complete the cycle. To investigate the photoactivity of the electrode these measurements were performed under illumination.

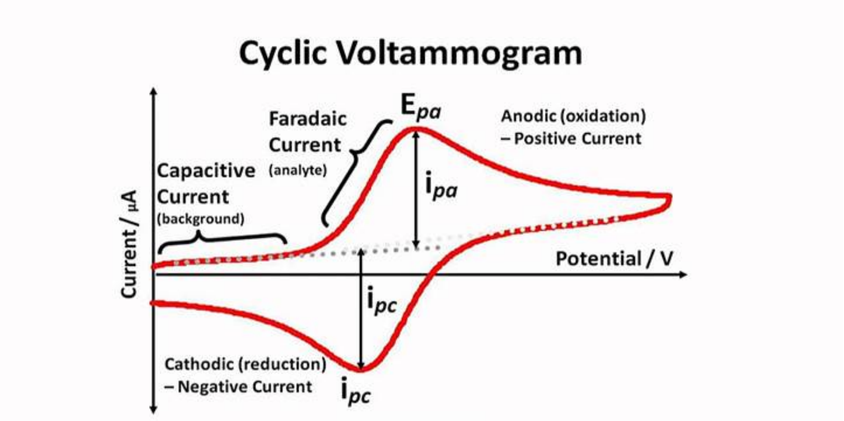

Figure 4.4: Typical cyclic voltammogram where i_{pc} and i_{pa} show cathodic and anodic peak currents, respectively, for a reversible reaction [165].

Typical CV measurements at the anodic region are shown in Figure 4.4. The recorded CV curves reveal several features indicative for the reaction mechanisms involved. The first part shows the capacitive current or non-faradaic current. This current is flowing through an electrochemical cell and is observed upon charging or discharging of the electrical double layer and does not involve in any chemical reaction. The second part is the faradaic current indicating charge transfer of electrons across the electrode-electrolyte interface. Depending on the direction of the voltage scanning, electrons are either gained or released by the electrodes. By scanning the voltage of the electrode to more negative values, the energy of the electrons in the electrode increases, providing thereby the electrons with sufficient energy to occupy vacant states on the species in the electrolyte. In this case reduction takes place like for hydrogen evolution. On the other hand, by driving the voltage more positive, the electrons in the electrode loose energy, thereby electrons from species in the electrolyte are transferred to the electrode. In this case oxidation takes place like in oxygen evolution. The faradaic process will be continued till all the material at the surface of the electrode is oxidized; the resulting peak is called anodic peak. After reaching the final potential the scan direction is reversed and reduction of the substrate continues until E_{pc} is reached where the reduction is finished. If the reaction at the surface is reversible, the integral ratio of cathodic current and anodic current is equal to 1.

Measurements described here were done in a three electrode configuration. The material to be tested was positioned as working electrode; two steel clips attached to the surface of the sample were applied as front contacts. The surface area of the working electrode, exposed to the electrolyte, was 0.5 cm^2. A platinum wire was used as counter electrode and the reference electrode was a KCl-saturated Ag/AgCl electrode. The reference electrode circuit uses a large series resistance ($> 10^{11}\Omega$) such that, practically speaking, no current exchange takes place. Therefore, it enables determination of the absolute value of the working electrode potential in a reliable way. All these three electrodes were connected through a potentiostat (Biologic VSP-300). A schematic of the used electrochemical cell is shown in Figure 4.5.

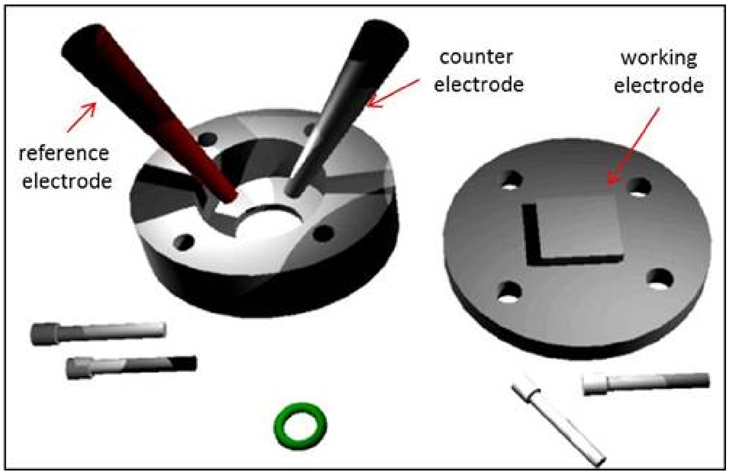

Figure 4.5: Schematic of the photoelectrochemical cell.

4.2.1.2 Incidence photon to charge carrier conversion efficiency (IPCE)

Incidence photon to to charge carrier conversion efficiency (IPCE) is a measure to characterize the efficiency of a photoelectrode to convert incident light into photoelectrochemical reactions. It is equal to the external quantum efficiency and is the ratio between the amount of collected carriers and the number of incident photons on the sample. The schematic of the setup is shown in Figure 4.6. The principle of IPCE measurements is based on illumination of the sample by monochromatic light and recording of the resulting photocurrent density. The setup consists of a 300W Xenon lamp from LOT-oriel GmbH as light source with a continuous spectrum from 200 nm to 700 nm. A Princeton Instruments (Acton, MA) SP2150i monochromator with entrance and exit slits of 1 mm was used to select light with defined narrow wavelength width. After passing the monochromator, the light beam was chopped by a shutter (LS6T2-NL, Vincent Associates, Rochester, NY) resulting in a periodic sequence of illumination and darkness in 2s time intervals. Thereby, the net photocurrent could be determined by subtraction of currents observed under illumination and in the dark.

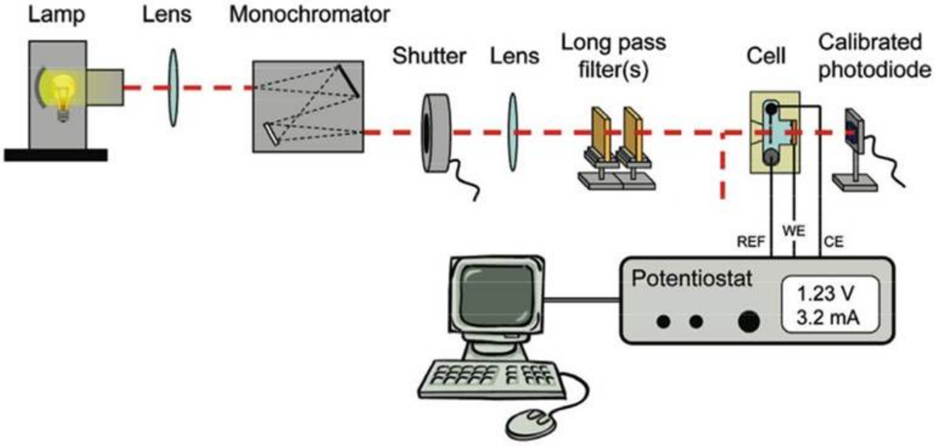

Figure 4.6: IPCE set up [3].

After passage of the light through two long-pass filters, used to remove higher orders of diffracted light, it illuminated the electrode in the PEC cell. A platinum wire was used as counter electrode. The electrodes in the PEC cell were connected to a PRS237A potentiostat (Ameteck Inc., Berwyn, PA) in order to apply a bias potential and to measure the current densities. The data were recorded by a LabView program, automatically decrementing the wavelength from 900 nm to 300 nm at a scan rate of 30 nm/min. The IPCE is calculated by Eq. 4.4 as below:

$$\mathrm{IPCE}(\lambda) = \frac{hc}{(q\lambda)} \frac{j_{\mathrm{photo}}(\lambda)}{P(\lambda)} \tag{4.4}$$

Here, c and λ are the speed and the wavelength of light respectively,q is the elementary charge, j_{photo} and P are the photocurrent density and the light power intensity at a given wavelength.
IPCE is also useful for studying the degradation behavior of devices. If the measurements show a decrease in IPCE during repeated cycles, deterioration of the photoconversion properties of the active material have to be assumed. A changing shape of the IPCE curve, on the other hand, may point to morphological alterations in the absorbing layer.

4.2.1.3 Mott-Schottky measurements

Mott-Schottky measurements were performed to study the semiconductor -electrolyte interface and to determine the flat band potential E_{FB} and the charge carrier concentration N_D of the photoelectrodes. The measurements were carried out in the dark using a Zahner Messystem electrochemical workstation, IM6, combining a potentiostat and a frequency response analyzer. A potential range from 1.5 V to -0.5 V was applied on the sample with oscillation amplitude of 10 mV with frequencies of 50 kHz, 13 kHz, 8 kHz and 3kHz, respectively. The space charge capacitance (C_{sc}) was measured as a function of the applied potential (E). Results were plotted as $1/(C_{sc}^2)$ vs. E, allowing the extrapolation of N_D from the slope and E_{FB} from the intercept with the horizontal axis. This approach follows from the Mott-Schottky equation [166] (Eq. 4.5):

$$\frac{1}{C_{sc}^2} = \frac{2}{q\epsilon\epsilon_0 N_D A^2}(E - E_{FB} - kT/q) \tag{4.5}$$

Here, ϵ_0 is the permittivity of free space and ϵ is the relative dielectric constant of the material of the photoanode. A is the cross sectional area exposed to the electrolyte, N_D is the charge carrier concentration, E is the applied potential, E_{FB} is the flat band potential and k is the Boltzmann constant.

4.2.1.4 Differential electrochemical mass spectroscopy (DEMS)

Differential electron mass spectroscopy (DEMS) [167-168] was used to detect the produced gases during cyclic voltammetry. The inlet system between the electrochemical cell and the differentially pumped vacuum system of the mass spectrometer (Balzers; QMI 420, QME 125, QMA 125 with 901 off axis SEM) consists of a porous hydrophobic membrane, covered with a 100 nm thick Au-layer. This layer serves as contact area to the working electrode. Oxygen or hydrogen, which is formed in an electrochemical experiment at the working electrode, diffuses to some extent into the mass spectrometer where it is monitored simultaneously with the electrochemical data. A schematic of the cell is shown in Figure 4.7. All experiments were carried out in N_2 purged atmosphere at scan rates of 2 mVs^{-1}. As reference, an Ag/AgCl electrode (+290 mV NHE) and as a counter electrode a Pt-wire were used. For alkaline electrolytes KOH 1N pH 14 and NaOH 0.1M pH13, and for acidic electrolyte H_2SO_4 0.5M pH0.3 and for buffer solution kPi ph7 were used.

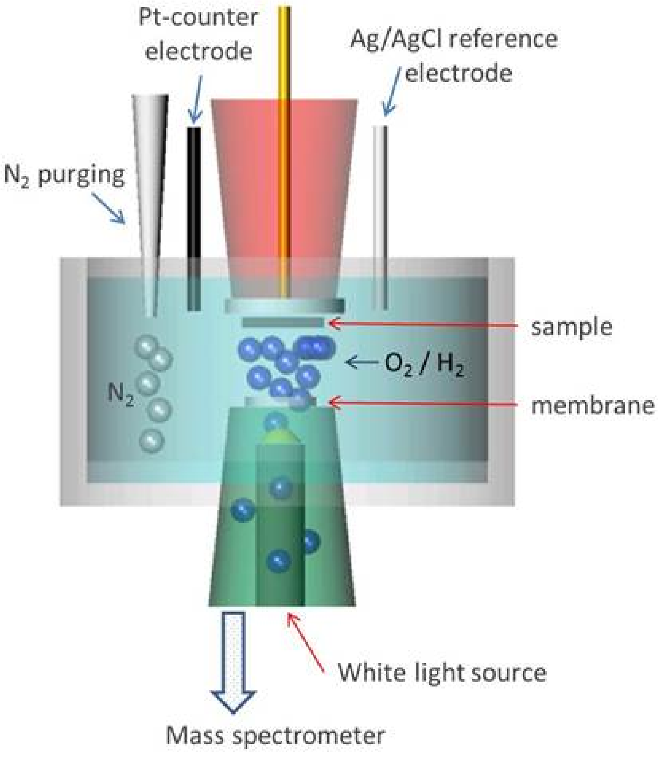

Figure 4.7: Schematic of the Differential Electrochemical Mass Spectroscopy (DEMS) setup.

4.2.2 Spectroscopic analysis

4.2.2.1 Grazing incidence X-ray diffraction (XRD)

X-ray diffraction (XRD), carried out in (conventional) reflection mode, is a method used for phase identification of crystalline materials and atomic spacing. With this method, X-rays penetrate the entire sample's volume. Therefore, the sensitivity of the method is highest with respect to the distance of atomic planes parallel to the surface. The most important feature is that the incident angle corresponds to half of the scattering angle.

A corresponding mode is the grazing incidence technique which is applied in order to enhance the sensitivity for scattering contributions from the film and to suppress contributions from the substrate. In this mode the X-rays are impinging on the surface at an angle α_i and the scattering occurs only in the horizontal plane. The x-ray photons are then collected at an angle $\alpha_f = \alpha_i$. At low incidence angles the absorption mainly limits the penetration depth of the radiation and therefore the gained information can mainly be attributed to the surface. An X-ray diffractometer consists of three basic elements: an X-ray tube, a sample holder, and an X-ray detector. A schematic of the setup is shown in Figure 4.8.

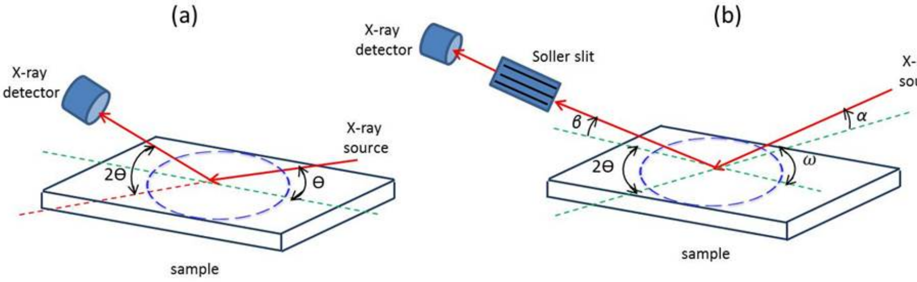

Figure 4.8: (a) X-ray diffraction in reflection mode. (b) Grazing incidence X-ray diffraction (GIXRD) mode.

X- rays are produced by bombarding a metal target (Cu, Mo) with a beam of electrons emitted from a heated filament (often tungsten). The incident beam will ionize electrons from the K-shell (1s) of the target atom and x-rays are emitted as the resulting vacancies are filled by electrons dropping down from the L (2p) or M (3p) levels. This gives rise to K_α and K_b lines. Filtering, by foils a crystal monochromator, is required to produce monochromatic X-rays needed for diffraction. These X-rays are collimated and directed onto the sample. As the sample and detector are rotated, the intensity of the reflected X-rays is recorded. When the geometry of the incident X-rays, impinging on the sample, satisfies the Bragg Equation constructive interference occurs and a peak in intensity is observed. A detector records and processes this X-ray signal and converts the signal to a count rate which is then transferred to a device such as a printer or computer monitor. In this project, the crystallinity of TiO_2, ZnO:Co and RuO_2 layers was measured by means of grazing incidence X-ray diffraction (XRD) in Bragg-Brentano geometry, using a Bruker AXS (D8 Advance) diffractometer. In order to achieve high resolution and an excellent signal to noise ratio the X-ray beam was directed via a Göbel mirror. For detecting the diffracted radiation, a SOL-X energy dispersive detector was employed. The measured diffractograms were analyzed with the software EVA3. The radiation source used was Cu-K alpha with a wavelength of 1.5406 Å. The size of the crystal (t) in a sample is estimated from the width of the measured diffraction peak using the Debye-Scherrer correlation [169]:

$$t = 0.9\lambda/(\beta.\cos\theta) \tag{4.6}$$

Here, t is the crystal size, λ is the wavelength of the incident radiation, β is the width of the diffraction peak which is determined at full width of half maximum of the signal peak.

4.2.2.2 Surface photoelectron spectroscopy(PES)

Photoelectron spectroscopy (PES) is a non-destructive surface-sensitive technique for analyzing the surface chemistry of a material by measuring the kinetic energy of photoelectrons emitted from the sample due to the photoelectric effect. The photoelectric effect describes the emission of electrons from the surface when the surface is hit by electromagnetic radiation. Depending on the source of the ionization energy, PES is divided in to two categories (I) Ultraviolet Photoelectron Spectroscopy (UPS) which uses noble gas discharge lamps like He as the source of radiation with excitation energies lower than 41 eV and (II) X-ray photoelectron Spectroscopy (XPS) which uses X-ray excitation energies in the range of 1000-1500 eV. UP excitation is used to assess the valence band, whereas XPS can characterize deep core-levels. The comparison of UPS and XPS is shown in Figure 4.9.

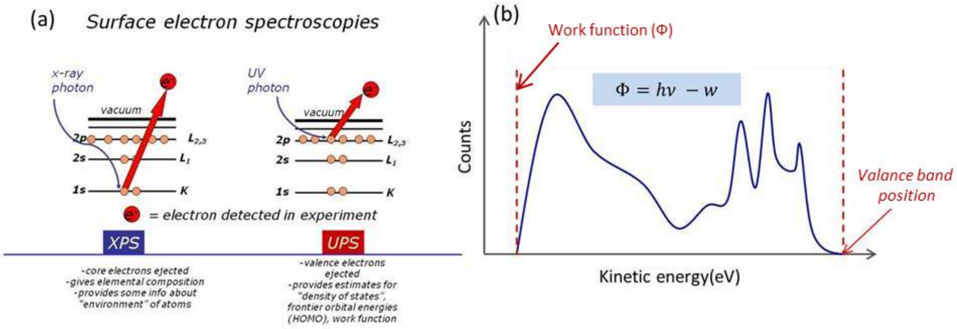
(a)
Surface electron spectroscopies
x-ray photon
vacuum
2p
2s
1s
$L_{2,3}$
L_1
K
UV photon
vacuum
2p
2s
1s
$L_{2,3}$
L_1
K
= electron detected in experiment
XPS
-core electrons ejected
-gives elemental composition
-provides some info about "environment" of atoms
UPS
-valence electrons ejected
-provides estimates for "density of states", frontier orbital energies (HOMO), work function
(b)
Work function (Φ)
$\Phi = h\nu - w$
Counts
Valance band position
Kinetic energy(eV)

Figure 4.9: comparison between UPS and XPS[170].

All measurements were performed under high vacuum conditions at 3.4×10^{-10} mbar. For XPS measurements, a monochromatized Al X-ray source was used. The X-rays excite photoelectrons in the sample mostly in the first 10 nm of the surface layer which restricts the so-called information depth to a very thin surface film. If the binding energy of the excited electrons is lower than the excitation energy (here less than 1486.74 eV) the electrons will be emitted as photoelectrons and detected in a channeltron analyzing detector. The entire excitation process can be conceived to occur in three steps:

I) The atom will absorb the photon and its energy is transferred to an electron.

II) The excited electron will travel to the surface of the sample. During this motion the electron can lose some of its kinetic energy by scattering processes.

III) The excited electron will be released from the surface into the vacuum. An electron analyzer measures the kinetic energy and the number of emitted photoelectrons.

In the used set-up, a PHOIBOS analyzer 100 served as detector with 5 channels and diameter of 100 mm. An XPS spectrum was obtained as plot of number of detected electrons versus the binding energy, calculated according to Eq. 4.7 [171].

$$E_K = h\nu - E_B - \Phi_{spec} \tag{4.7}$$

Here, E_K is the kinetic energy of the photoelectrons measured by the system, E_B is the binding energy of the emitted electrons, $h\nu$ is the energy of the X-ray photons, ν is the frequency of the incident light and h is Planck's constant ($h = 6.626 \times 10^{-34}\,Js$). The aluminum X-ray source provided an excitation energy of 1486.7 eV. Φ_{spec} is the work function of the XPS system, a constant value that depends on the material properties of the spectrometer, which has to be determined prior to sample analysis (4.287 eV). Typically, the energy-dissipative curve of an XPS survey can show various features in the spectrum to be associated to different emission processes [172]:

I) Sharp peaks due to photoelectrons created within the first few atomic layers (elastically scattered).

II) Spin-orbit splitting (if incomplete filled shells contain unpaired electrons).

III) A broad background structure due to electrons from deeper regions of the solid which are ineslastically scattered (reduced EK).

IV) Satellite structures, which arise when a core electron is removed by photoionization. In this case, a sudden change of the effective charge occurs due to the loss of shielding electrons. This kind of peaks has two forms:

  - Shake-up satellites: the emitted electron interacts with a valence electron and excites it (shakes it up) to a higher energy level. As a consequence the energy of the core electron is reduced and a satellite structure appears a few eV below (EK scale) the core level position.
  - Shake-off satellites: the valence electron is ejected from the atom completely (to the continuum). This effect is visible as broadening of the core level peak or as contribution to the background signal.

V) Plasmons which are created by collective excitations of valence band electrons:

  - Extrinsic Plasmon: excited as the photoelectron propagates through the solid after the photoelectric process.
  - Intrinsic Plasmon: screening response of the solid to the sudden creation of the core hole in one of its atoms.

VI) Auger peaks produced by X-rays (transitions from L to K shell: O KLL or C KLL).

These peaks are well defined in terms of the binding energy of the electronic states of the atoms. Depending on the number of the protons in the atom, these binding energies can be specified for each atom. Figure 4.10 shows the relation between electron binding energies and atomic number (Z).

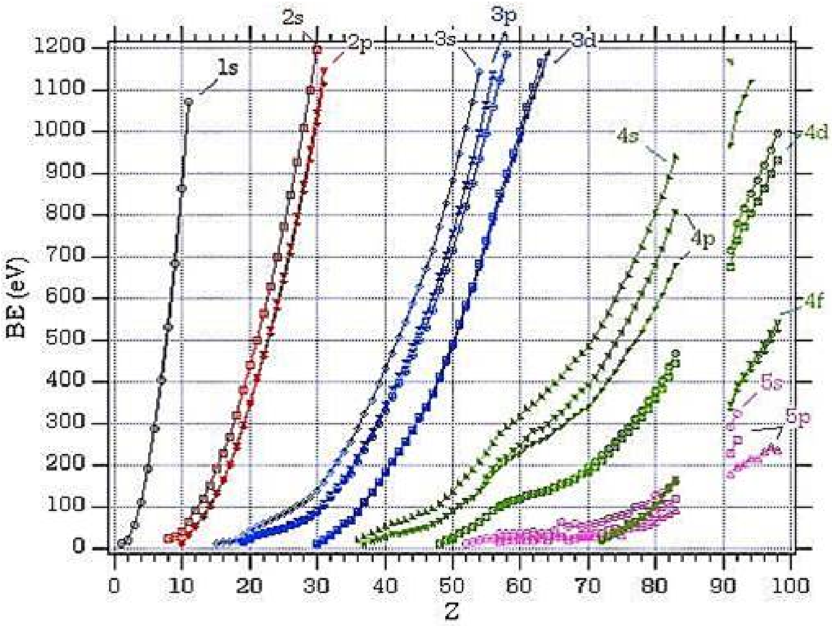

Figure 4.10: Relation between electron binding energies and atomic number (Z)[173].

Assignment of the core-level lines to specific oxidation states was done by using published data (J. Chastain and R. C. King Jr. (Eds.), Handbook of X-Ray Photoelectron Spectroscopy, Physical Electronics, Inc., Minnesota, USA (1995) and the XPS data base of the National Institute of Standards and Technology, NIST, USA). By comparison of these binding energies with the references, the elemental composition, the chemical state and the electronic state of the elements within a material can be characterized. The machine used in this project for surface chemical analysis was an XPS-ESCA system (Specs, Germany).

4.2.3 Morphological-chemical analysis

4.2.3.1 Scanning Electron Microscopy coupled with Energy Dispersive X-ray (SEM/EDX) Analysis

Scanning Electron Microscopy (SEM) and Energy Dispersive X-ray (EDX) are non-destructive methods for obtaining high resolution morphological and chemical analysis of samples. In these measurements the surface of a sample is bombarded with electrons emitted from a heated tungsten filament or from a field emission cathode. The energy of the incident electrons depend on the evaluation objectives and lies between 100 eV and 30 keV. The depth of the penetrating of the beam ranges from 10 to several 100 nm and is related to the spatial resolution of the data. Figure 4.11 shows the interaction of the incident electron beam with a sample. The interaction of this high energy beam with the sample results in a variety of signals: (I) secondary electrons (II) backscattered electrons (BSE), (III) visible light, (IV) X-ray photons and (V) Auger electrons. Secondary electrons and backscattered electrons are commonly used for microscopic imaging of the samples. The analysis of secondary electrons serves for analysis of the sample's surface morphology while backscattered electrons allow for achieving high contrasts in the composition of multi-phase samples. The intensity of backscattered electrons is correlated to the atomic number of the element within the sampling volume.

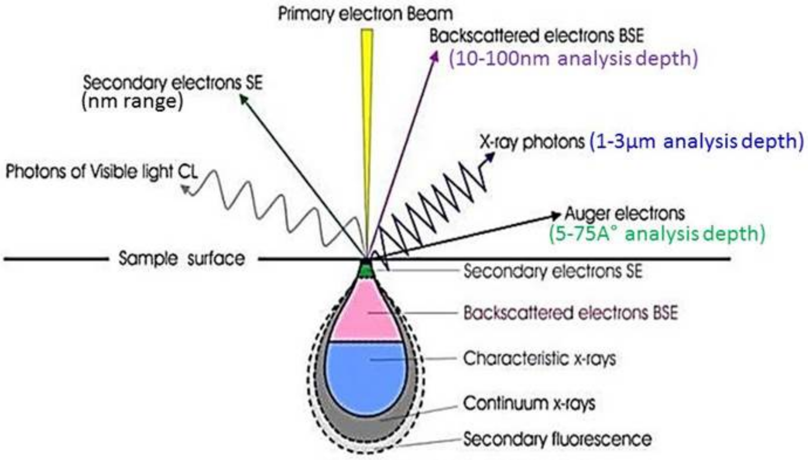
Primary electron Beam
Backscattered electrons BSE
(10-100nm analysis depth)
Secondary electrons SE
(nm range)
X-ray photons (1-3µm analysis depth)
Photons of Visible light CL
Auger electrons
(5-75A° analysis depth)
Sample surface
Secondary electrons SE
Backscattered electrons BSE
Characteristic x-rays
Continuum x-rays
Secondary fluorescence

Figure 4.11: Interaction of the electron beam with a sample in SEM [174].

Depending on the filling form of the vacancies created by the secondary electrons, two types of signals can be detected: Auger electrons and X-ray photons. In Auger emission, the remaining hole belongs to inner shells e.g. to the K shell, and is filled by an electron from an outer shell (L1). The released energy is transferred subsequently to another electron (here: L3) which is then ejected as Auger electron. X-ray photons are emitted when the vacancies, created by secondary electrons, are filled with electrons from higher orbital levels and the released energy is emitted as a photon. X-rays provide information about the elemental composition of the sample and they are detected by an energy dispersive detector that displays the signal as a spectrum of intensity versus X-ray energy.
Here, the morphology of the semiconductor was investigated by a scanning electron microscope (SEM), LEO Gemini 1530, from Zeiss, Germany, and a Thermo Fisher EDX system. The EDX software, used for elemental analysis, was ”Noran System Six” (NSS). The thicknesses of the samples were determined by using a Veeco-Dektak 8 stylus profilometer [175] which measures the vertical displacement of a diamond tip electromechanically. The gantry moves the stylus with adjustable speed and force across the surface of the sample. A stylus with a radius of 12.5 µm was used.

4.2.3.2 Transmission Electron Microscopy (TEM)

Transmission electron microscopy is a microscopy technique in which the sample is characterized by a beam of electrons. Since in TEM electron beams are used as probe signal, much higher resolution is achieved in comparison to light microscopes due to the much shorter wavelength associated to electrons. The TEM set-up has three main parts: (I) the electron gun to produce the electron beam and a condenser to focus the beam on the object, (II) a series of lenses, a movable specimen stage, and (III) an image recording system that consists of a fluorescent screen for viewing and focusing the image and a digital camera. To prepare a cross-sectional sample, the specimen is cut into two small slices and glued on each other with epoxy in a face-to-face configuration. The area size of the slices is about 0.5 mm^2 each. The sample is subsequently thinned to about 4-6 microns and polished by ion milling. TEM measurements were carried out under vacuum conditions. The electron beam hit the specimen and passed through it. Depending on the state of the material (amorphous, crystalline phase, lattice constant etc.) some of the electrons are scattered and are not detected. Behind the sample at the bottom of the microscope, electrons, not affected by scattering, hit a fluorescent screen. As result, a gray image with varying contrast is obtained in dependence on the amount of scattered electrons. In this project, the microscope C5, 12 from Phillips equipped with a LaB6 cathode (lanthanum hexaboride) was operated at an accelerating voltage of 120 kV. The material under investigation present in thin layers was embedded in epoxy resin and cut with an Ultramikroton by Reichert & Young using a diamond knife (diatoms) at an angle of 45°.

4.2.4 Optical analysis

4.2.4.1 Ultraviolet-visible spectroscopy

Ultraviolet-visible spectroscopy is an optical method which measures the transmittance or reflectance of light after interaction with a sample as a function of the wavelength. It contains information about the optical band gap, the type of the band gap (direct or indirect) and the absorption coefficient of the material. The principle of UV-VIS spectroscopy is based on irradiation of a sample with light of the visible and ultraviolet spectrum. Molecules containing bonding electrons (π) or non-bonding electrons (n-electrons) will absorb the energy of the incident light and these electrons will be excited to higher anti-bonding molecular orbitals. As a result, the intensity of the impinging light attenuates along the penetration path [110]. Optical measurements of thin films were performed using a Perkin Elmer Lambda 950 UV/VIS spectrometer equipped with an integrating sphere, the used light spectrum was in the range of 200 nm to 800 nm, and transmittance or reflectance spectrums were measured. The absorption (A) was calculated by the relationship:

$$A + T + R = 1 \tag{4.8}$$

Here, T refers to the transmission and R to the reflection coefficient, respectively.
In order to determine, how far light of a particular wavelength can penetrate into a material before it is absorbed, the absorption coefficient was calculated using the Beer-Lambert Law [172]:

$$I(t) = I_0 exp(-\alpha t) \tag{4.9}$$

Here, α is the absorption coefficient and I(t) is the intensity of the transmitted light after passing through the sample with thickness t. I_0 is the incident intensity. I(t) and I_0 are equal to T and (1-R) respectively, therefore

$$T = (1 - R) exp(-\alpha t) \tag{4.10}$$

The absorption coefficient depends on the material and also on the wavelength of the light. A low absorption coefficient indicates that light is only poorly absorbed. If the material is thin enough, it will appear almost transparent to that wavelength. The intersection of the absorption coefficient with the wavelength-axis is equal to the band gap of the material. Near the band gap of the material, the absorption coefficient is given by Eq. (4.11)[110]:

$$\alpha \propto (h\nu - E_g)^m \tag{4.11}$$

Here, $h\nu$ is the photon energy and m is a constant that determines whether the material has a direct band gap or indirect band gap. For direct band gap materials, m is equal to 1/2 or 3/2. For indirect band gap materials, excitation of electrons is accompanied by absorption or release of a phonon in order to conserve the momentum, and m is equal to 2 or 3.

4.2.4.2 Fourier Transform Infrared Spectroscopy (FTIR)

Fourier Transform Infrared Spectroscopy (FTIR) is a nondestructive optical method for material analysis. The method applies illumination of the sample with infrared (IR) light. Some of the frequencies will be absorbed due to vibrational excitation of the bonds of the atoms. These frequencies are detected as characteristic absorption features. The strength of these peaks corresponds to the amount of the respective species in the material. Since each different material is composed of unique atomic bonds, none of them produce the same FTIR fingerprint. The FTIR spectra of solutions and deposited films were measured using a Bruker TENSOR 27 FTIR Spectrometer with OPUS software.

4.2.4.3 Surface photovoltage spectroscopy (SPV)

Surface Photo Voltage spectroscopy (SPV) [176] is a contactless and highly sensitive method for measuring light induced charge separation in conductive layers. With this technique photo-induced charge separation at the surface is detected in the presence of an external voltage. Thereby, information about the absorption edge and distribution of surface states is obtained and separation and recombination mechanisms can be characterized [177-178].

An SPV signal arises whenever there is an asymmetry in the separated charge and therefore a change in the surface work function. This change can occur when photogenerated charge carriers are separated in space or when non-uniform generation and recombination of charge carriers is present. Depending on the amount of charge (Q) separated in space and the distance (d) between the centers of the separated charges, the resulting SPV signal is given by Eq. 4.12 [179]:

$$\mathsf{SPV} = \frac{\mathsf{Qd}}{\epsilon \times \epsilon_0} \tag{4.12}$$

Here, the constant ϵ is the relative dielectric constant of the layer and $\epsilon_0 = 8.85\times10^{-14}$ F/cm. The SPV signals is measured in two configurations: (a) in the Kelvin probe mode and (b) in the fixed capacitor mode (Figure 4.12). In the Kelvin probe mode, the contact potential difference (CPD) is measured between the sample and a vibrating metal electrode in the dark and under steady light illumination. The metal electrode and the sample form a capacitor whose capacitance changes due to the vibration of the electrode. A voltage is applied to counter the alternating current generated by the varying capacitance. Under illumination, the capacitance changes which leads to a change in the applied voltage. The change in the applied voltage is equivalent to the change in the CPD. The difference ($\Delta\mathsf{CPD}$) between the CPD in the dark and under illumination represents the SPV signal.

In the fixed capacitor mode, which was used in this project, measurements were done at room temperature under low vacuum of 10^{-2} mbar. A thick (10-30 μm) mica sheet was placed between the sample and the electrode (cylindrical $\mathsf{SnO_2 : F}$). The sample, mica sheet and an FTO electrode were pressed together by using a cardanic spring to form a parallel plate capacitor. The capacitance of this arrangement was of the order of 100 pF. Then the sample was illuminated by a halogen lamp. The incident light was chopped at a frequency of 8 Hz. When the sample is illuminated, the change in the surface potential results in a change in capacitance.

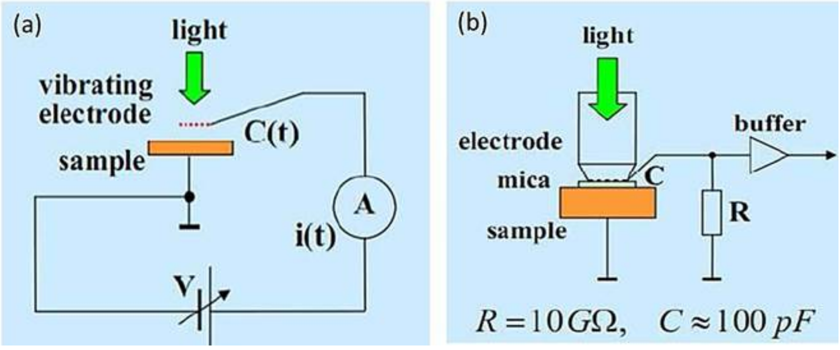

Figure 4.12: (a) Kelvin probe mode and (b) Fixed capacitor mode.

As SPV signal, the change in capacitance is measured across the measurement resistance (10 GΩ) using a lock-in amplifier (EG & G, 7260 DSP). The lock-in amplifier measured the signal in-phase (X) and by a 90° phase shifted signal (Y) with respect to the chopped light. The in-phase (X) signal contains information about the direction of charge separation: a positive or negative X signal implies that photo-induced electrons are separated towards the internal or outer surface, respectively. The 90° phase shifted signal (Y) characterizes the phase shift between the SPV signal and the chopped light, the amplitude (R) and phase angle (φ). The SPV amplitude R and phase angle φ are determined from the signals X and Y as shown below:

$$SPV_{amp} = R = \sqrt{X^2 + Y^2} \tag{4.13}$$

$$\varphi = tan^{-1}(Y/X) \tag{4.14}$$

The X and Y signals can be positive or negative, the sign of the signals depends on the direction of charge separation and how fast the charge separation is. A positive X signal and negative Y signal indicate that charge separation of electrons proceeds towards the internal surface, and the magnitudes of the signals depends on how fast this charge separation occurs. Fast charge separation leads to a high positive X signal and a low negative Y signal and slow charge separation leads to a low positive X signal and a high negative Y signal. If the X signal is negative and the Y signal gets positive, this case indicates charge separation towards the external surface. In this case, if the charge separation is fast, a high negative X signal and low positive Y signal is measured but upon slow charge separation, a low negative X signal and high positive Y signal will be measured. The R signal shows the maximum amplitude and the onset of the SPV signal which is a signature of the mobility band gap. It includes contributions from charge separation from states below the band gap. It should be noted that this band gap is related to the density of electronic defect states and has to be distinguished from the optical band gap. By dividing the normalized R signal with respect to the photon flux, a fit of the band edge by an exponential function results in the energy of the tail states:

$$\frac{R_{normalized}}{\phi_{photonflux}} = Aexp(\frac{h\nu}{E_{tail}}) \tag{4.15}$$

The energy of tail states indicates the distribution of defect states within the band gap of the material. The phase angle of the SPV signal gives information about the direction of charge separation. Values of 0° and 180° for φ or close to them mean a fast spectral response and values close to ±90° implies a slow time response [180].

5 Results and discussions

Solar-driven splitting of water into hydrogen and oxygen requires a complex and concerted activity of two electrodes, cathode and anode, under illumination [77-78]. For this purpose, state of the art semiconductors are presently employed with increasing success but necessitate consideration of a number of serious boundary conditions [80-82]. The electrode design has to ensure that photons are efficiently converted to charge carriers and that charge transport is not limited by junction barriers or ohmic losses. Most important, surface protection (of the semiconductor) has to be realized such that long-term operation in aqueous electrolytes is guaranteed. In this work, commercial chalcopyrite and silicon absorbers are used as fundamental photoelectrodes. This chapter contains the experimental results obtained in this study and is divided in two main sections. The first section includes the preparation and characterization methods of the novel photocathode based on chalcopyrite as an absorber and TiO_2 as conductive protection layer for hydrogen evolution.

The second section introduces electrophoretic deposition as an effective technique to deposit presynthesized catalysts on conductive substrates for preparation of (photo-)electrodes. Two case studies based on this method were performed with pre-synthesized ZnO:Co and RuO_2 in order to prepare electro/(photo-)anodes for alkaline and acidic electrolytes, respectively. Silicon (n-type Si(100), doping density $N_D \sim 6 \times 10^{15}$, ABC Company, Germany) serves as an absorber for photoanode preparation. In the subsections, the electrodes were characterized by:

I) Optical measurements to determine the transmission, reflection and absorption behavior of the thin films (UV-VIS), and the molecular fingerprint of the sample (FTIR).

II) Spectroscopic analysis to establish the phase (GIXRD), elemental composition and chemical state of the elements, relative composition of the constituents in the surface region and the valence band structure and oxidation states (XPS).

III) Morphological-chemical analysis to identify the homogeneity and elemental composition of the films (SEM/EDX).

IV) PEC performance under at $100\,mWcm^{-2}$ illumination intensity. This characterization also includes mass spectroscopy (DEMS), and incident photon to charge carrier conversion efficiency (IPCE).

5.1 Characterization of doped $TiO_2/Cu(In,Ga)Se_2$ photocathodes

As discussed in chapter 2, for developing an efficient photocathode, the use of relatively small band gap materials (i.e., 1.1-1.7 eV) is desired in order to efficiently absorb light in the range of the terrestrial solar spectrum.

Simultaneously, the respective positions of conduction band minimum and valence band maximum have to be adapted to the standard potentials of H_2 evolution. One of the suitable groups of materials in this respect are polycrystalline chalcopyrite films. Chalcopyrite thin film absorbers such as $CuInS_2$, $Cu(In,Ga)Se_2$, and $CuGaSe_2$, are very attractive candidates for solar-driven evolution of hydrogen because they have suitable band gap energies (≈ 1.0-1.7 eV) [24-26] and can, in principle, produce a significant portion of the required photovoltage. The advantage of chalcopyrite-based materials, besides having the right potential for hydrogen evolution, is their ability to absorb light in the entire visible range, resulting in high photocurrent densities, with values of up to 38 $mAcm^{-2}$ for world record $Cu(In, Ga)Se_2$ based solar cells and photovoltaic conversion efficiency beyond 20% [27].

The stability of ZnO/CdS/$Cu(In, Ga)Se_2$ device-grade solar cells in water under illumination turns out to be a severe problem [32]. The ZnO layer (TCO layer of the solar cell) is well-known to be unstable in aqueous environments [181]. Hence, the aim of this project is the development of a composite (or heterojunction) device based on p-type $Cu(In, Ga)Se_2$ device-grade chalcopyrite and an appropriate n-type transparent conductive oxide (TCO), stable under photo-corrosive conditions.

One of the most promising TCO candidates is TiO_2. The deposition method for preparation of TiO_2 films is the spray ILGAR technique described in detail in section 4.1.1. The first part of this chapter reports the optimum deposition temperature of the TiO_2. In the second part, the performance of the chalcopyrite solar cell with and without TiO_2 is compared. In the third part, Pt is introduced, firstly, as a catalyst to enhance the HER rate and, secondly, as a dopant to optimize the conductivity of TiO_2.

5.1.1 $Cu(In, Ga)Se_2$ as an absorber in heterojunction photocathode

In order to identify the optimum multi junction photocathode based on a chalcopyrite solar cell, three architectures were tested. In a first configuration, TiO_2 was deposited directly on the TCO layer (ZnO) of the solar cell. In a second configuration, the ZnO layer was removed and TiO_2 was deposited on the buffer layer (CdS). In a third configuration, both ZnO and the buffer layer were removed, and the TiO_2 film was deposited directly on the CIGSe absorber. The current-voltage behavior of these three different multi junctions in H_2SO_4 0.5 M is depicted in Figure 5.1. Dark current densities are throughout shown in blue color while corresponding photocurrent densities are shown in red color. The solid curves show the performance of the multi junction photocathode with TiO_2 top layer deposited by ILGAR. Dashed curves show the performance of the same composite without TiO_2 layer at the top. Figure 5.1(a) compares the current-voltage behavior of the chalcopyrite solar cell in H_2SO_4 0.5 M in the dark (blue dashed curve) and under illumination (red dashed curve). In this figure, it is shown that the chalcopyrite solar cell degraded immediately after getting in contact with the electrolyte. This results clearly proves that ZnO is not stable in aqueous media. In order to protect the ZnO from corrosion and benefit from the solar cell photovoltage, a TiO_2 layer was deposited on the TCO of the solar cell (by ILGAR process at 400°C for 40 min). As shown in Figure 5.1(a), in this case the activity of the photocathode in the dark (blue solid line) and under illumination (red solid line) is the same, i.e. a high dark current and no photo activity is observed. This observation points to an instability of the ZnO film during the ILGAR process. Therefore, the entire junction was compromised already during the ILGAR preparation process.

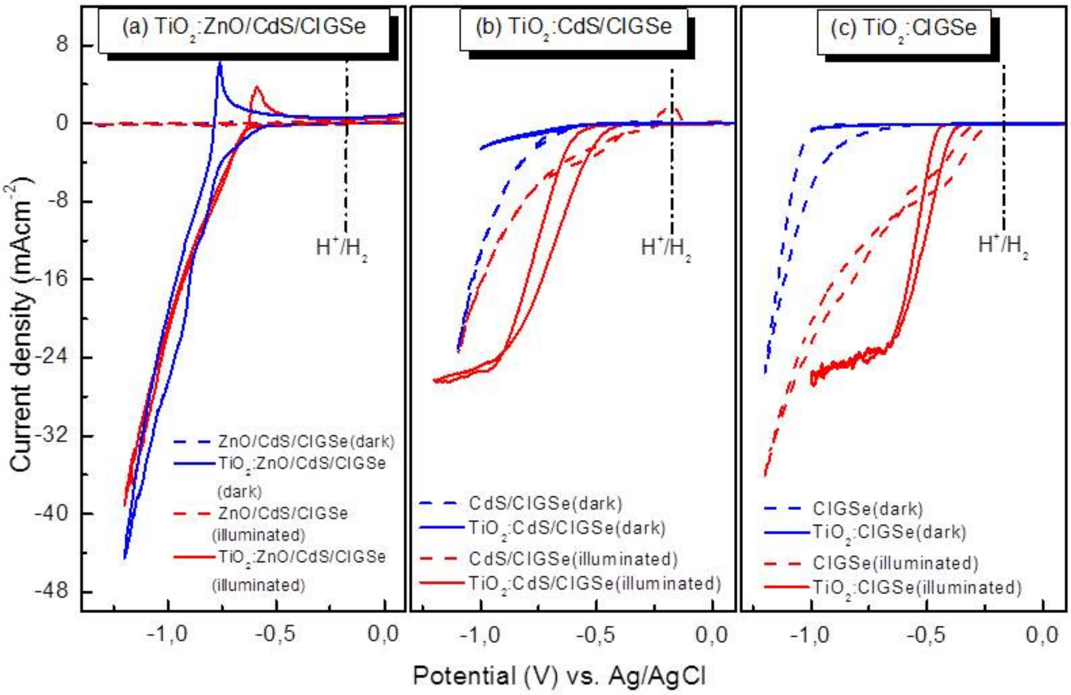

Figure 5.1: Current-voltage behavior (a) TiO_2:ZnO/CdS/CIGSe (solid line) and ZnO/CdS /CIGSe (dashed line), (b) TiO_2:CdS/CIGSe (solid line) and CdS/CIGSe and (c) TiO_2:CIGSe (solid line), bare CIGSe (dashed line).

According to the second configuration, the ZnO layer of the solar cell was removed in order to use the remaining $CdS/Cu(In,Ga)Se_2$ junction as support (and absorber). Electrochemical results are shown in Figure 5.1(b). The activity of this heterojunction in the dark (dashed blue curve) and under illumination (dashed red curve) was similar to the solar cell, i.e. fast degradation was observed and the samples did not show any photoactivity. After deposition of TiO_2 on CdS (buffer layer) the performance of the multi-junction photocathode improved. The dark current were limited to lower values of 3 $mAcm^{-2}$ at 1.1 V (blue solid curve). Under illumination the photoelectrode reached a saturation current density of 25 $mAcm^{-2}$ at 1.1 V (red solid curve). Despite this considerable improvement, this heterostructure is still characterized by a high overpotential with respect to the thermodynamic potential of 500 mV. One of the reasons, causing this increased overpotential, is considered to be interdiffusion of CdS at high temperature with the $Cu(In,Ga)Se_2$ absorber during ILGAR deposition of TiO_2. Since the presence of the CdS buffer layer proved to be deleterious, it was removed and just $Cu(In,Ga)Se_2$ was used as an absorber. The current-voltage behavior of $Cu(In,Ga)Se_2$ with and without protection by TiO_2 (TiO_2/ $Cu(In,Ga)Se_2$) is shown in Figure 5.1(c). It can be seen that bare $Cu(In,Ga)Se_2$ still shows disadvantages as photocathode in acidic media (high dark current, no photoactivity and high over potential) but after deposition of TiO_2 at the top, the sample proves to be sufficiently protected from corrosion. The current-voltage behavior shows no dark current, and the saturation photocurrent density reaches high values of 25 $mAcm^{-2}$ while the overpotential is considerably reduced down to 200 mV. The reason why still a relatively high overpotential is observed is attributed to the low conductivity of TiO_2. In the next section, it will be shown that the conductivity of the TiO_2 layer can be successfully improved by Pt doping.

5.1.2 Effect of the TiO_2 deposition temperature on the device performance

The deposition temperature of TiO_2 is a crucial parameter for optimization of the performance of the photocathode. To find out the optimum deposition temperature (T_d), the temperature control of the sample holder at the ILGAR set-up was adjusted to a sequence of different temperatures. Then the titanium precursor 0.01 M was sprayed (nitrogen flow: 30 LPM) on an FTO substrate and heated to a predefined temperature. Grazing-incidence XRD (GI-XRD) results, obtained after deposition, are shown in Figure 5.2. The black, red, green and blue curves correspond to 250°C, 350°C, 400°C and 450°C deposition temperature, respectively. Because of different instrumental requirements, GI-XRD measurements were carried out for TiO_2 layers deposited on FTO, while SPV and PEC measurements were performed for TiO_2 layers deposited on $Cu(In, Ga)Se_2$ substrates.

Figure 5.2 shows that, layers deposited at 250°C and 350°C are amorphous. All the observed peaks correspond to the FTO substrates indicated by dashed lines. By increasing the temperature of the sample holder to 400°C (green curve), the amorphous TiO_2 layer becomes crystalline. The peak positions are in accordance with the anatase phase. For deposition at 400°C, the FTO peaks still are visible at the angels 25.59°, 33.66°, 51.76°, 61.76° and 65.73°. By increasing the temperature to 450°C, the crystallinity of the layer increases and most of the FTO peaks are not visible anymore. This observation is attributed to the larger TiO_2 thickness caused by the deposition at an increased temperature.

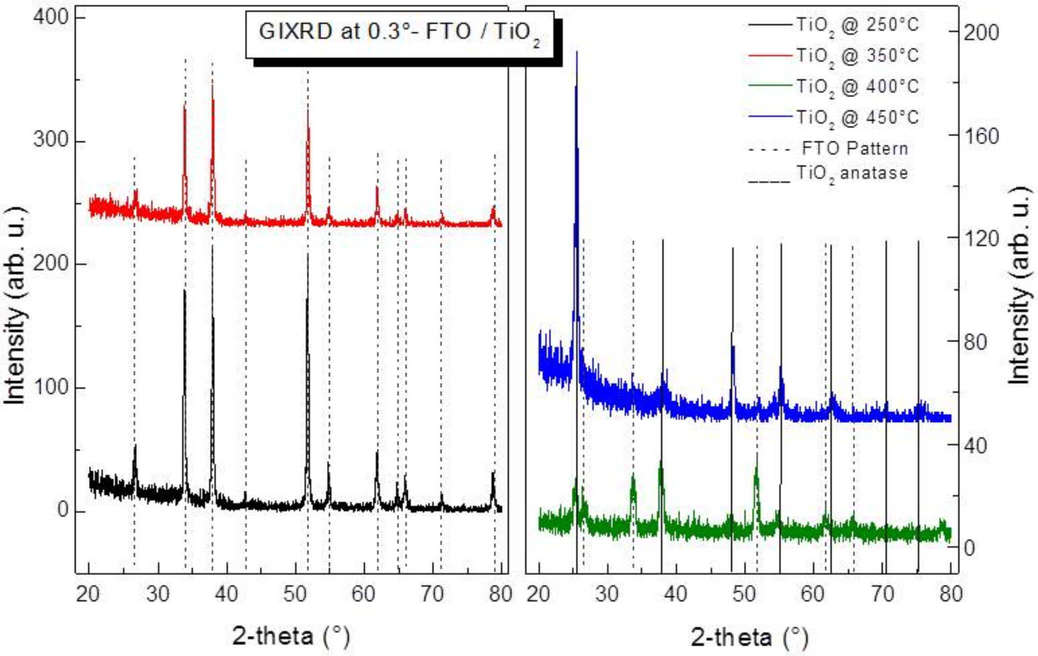

Figure 5.2: Grazing incidence X-ray diffraction (GIXRD) at 0.3° angle of incidence of ILGAR TiO_2 deposited on FTO at different deposition temperatures: 250°C (black curve), 350°C (red curve), 400°C (green curve) and 450°C (blue curve).

Figure 5.3 shows the effect of the deposition temperature on the SPV-determined mobility edge and on the formation of defect states near the band gap of the $\mathrm{TiO_2/Cu(In,Ga)Se_2}$ composite. The left image in Figure 5.3 (a) shows the normalized SPV amplitude versus photon energy for bare $\mathrm{Cu(In,Ga)Se_2}$ (purple curve), and for $\mathrm{TiO_2/Cu(In,Ga)Se_2}$ deposited at 250°C (black curve), 350°C (red curve), 400°C (green curve) and 450°C (blue curve). SPV results prove that bare CIGSe has two absorption edges, one with an onset between 0.8-0.99 eV and another one at 1.6 eV. With heating of the $\mathrm{Cu(In,Ga)Se_2}$ substrate to increasing temperatures, this second absorption edge becomes less and less visible.

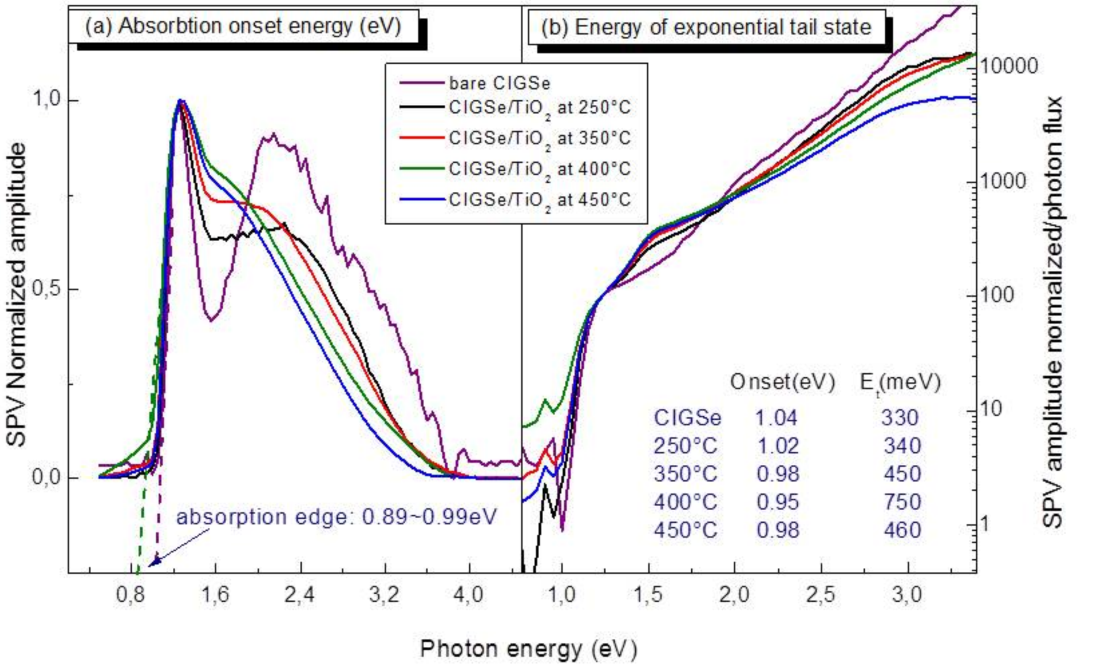

Figure 5.3: Surface photovoltage measurements: (a) Normalized SPV amplitude and (b) normalized SPV divided by photon flux for $\mathrm{TiO_2 : CIGSe}$ samples prepared at different deposition temperatures: bare CIGSe (purple curve), 250°C (black curve), 350°C (red curve), 400°C (green curve) and 450°C (blue curve).

The strong variation of the onset energies for the lower band edge (between 0.8 and about 1 eV) is attributed to the increasing incorporation of carbon and nitrogen into the heterojunction and diffusion of copper atoms. It is well known that disordering processes in materials can lead to defect states in the band gap close to the band edge and result in an exponential drop in the SPV signal towards lower photon energies [182]. The tail state energy,E_t, is a characteristic quantity of the degree of disorder in a semiconductor and describes the defect states below the band gap which participate in charge separation [180]. In order to obtain the energy parameter of the exponential tail states (E_t), the normalized SPV amplitude is divided by the photon flux and fitted by an exponential function in the region below the band gap. Figure 5.3(b) shows E_t values for bare CIGSe (330 meV) and for $\mathrm{TiO_2/Cu(In,Ga)Se_2}$ at 250°C, 350°C, 400°C and 450°C (340, 450, 750 and 460 meV, respectively).

PEC measurements were carried out for samples prepared at different T_d to determine the dependence of the performance of the composite photocathodes on T_d (Figure 5.4). On the left hand side (Figure 5.4(a)) the current-voltage behavior of $\mathrm{TiO_2/Cu(In,Ga)Se_2}$ for T_d: 250°C (black curve) and 350 °C (red curve) is shown and on the right hand side

(Figure 5.4(b)) the corresponding current-voltage behavior of $TiO_2/Cu(In, Ga)Se_2$ for T_d: 400°C (green curve) and 350°C (blue curve) is depicted. The dashed lines show the activity of the composite photocathode in the dark and the solid lines show the performance under illumination. For samples with an amorphous TiO_2 layer at the top (prepared at 250°C and 350°C), high dark currents, low photoactivity and high onset potentials were observed. Moreover, sample degradation proceeds fast.

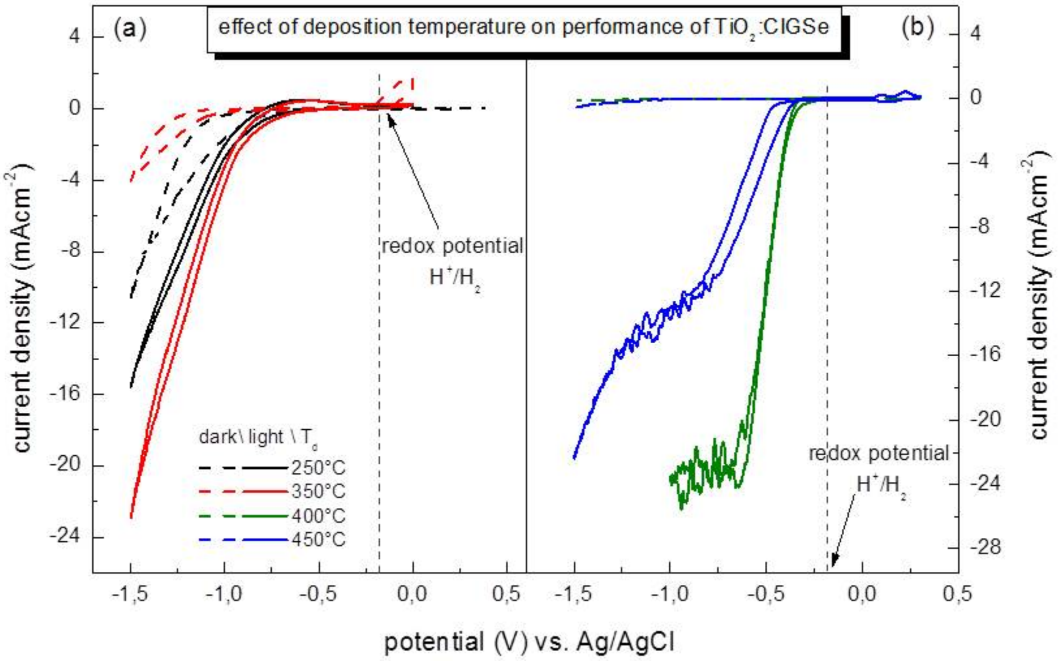

Figure 5.4: Effect of deposition temperature on the current-voltage behavior of the $TiO_2/Cu(In, Ga)Se_2$ photocathode: TiO_2 sprayed at (a) 250°C (blue curve), 350°C (red curve) and (b) 400°C (green curve), 450°C (orange curve). Electrolyte: 0.5 M H_2SO_4, pH0.3. Photoelectrodes were measured under near AM1.5 (100 mW/cm^2) conditions, with Pt as counter electrode and Ag/AgCl as reference electrode.

For samples with crystalline TiO_2 layers, it is observed that the dark current density is limited. For a deposition temperature of T_d= 400°C the resulting sample shows the lowest overpotential of about 200 mV. At 600 mV a saturation photocurrent density of 24 $mAcm^{-2}$ is reached. A further increase of the deposition temperature to 450°C, however, results in a decrease of the photoactivity of the junctions, indicating thereby an optimum deposition temperature near 400°C.

A potential physical property, to be related to the observed decrease in performance, is the decreased conductivity of the TiO_2 layer when the deposition temperature exceeds 400°C. This conclusion will be discussed in connection with so-called four-probe resistivity measurements to be discussed below (see Figure 5.7).

5.1.3 The Pt-doped TiO_2 layer: variation of the doping density

Although TiO_2 is a stable oxide in aqueous electrolytes it has the drawback of poor conductivity. As mentioned in section 3.1.2, one of the approaches to improve the conductivity in the TiO_2 layer is elemental doping, using transition metals [183]. Here, Pt was chosen as dopant metal due to its high activity for HER and also due to its stability in aqueous solutions. In order to identify the optimum value for the doping density, various concentrations of the platinum molecular precursor in the ILGAR process, from 2

vol.% up to 10 vol.% were tested. The resulting photocurrent densities for the Pt-doped $TiO_2 : Cu(In, Ga)Se_2$ samples as a function of the applied potential is shown in Figure 5.5. Solid curves indicate the results obtained under illumination of 100 $mWcm^{-2}$ (AM1.5), dashed curves show the activity of the samples in the dark. The photocathode was illuminated from the front side through the electrolyte (H_2SO_4 0.5 M pH0.3).
The solid black curve shows the performance of the undoped TiO_2 on CIGSe with an onset potential for hydrogen evolution of -200 mV (corresponding to an overpotential of 200 mV). Results for doped samples prove that, in general, by addition of the Pt-precursor to the solution, the onset potential shifts from negative values towards more positive values, i.e. the overpotential is reduced. This shift of the onset potential can be attributed to both Pt-doping, which increases the conductivity, and Pt nanoparticles (NPs) inclusions, which enhances the electrocatalytic activity of the TiO_2 layer.

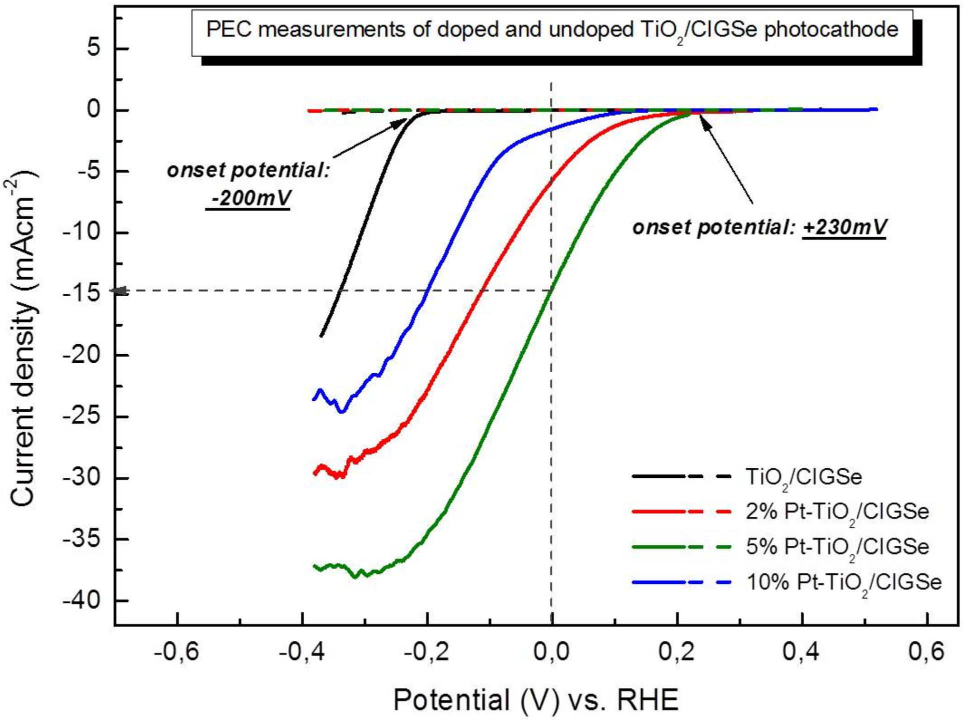

Figure 5.5: (a) Current-voltage behavior of undoped $TiO_2 : Cu(In, Ga)Se_2$ (black curve) and Pt-implemented $TiO_2 : Cu(In, Ga)Se_2$ devices. The best current-voltage behavior shows an anodically shifted onset potential at +230 mV (green curve); Electrolyte: 0.5 M H_2SO_4, pH0.3. Photoelectrodes were measured under near AM1.5 (100 mW/cm^2) conditions.

The red, green and blue solid curves are showing the performance of samples with 2, 5 and 10% Pt doping density, respectively. The vertical dashed line serves as a mark for $E_{RHE} \approx 0$ V and emphasizes the potential gain in hydrogen evolution achieved by the $Pt : TiO_2/Cu(In, Ga)Se_2$ composite photoelectrodes in comparison to the undoped device. By increasing the Pt density from 2 to 5 vol.%, the performance of the photocathode is improved and improves from 30 $mAcm^{-2}$ saturation photocurrent density to 37 $mAcm^{-2}$ with an onset potential of +230 mV. Further increase of the doping density to 10 vol.%, however, decreases the performance dramatically: the saturation photocurrent density decreases to 25 $mAcm^{-2}$ and the onset potential shifts to +100 mV. An optimum photoelectrocatalytic device performance is therefore achieved for 5 vol.% Pt: a saturation photocurrent density of 37 $mAcm^{-2}$corresponds, in fact, to values obtained to reported best chalcopyrite solar cells [184]. Furthermore, 15 $\mathtt{mAcm}^{-2}$ photocurrent density obtained at the redox the potential already exceed industrial minimum requirements of 10 $\mathtt{mAcm}^{-2}$ by 50%. For potentials more negative than about -0.4 V RHE , the device performance of the photocathode is only limited by the excess minority charge carriers (electrons) generated by the external white light source ($\approx$ 38 $\mathtt{mAcm}^{-2}$; simulating AM1.5 conditions). Several measurements including UV-VIS, SPV, SEM/TEM and four probe measurements were performed to clarify the role of the Pt for the efficiency of the photoelectrode. The results are reported in the following sections.

5.1.3.1 The twofold functionality of Pt as dopant and catalyst

In this section, by comparative analysis of TEM, XPS (The SEM, TEM and XPS measurements were done by Dr. M. Lublow, Dr. A. Fischer from Uni-Freiburg and A. Steigert from HZB, respectively)and XRD results, the twofold functionality of Pt as dopant and catalyst is demonstrated [183]. The Pt doping concentration in the $\mathtt{TiO_2}$ thin films was modified by applying various concentrations of the platinum molecular precursor in the ILGAR process, from 2 vol.% up to 10 vol.%. Corresponding TEM images for 2%, 5% and 10% Pt doping are shown in Figure 5.6 (a), (b) and (c), respectively. For low platinum precursor concentrations of 2 vol.%, no Pt-cluster formation is detected by TEM, i.e. Pt-atoms are most likely incorporated into the $\mathtt{TiO_2}$ host-lattice either on $\mathtt{Ti}^{+4}$ cation sites or at interstitial sites. For 5 vol.%, aggregation of Pt nanoparticles (NPs) is observed in the $\mathtt{TiO_2}$ layer (Figure 5.6 (b)). For higher concentrations of 10 vol.%, the Pt NPs increase further in size and also aggregate directly at the $\mathtt{TiO_2}$-$\mathtt{Cu(In,Ga)Se_2}$ interface. Figure 5.6 also shows that the morphology of the $\mathtt{TiO_2}$ layer changes by increasing the Pt concentration from a flake-like morphology (2% doping) to big crystals (10% doping). The conductivity of the $\mathtt{TiO_2}$ layer doped by Pt, was determined by four probe measurements. The results are shown in Figure 5.7. The blue line shows the resistivity of the Pt doped $\mathtt{TiO_2}$ layer after deposition on glass. The green line shows the resistivity of the layer after deposition on $\mathtt{Cu(In,Ga)Se_2}$. The red line shows the thickness of the corresponding layers (Pt:$\mathtt{TiO_2}$/glass) measured by a Dektak step profilometer and shows the reducing trend for thickness upon increase of the doping level. The thickest layer shows a thickness of 350 nm for undoped $\mathtt{TiO_2}$. The thickness of Pt-doped $\mathtt{TiO_2}$ layers, prepared from solutions containing 2%, 5% and 10%, is 180 nm, 115 nm and 50 nm, respectively. These results are in good agreement with UV-VIS measurements (section 5.1.3.2). According to the conductivity results in Figure 5.7, the conductivity increases with increasing Pt-concentration from 2% to 5% due to incorporation of Pt-atoms in the layer and decreases upon further increase of the concentration to 10% due to formation of Pt-clusters (TEM image 5.6(c)).

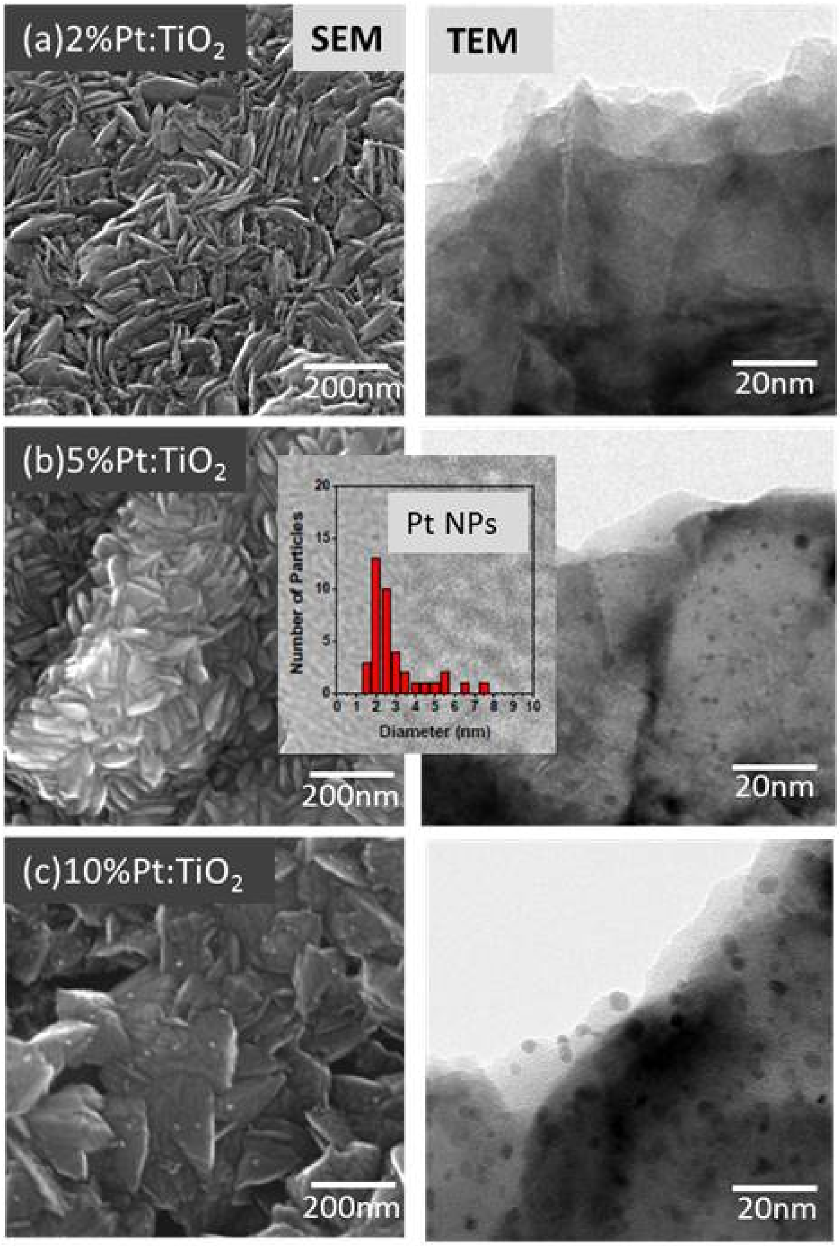
(a)2%Pt:TiO2
SEM
TEM
200nm
20nm
(b)5%Pt:TiO2
Pt NPs
Number of Particles
0
5
10
15
20
0 1 2 3 4 5 6 7 8 9 10
Diameter (nm)
200nm
20nm
(c)10%Pt:TiO2
200nm
20nm

Figure 5.6: Surface morphology (SEM, left) and Pt-distribution (TEM, right) of TiO_2 thin films on CIGSe supports upon increasing Pt concentrations. Characterization by SEM clearly shows an increase of the anatase crystallite size for incremented Pt concentrations. For 5 and 10 vol.%, agglomeration of Pt to nano-clusters is visible in the corresponding TEM images [183].

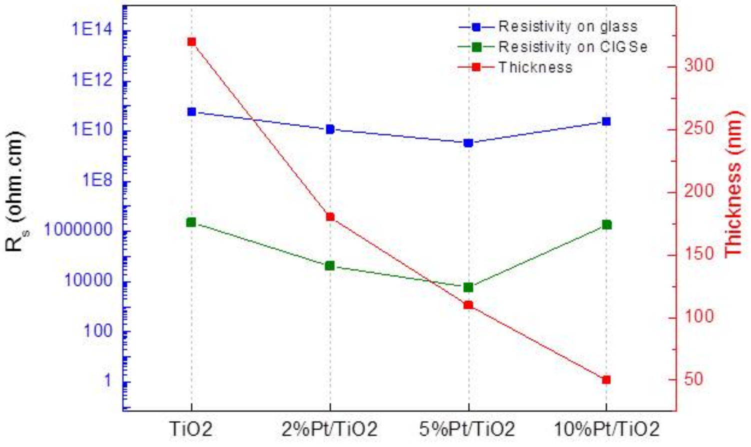

Figure 5.7: Resistivity and thickness of undoped and Pt-doped TiO_2.

GI-XRD and XPS spectroscopy results are discussed in the following to identify the oxidation state of Pt inside the TiO_2 layer. The grown TiO_2 thin films on the CIGSe are characterized by measurements carried out at a grazing X-ray angle of incidence of 0.3°. Measurements were done for three samples as shown in Figure 5.8: the black curve shows the XRD result obtained for undoped TiO_2 on CIGSe, the red and green curves show the corresponding results for 2 and 5 vol.% Pt doping. The results suggest that TiO_2 deposited at 400°C is characterized by an anatase phase (Figure 5.8). The CIGSe pattern is not visible for the undoped TiO_2 layer since the layer thickness is larger in comparison to doped TiO_2, as proven by Dektak step profilometry. The increasing Pt(200) signal at 46.5° for the doped samples indicates the incremented incorporation of metallic Pt in the TiO_2 layer.

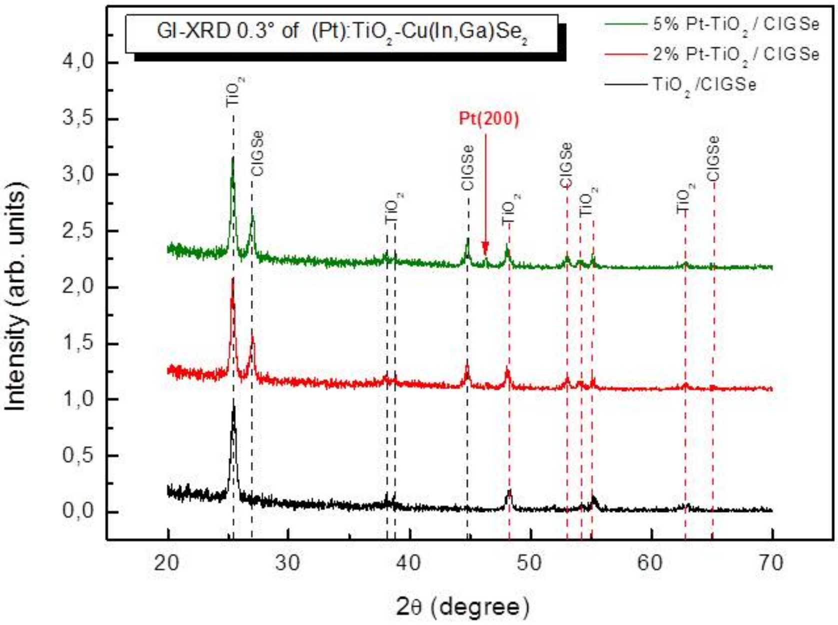

Figure 5.8: (a) Grazing incidence X-ray diffraction (GIXRD) at 0.3° angle of incidence of undoped ILGAR TiO_2 paste (black curve), 2 vol.% Pt doped TiO_2 (red curve) and 5 vol.% Pt doped TiO_2 (green curve). All films were prepared on CIGSe substrates.

X-ray photoelecron spectroscopy (XPS) of the Pt 4f core-level signal was carried out for a Pt:TiO_2 film prepared from solutions with 5 vol.% Pt-precursor concentration (Figure 5.9). According to XPS analysis, the actual Pt concentration is only about 0.1 atom%. Due to the high surface sensitivity of the method, this result is valid for an about 10 nm thin surface region. The value of 0.1 atom%, on the other hand, is close to the detection limit of this technique. The Pt $4f_{7/2}$ and Pt $4f_{5/2}$ signals show a pronounced asymmetric broadening most likely due to the contributions of Pt in an oxidation state of ”+2” and ”+4”, denoted in the figures as Pt(II) and Pt(IV), respectively. The signal Pt(0) at a binding energy near 71 eV is caused by metallic platinum, i.e., Pt-NPs.
According to recent results reported in the literature, Pt^{4+} and Pt^{2+} ions can occupy either Ti^{4+} sites or interstitial sites in rutile or in the anatase lattice [185]. As a result of similar ionic radii of Pt^{2+} (R_{ion} = 0.80 Å) and Pt^{4+} (R_{ion} = 0.63 Å) ions in the sixfold coordination geometry of anatase, TiO_2 (Ti^{4+} (R_{ion} = 0.61 Å) [25] either Pt^{2+} or Pt^{4+} ions (with electron configurations of Pt^{2+} [Xe] $4f^{14}$ $5d^8$ and Pt^{4+} [Xe] $4f^{14}$ $5d^6$) can partially replace Ti^{4+} ions leading to an extra n-type doping of the TiO_2 anatase in the bulk. The relative contributions of Pt(0), Pt(II), and Pt(IV) in Figure 5.9 indicate predominantly a Pt-dopant oxidation state of ”+2” rather than ”+4”. Three contributions to the envelope curve were identified and labeled as Pt(0), i.e. metallic Pt, Pt(II) and Pt(IV). The oxidation states (II) and (IV) are attributed to PtO, $Pt(OH)_2$ and PtO_2, respectively. The low signal-to-noise ratio impedes accurate analysis with respect to both the background signal and the identified components.

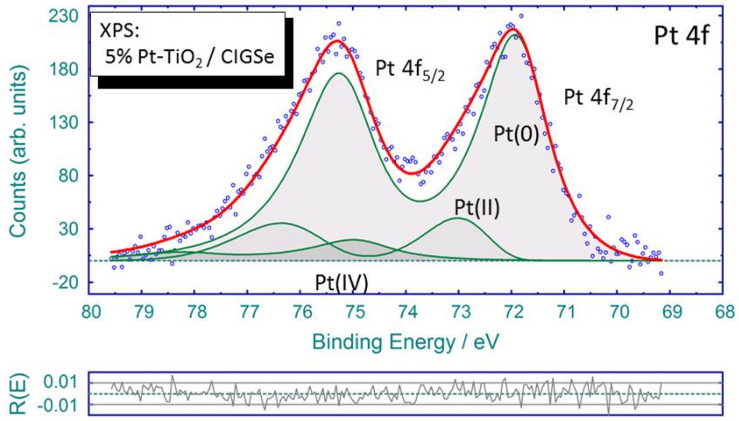

Figure 5.9: X-ray photoelectron spectroscopy of the Pt4 core level for the 5 vol. % Pt-TiO_2 film [183].

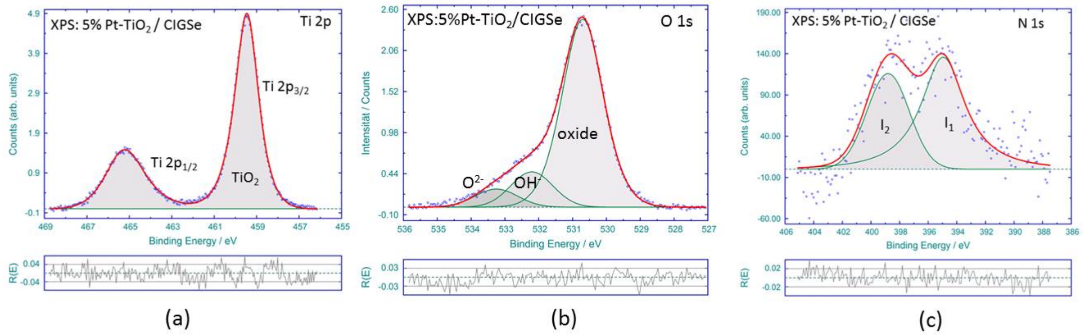

(a) (b) (c)

Figure 5.10: X-ray photoelectron spectroscopy of the Ti 2p (a), O 1s (b) and N 1s (c) signals measured for 5% Pt-doped TiO_2 on CIGSe [183].

Figure (5.10(a)) shows the XPS analysis of the Ti 2p signal for the sample with 5% Pt doping. For analysis of the data, only one doublet peak was applied. The small variation of the residuum between 459 eV and 462 eV suggests the presence of a further component. However, no convergence was achieved assuming a second Ti 2p related doublet structure. XPS analysis of the O 1s signal measured for 5% Pt-doped TiO_2 on CIGSe is shown in Figure (5.10(b)). Two sub-structures were identified to be attributed to oxygen in TiO_2 (near 530.7 eV) and hydroxyl groups (near 532.5 eV). XPS analysis of the N 1s signal measured for 5% Pt-doped TiO_2 on CIGSe is shown in Figure (5.10(c)). The core-level signal I_1 is assigned to substitutional nitrogen at an oxygen site, the signal I_2 may either be related to interstitial N or NH_x.

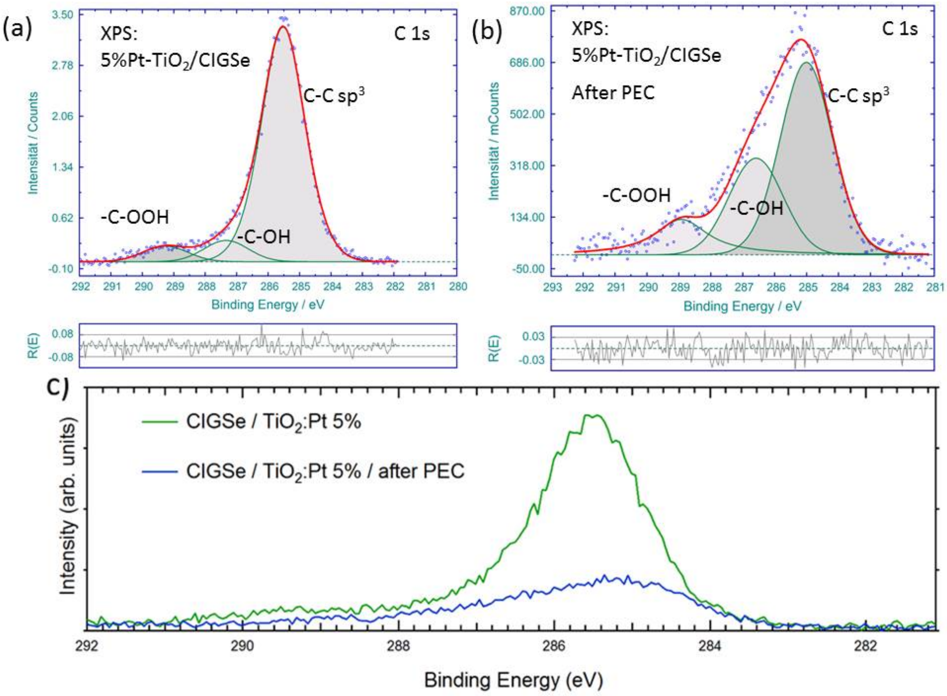

Figure 5.11: XPS analysis of the C 1s signal measured for 5% Pt-doped TiO_2 on CIGSe. (a) before electrochemistry, (b) after electrochemistry, (c) comparison of the C 1s signals in (a) and (b)[183].

Figure 5.11 shows the respective components for sp^3 C-C bonds, C-OH and C-OOH. Due to the broadening of the sp^3 peaks, it is not possible to exclude sp^2 carbon. These components are detected before as well as after photoelectrochemical evolution of hydrogen. The much lower intensity of the signal after operation, however, suggests that carbon is mainly confined to the surface, i.e. carbon species are adsorbed from the environment rather than incorporated in the oxide film.

5.1.3.2 Correlation of optical behavior with doping density

The optical properties of the doped TiO_2 layers, deposited on glass, were investigated by UV-VIS measurements. Figure 5.12 shows the transmission (a) and reflectance spectrum (b) and the absorption coefficient (c) which was calculated according to the Beer-Lambert Law [110]. In these figures, the black curve shows the spectrum for undoped TiO_2 and the red, green and blue curves show the spectra for the samples with 2%, 5% and 10 vol.% doping density. The transmission and reflectance spectra reveal that the optical properties of the TiO_2 film are sensitively influenced by gas phase proportion of the Pt precursor and demonstrate the nonlinear change in light absorption upon incrementing Pt-concentrations. The measurements show that the transparency of doped samples is higher than of undoped TiO_2 (black curve) and is increased by incrementing Pt-concentrations from 2 to 5 vol.%. The transparency decreases, however, for the photocathode device with the highest Pt concentration in the TiO_2 layer (10 vol.% Pt precursor).

Comparison of the reflectance behavior demonstrates that the reflection of the doped layers is higher than for undoped TiO_2 [183]. The reflection decreases with incrementing Pt-concentrations. The sample with 2 vol.% Pt doping has the highest reflection. The lowest reflection is observed for the 10 vol.% Pt doping concentration. This change in the optical behavior is also visible to the naked eye: a color change is observed upon increase of the doping level which is attributed to decreasing film thickness and formation of Pt-clusters. Samples prepared from solutions with 2 vol.% Pt-precursor concentrations appear yellowish while samples with 10 vol.% appear more brownish.

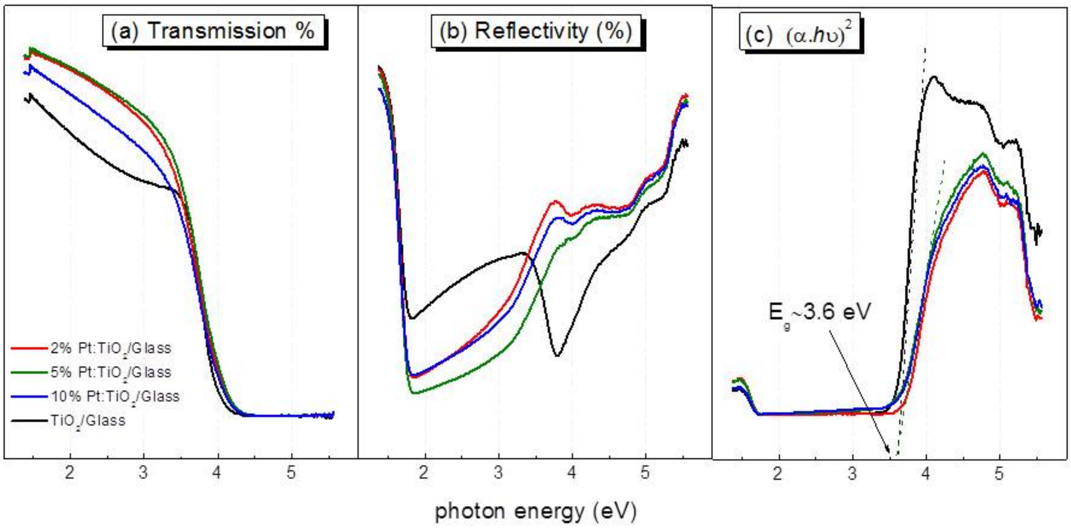

Figure 5.12: UV-VIS transmission (a) and reflection (b) of undoped and Pt-doped TiO_2/CIGSe(c) Determination of the optical band gap of undoped and Pt-doped TiO_2/CIGSe.

The increased density and average size of the Pt-NPs limits the magnitude of light that reaches the chalcopyrite absorber (Figure5.5). Furthermore, increased electron-hole recombination at the TiO_2/Pt-NP interface can lower the achievable saturation photocurrent density. Consequently, saturation photocurrent densities are limited to about 25 $mAcm^{-2}$ (blue curve; Figure 5.5). The photocathode device with the lowest Pt concentration in the TiO_2 layer (red curve; Figure 5.5), in turn, proves higher saturation photocurrent densities. But they remain still below those of the most efficient photocathode device with TiO_2 films grown in 5 vol.% Pt-precursor gas phase concentration.
The absorption coefficient, α, of the samples was determined according to $1 = \alpha + R + T$ where R and T represent reflectance and transmission of the samples, respectively. The calculated spectra, $(\alpha - h\nu)^2$, were subsequently extrapolated by straight lines (Figure 5.12(c)). Here, $h\nu$ represents the photon energy. According to the results indicated by the inset, an optical band gap of about 3.6 eV was determined for all samples. It is noteworthy that this band gap is typically detected for TiO_2 prepared by spray pyrolysis.

5.1.3.3 Dependence of the energy of the tail states on the doping density

SPV measurements were used for investigation of the charge separation mechanism in the TiO_2 layers. In this chapter, results for the mobility edge of different TiO_2 layers and charge separation mechanisms across the TiO_2/FTO junction are presented. Charge separation across the interface was measured by modulated SPV (explained in detail in 4.2.4.3) in the fixed parallel plate capacitor configuration and as a function of the deposition method. Three different samples are compared in Figure 5.13; commercial TiO_2 paste (blue curve) prepared by screen printing, undoped TiO_2 prepared by ILGAR (green curve) and Pt doped TiO_2 also prepared by the ILGAR process (red curve) after deposition on fluorinated tin oxide (FTO). Figure 5.13(a) shows the normalized SPV amplitude of these three samples. According to the results, the onset of the SPV absorption (E_{abs}) (mobility edge) for the commercial TiO_2 is 3.2 eV, i.e. it is close to the optical band gap of TiO_2. This value is shifted to 1.05 eV in the case of TiO_2 samples prepared by the ILGAR process. This position of the absorption edge is due to embedding of carbon and nitrogen atoms inside the TiO_2 structure during the deposition process. According to Figure 5.13(a), Pt-doping, in fact, gives rise to an additional defect band centered at 3.2 eV and pointing thereby to an increased density of donor-like states near the conduction band. These defect bands contribute to an increase in absorption and higher charge separation [183].

Figure 5.13(b-d) shows the X and Y signals for commercial TiO_2 paste (b), undoped TiO_2 (c) and Pt:TiO_2 (d) deposited on FTO. For all samples X signals were positive and Y signals were negative. This means that photo-generated electrons were separated preferentially towards the internal interface. The amplitude of both X and Y signals for commercial TiO_2 paste is higher than for ILGAR-grown TiO_2. Comparison of Figure 5.13(c) and (d) shows that Pt-doping resulted in a decrease of the amplitude of the X and Y signals. For all samples a common peak arises at 3.2 eV corresponding to the band gap of TiO_2. The absorption peak at 1.05 eV for samples prepared by ILGAR was also detected in the X and Y signals. New signals around 2.5 ev and 2.7 eV were observed in the defect region below the band gap of TiO_2 for Pt doped TiO_2 (Figure 5.13(d)) which are not detectable for the undoped TiO_2 sample.

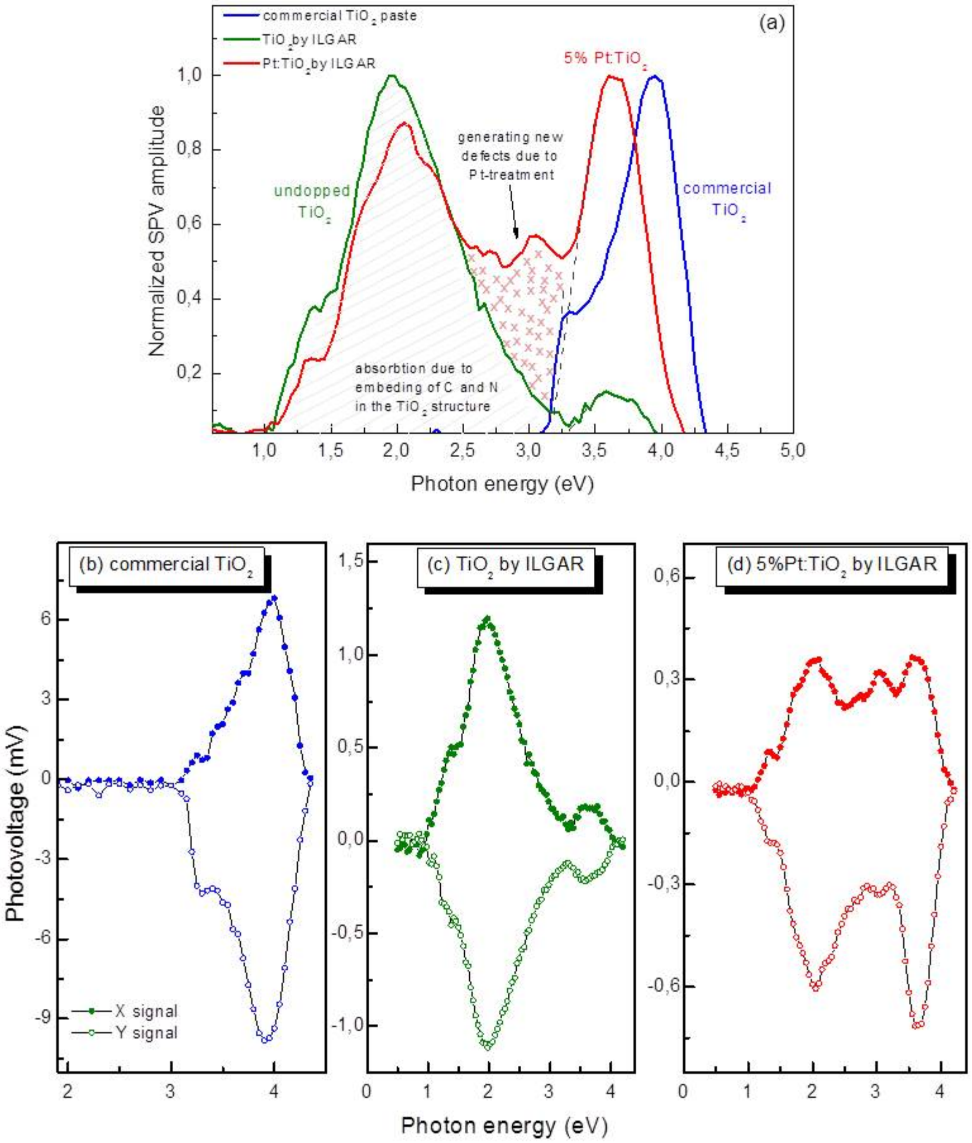

Figure 5.13: Surface photovoltage measurements (SPV): (a) Normalized SPV amplitude, in-phase (blue curves) and phase shifted by 90° signals (red curves) for commercial TiO_2 paste (b), undoped TiO_2 (c) and 5%Pt:doped TiO_2 (d) prepared by the ILGAR process.

5.1.3.4 IPCE - DEMS measurements

Quantum efficiencies characterize the performance of a photocathode in photon-to-charge carrier conversion efficiency. Figure 5.14 presents the corresponding IPCE data, measured at a constant potential of −0.4 V RHE, i.e. in the saturation photocurrent density region. Four different doping concentrations (0, 2, 5, and 10 vol.% Pt-precursors, respectively) are compared. Measurements were performed over a wide range of wavelengths (300-800 nm). The black curve shows the IPCE of undoped TiO_2 deposited on CIGSe. The IPCE data are below 8% over the visible light range. The red, green and blue curves belong to 2, 5, 10 vol.% Pt doping density, respectively. The IPCE results are in good agreement with the corresponding PEC performance of the photocathodes: the efficiency of the sample increases by incrementing of the Pt density from 2 to 5% and decreases by further doping to 10 vol.%. This finding implies better charge separation with Pt up to 5 vol.% and is also in good agreement with conductivity measurements (Figure 5.7).

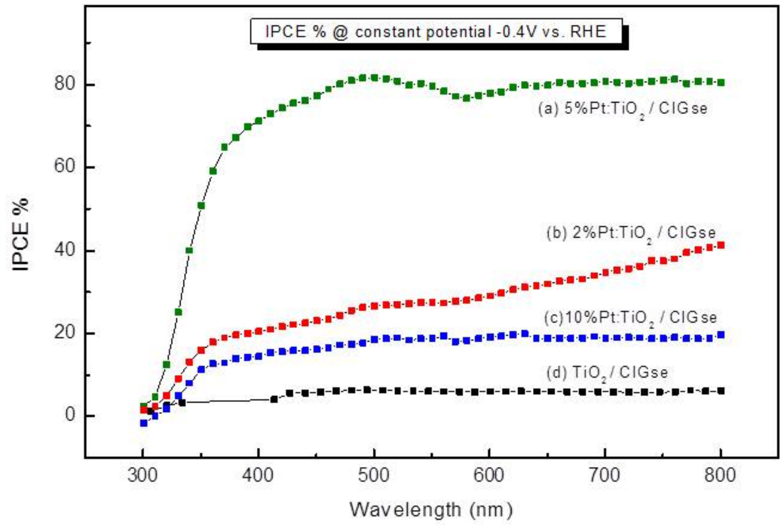

Figure 5.14: Incident-photon-to-charge-carrier conversion efficiency (IPCE) data of four different Pt-doped $TiO_2 - Cu(In, Ga)Se_2$ heterojunctions. (a) green squares: 5 vol.% Pt; (b) red squares: 2 vol.% Pt; (c) blue squares: 10 vol.% Pt compared with the undoped $TiO_2 - Cu(In, Ga)Se_2$ heterojunction photocathode (d) black squares. The IPCE data have been measured at -0.4 V vs. RHE. Electrolyte: 0.5 M H_2SO_4, pH0.3 [183].

The IPCE data of the most efficient photocathode device reveals an essentially high efficiency of ≈ 80% over the complete visible light range from 400 to 800 nm (green squares). The observed cut-off energies can be related to the optical band gap of ILGAR-TiO_2 (near 345 nm corresponding to 3.6 eV, respectively, $Cu(In, Ga)Se_2$ (≈ 1000 nm corresponding to ≈ 1.2 eV) [117,186].

In order to prove the evolution of hydrogen gas and to exclude formation of H_2Se, HER of the most efficient (5%)Pt-doped TiO_2 /$Cu(In, Ga)Se_2$ photocathode was followed by differential (photo-) electrochemical mass spectroscopy (DEMS) as shown in Figure 5.15. The onset for hydrogen evolution (blue solid line: mass signal of H_2 related to the left y-axis) of the photocathode occurs at a positive, anodic potential of about 110 mV versus the RHE reference electrode.

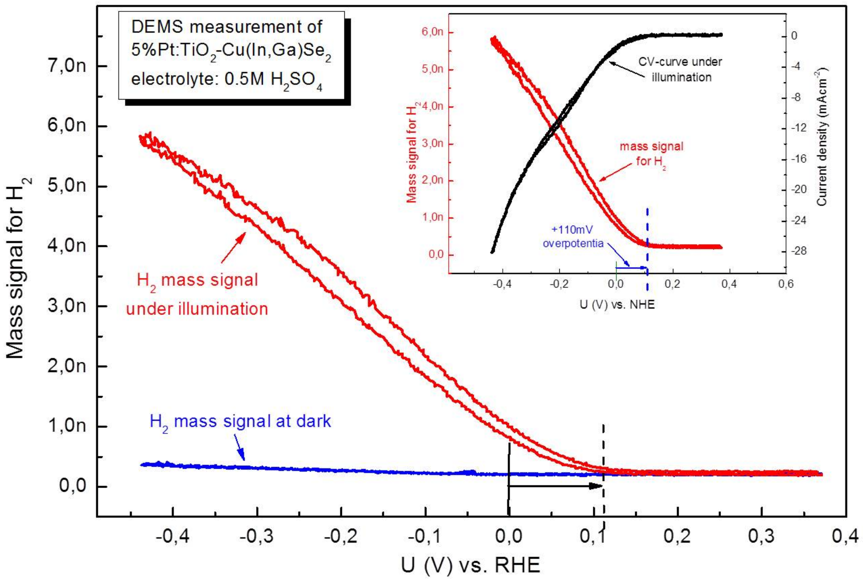

Figure 5.15: Hydrogen evolution behavior of the most efficient Pt-implemented TiO_2-$Cu(In,Ga)Se_2$ photocathode under illumination (red curve) and in the dark (blue curve) detected by differential photoelectrochemical mass spectroscopy (DEMS). The inset shows the hydrogen evolution with respect to CV curves under illumination. Electrolyte: 0.5 M H_2SO_4, pH0.3.

This onset potential is lower than the corresponding one shown in Figure 5.5 and is caused by the employed gas membrane of the DEMS setup. This membrane is in close contact to the sample, limiting thereby mass transport to the sample and causing an additional overpotential. The inset shows the hydrogen evolution mass signal (red curve) with respect to the CV curve under illumination (black curve). The slight increase of the H_2-mass signal in the dark is attributed to incomplete sealing of free parts of the molybdenum back contact to which electrical contacts were connected. In our custom-made setup, not all evolved H_2 gas can be directed to the spectrometer therefor the results of Figure 5.15 are qualitatively only and it is not possible to evaluate the amount of generated H_2.

5.1.3.5 pH dependent performance: CV and stability measurements

The photoelectrochemical behavior of the most efficient photocathode (5 vol% Pt-precursor solution) is shown in Figure 5.16 for aqueous electrolytes of pH 0.3 (green curves), pH7 (red curves) and pH14 (blue curves). Solid lines show the original data and dashed lines are IR corrected data, i.e. data corrected for uncompensated solution resistance, R, as determined by impedance spectroscopy. The corrected potentials are calculated by subtraction of the potential drop across the solution, IR, from the applied potential U according to: ($U_{new} = U_{measured} - IR$).

As shown in this Figure, at the redox potential, current densities of 14, 13 and 3 $mAcm^{-2}$ were measured for pH values of 0.3, 14 and 7, respectively. The current-voltage behavior of the sample in pH7 shows that the saturation photocurrent density is obtained at significantly higher potentials which has to be attributed to the low conductivity of the electrolyte at pH7. In comparison to the most efficient devices for photoassisted evolution of hydrogen published so far, planar Si-Pt and InP-Rh heterojunctions [187-188] with efficiencies of 9.6% and 14.5%, respectively, the TiO_2-$Cu(In,Ga)Se_2$ system shows higher saturation photocurrent densities but operates less active, i.e. the samples show lower photovoltages and, consequently, a negatively shifted onset. However, our CIGSe substrates are characterized by uniform doping while both the Si and InP absorbers were fabricated as homojunctions with a highly doped surface-near region, improving thereby considerably the achievable photovoltage.

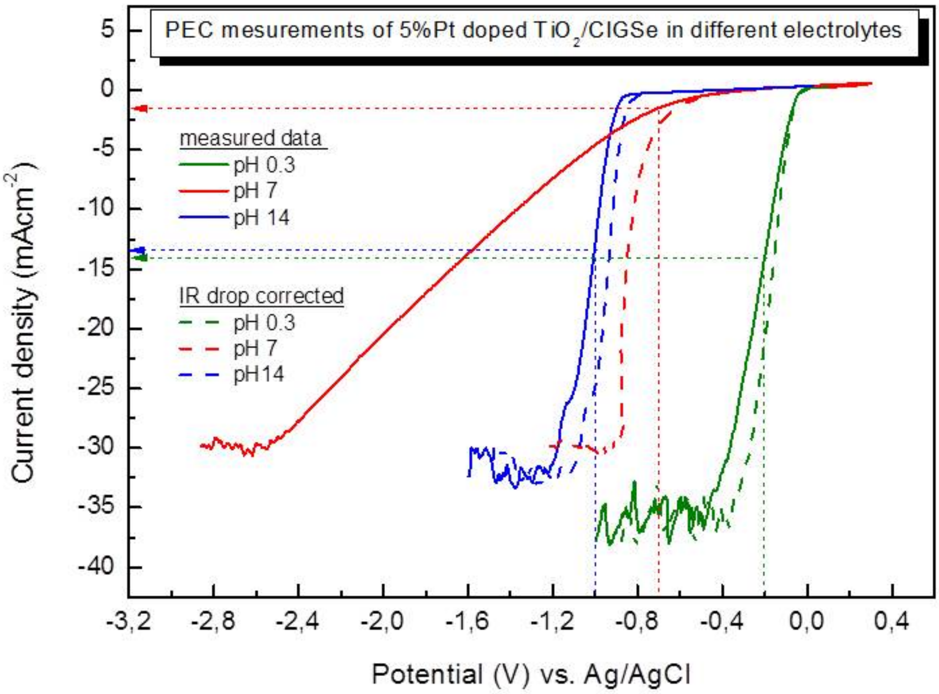

Figure 5.16: Current-voltage behavior of 5 vol.% Pt doped TiO_2-$Cu(In,Ga)Se_2$ composite photocathode devices in different electrolytes: H_2SO_4 0.5M pH 0.3 (green curve), KOH 1N pH 14 (blue curve) and KPi buffer phosphate solution pH7 (red curve). All measurements were carried out in a three-electrode mode vs. Ag/AgCl reference electrode.

To examine the long-term stability of the new composite devices, the cathodic photocurrent density has been measured at the thermodynamic reduction potential of hydrogen evolution, $E_0 = 0$ V RHE, in H_2SO_4 electrolyte pH0.3 (Figure 5.17). No degradation was observed within 25 h for the 5 vol.% $Pt : TiO_2/Cu(In, Ga)Se_2$ composite photocathodes. A cathodic photocurrent density of ≈ 9 $mAcm^{-2}$ was monitored over 25 h. The external light source was turned on under potential and turned off after 25h in order to prove the maintained photoactivity of the device and to exclude electrochemical degradation currents which can be typically observed also in the dark. In order to highlight this important stability, the corresponding turn-over-number (TON) of active surface sites of the photoelectrocatalyst surface was calculated. A total amount of charge of about 810 C cm^{-2} [$\approx 9\ mAcm^{-2} \times 25\,h \times 3600\,s$] is supplied by the photoelectrocatalytic sample. By assuming that each surface atom provides one active site ($\approx 10^{15}$ atoms cm^{-2}), a high TON of $\approx 2.5 \times 10^6$ is calculated for the produced solar hydrogen molecules per active site which corresponds to a Turn-over frequency (TOF) of about 690 hydrogen molecules per second and per active site [183].

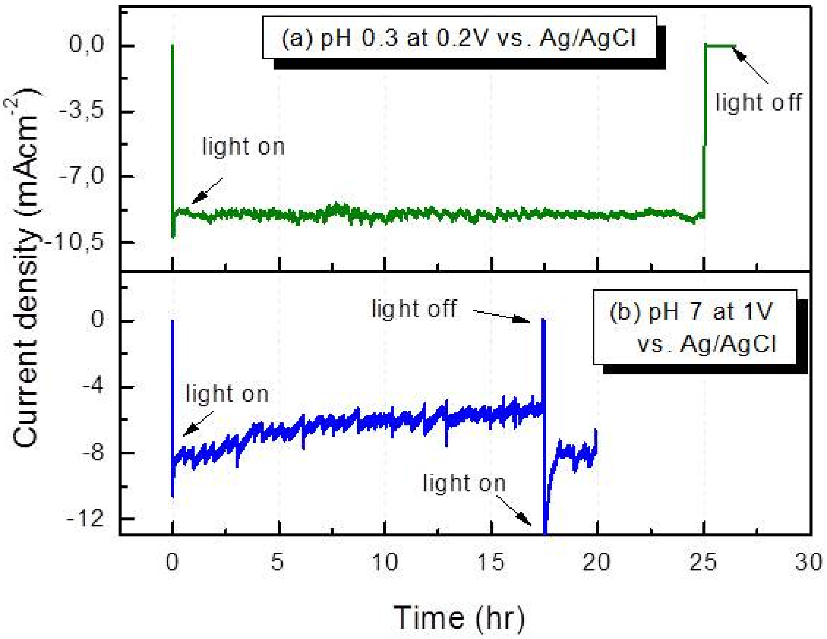

Figure 5.17: Photocurrent density time behavior over 25 (20) hours of the most efficient Pt-doped $TiO_2/Cu(In,Ga)Se_2$ heterojunction photocathode in electrolytes of pH0.3 (pH7). Photoelectrodes were measured under near AM1.5 (100 mW/cm^2) conditions at the hydrogen reduction potential 0 V vs. RHE. The spikes correspond to light on/light-off in order to assess the dark current density in a short time of several minutes.

In Figure 5.17(b), stability investigations for the sample in solutions of pH7 and pH0.3 are shown for 20 (25) h. The calculated STH is 2%. The long-term stability in neutral solutions with overpotential-free evolution of hydrogen proves the advantageous concept with promising implications for future industrial applications. After 24 hours the electrolyte was renewed and the sample was cleaned by rinsing in ultra-pure water. Subsequently the photocurrent density reached again values near 8 $mAcm^{-2}$. This finding suggests that active surface sites might have been contaminated during extended operation by the buffer solution. The stability at pH14 is limited about 2h.

5.1.4 Interface engineering by thin interfacial TiO_2 deposited by Atomic Layer Deposition (ALD)

SEM analysis of very low efficient samples revealed that Pt nanoparticles were forming at the interface and surface of the $TiO_2/Cu(In,Ga)Se_2$ junction. Figure 5.18 shows some of these SEM images. In (a) two big clusters formed on the surface of $Cu(In,Ga)Se_2$ and TiO_2. EDX mapping (b) proved that these particles are composed of Pt. Also in (c) and (d), the cross section and a top view of one of these samples is depicted and shows that a layer, composed of Pt nanoparticles, was formed at the interface of TiO_2 and $Cu(In,Ga)Se_2$.

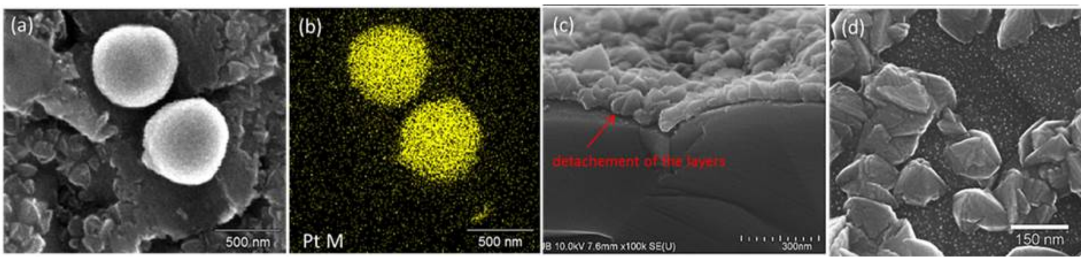
(a)
500 nm
(b)
Pt M
500 nm
(c)
detachement of the layers
10.0kV 7.6mm x100k SE(U)
300nm
(d)
150 nm

Figure 5.18: (a) and (b) SEM / EDX image of a low efficient sample, with formation of Pt clusters on the surface of a $Cu(In,Ga)Se_2$, (c) SEM image of cross section of the sample, (d) the top view SEM image of the sample shows formation of an interface layer with Pt nanoparticles.

The formation of a suitable metal-semiconductor junction is critical for the performance of the electrodes. As described in section (2.4), depending on the work function of the semiconductor and the metal, two types of barriers can be observed: the Schottky barrier and the ohmic barrier. The assumed band bending for a p-type semiconductor is proposed and shown in Figure 5.19 (a/b). According to UPS measurements, the electron affinity and work function of $Cu(In,Ga)Se_2$ are 3.8 eV and 4.82 eV, respectively. The work function of Pt depends on the size of the nanoparticle and is between 5.3 and 5.7 eV. If Pt comes in direct contact with $Cu(In,Ga)Se_2$ formation of an ohmic contact is assumed (Figure 5.18(b)). In this case, $Cu(In,Ga)Se_2$ is characterized by flat-band conditions or slightly upward band bending which prohibits separation of photogenerated carriers. Therefore no light-induced charge transfer occurs and the performance of the sample is low.

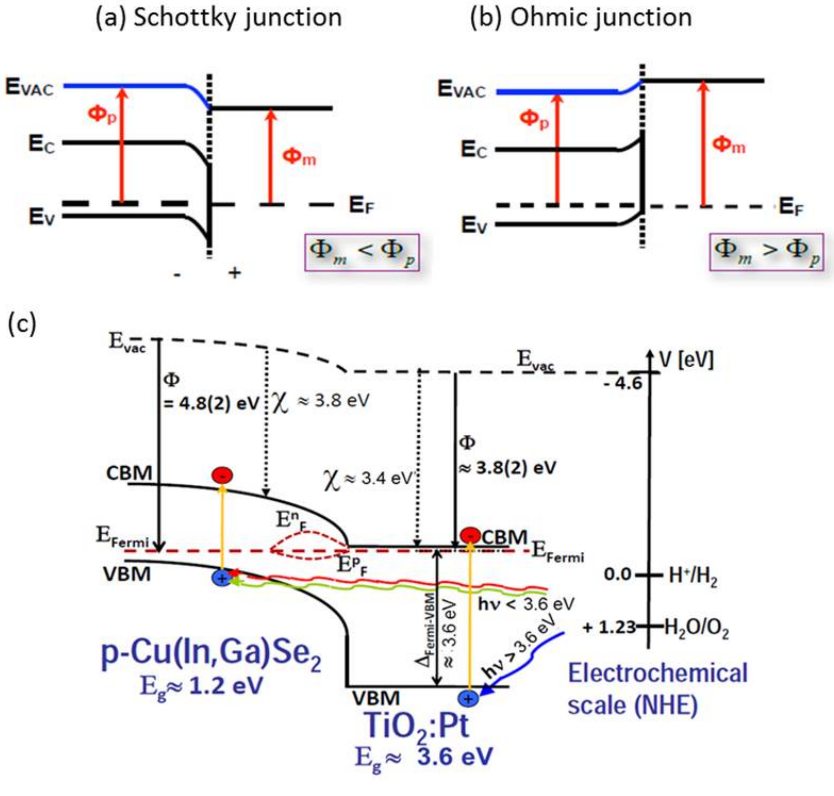
(a) Schottky junction
(b) Ohmic junction
EVAC
Φp
Φm
EC
EV
EF
Φm < Φp
Φm > Φp
-
+
(c)
Evac
Φ = 4.8(2) eV
χ ≈ 3.8 eV
χ ≈ 3.4 eV
Φ ≈ 3.8(2) eV
Evac
-4.6
V [eV]
CBM
EFermi
VBM
EnF
EpF
CBM
EFermi
0.0
H+/H2
+1.23
H2O/O2
hν < 3.6 eV
hν > 3.6 eV
ΔFermi-VBM ≈ 3.6 eV
p-Cu(In,Ga)Se2
Eg ≈ 1.2 eV
VBM
TiO2:Pt
Eg ≈ 3.6 eV
Electrochemical scale (NHE)

Figure 5.19: Band alignment of a p-semiconductor with a metal for different work function relations (a) $\Phi_m < \Phi_p$, (b) $\Phi_m > \Phi_p$ and (c) Proposed band alignment of the 5%Pt-doped $TiO_2 - Cu(In,Ga)Se_2$ [183].

In order to derive an energetic scheme for the TiO_2/ $Cu(In,Ga)Se_2$ junction, work function, Φ, energetic distance, ΔFermi-VBM, between valence band maximum (VBM) and Fermi energy, E_{Fermi}, in $Pt:TiO_2$ have been measured by means of UV-light excited photoelectron spectroscopy (UPS). The derived energetic position of the TiO_2 conduction band minimum (CBM) of ~ 3.4(2) eV, i.e. the electron affinity,χ, is negative with respect to the thermodynamic potential for proton reduction. A splitting of the quasi-Fermi levels of the minority charge carriers, $E_F^{n,p}$, occurs at the heterojunction under illumination and results in a net photovoltage. The proposed band alignment of the most efficient Pt-doped $TiO_2-Cu(In,Ga)Se_2$ composite photocathode is depicted in Figure 5.19(c) together with the electrochemical position of both the hydrogen reduction potential $\mu_e^{H^+/H_2}$, and the water oxidation potential, $\mu_e^{H_2O/O_2}$, on the right hand side [117,185-186].

In order to minimize the recombination rate at the interface of chalcopyrite the ($Cu(In,Ga)Se_2$) and TiO_2, and also to avoid the formation of semiconductor-metal (Pt) junctions, a thin layer (10 nm) of amorphous TiO_2 was deposited by atomic layer deposition (ALD) on the $Cu(In,Ga)Se_2$ surface. Subsequently, Pt doped TiO_2 was deposited by ILGAR. Figure 5.20 shows the comparison of the respective current-voltage behavior of the samples without Pt doping (black curve), 2%, 5% and 10% Pt:TiO_2/$Cu(In,Ga)Se_2$ (in red, green and blue curves) and the sample with an ALD TiO_2 interlayer and 5%Pt:TiO_2 top layer (brown curve).

As shown in this graph an anodically shifted onset potential at +400 mV is observed for the sample with ALD TiO_2 interlayer. The slope of the graph indicates, however, an increase in resistivity of the sample. Although the onset potential improved, the photocurrent density at the redox potential shows no improvement. Saturation photocurrent densities reach, as expected, the same value independently on the presence of the interlayer.

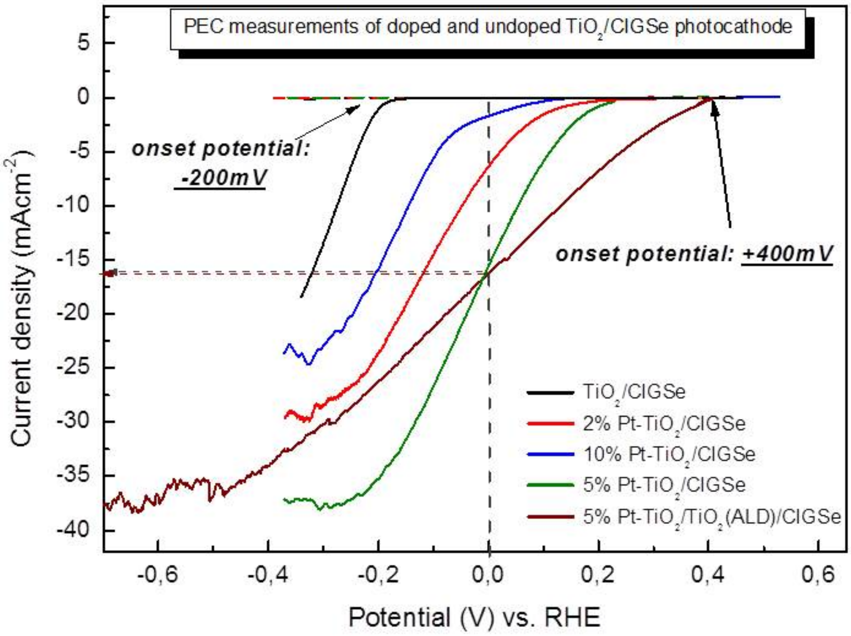

Figure 5.20: Comparison of the current-voltage behavior of the undoped $TiO_2-Cu(In,Ga)Se_2$ (black curve), $Pt:TiO_2-Cu(In,Ga)Se_2$ compsoite photocathode with $Pt:TiO_2-TiO_2(ALD)-Cu(In,Ga)Se_2$ sample. The best current-voltage behavior is observed for the sample with TiO_2 (by ALD) interface layer and shows an anodically shifted onset potential at +400 mV (brown curve); Electrolyte: 0.5 M H_2SO_4, pH0.3. Photoelectrodes were measured under near AM1.5 (100 mW/cm^2) conditions.

5.2 EPD-prepared semiconductor electrodes for electrocatalytic and photo-assisted evolution of oxygen

Electrochemical evolution of oxygen requires immobilization of suitable electrocatalysts on semiconductor supports. Two types of electrocatalysts were investigated, (i) Co-substituted ZnO, ZnO:Co, and (ii) RuO_2 in order to realize the OER in alkaline as well as in acidic electrolytes. Although FTO is a common semiconductor support for evolution of oxygen, the stabilization of this support in high-concentrated electrolytes is demanding. It will be shown that the electrophoretic deposition of the electrocatalysts resulted concomitantly in formation of a carbon-rich protection layer which stabilized the FTO support upon long-time operation. This finding made it possible to choose finally the even more oxidation-sensitive silicon as support for photo-assisted evolution of oxygen (my work focuses here exclusively on the Si/RuO_2 junction while the corresponding Si/ZnO:Co system was investigated by colleagues of mine). It is noteworthy that the application of silicon in an inorganic-organic configuration schemes represents thereby a major progress. Although doped-silicon is commercially available and its band gap makes it a suitable candidate for photoanode preparation, the susceptibility of this semiconductor to photo-degradation and passivation in aqueous electrolytes, especially under anodic conditions, makes efficient surface protection schemes inevitable to guarantee long-term stable operation. The challenge for proper surface protection is to realize optimum electronic and optical properties in order to benefit most from the technologically advanced semiconductor substrate. In recent approaches, metallic overlayers or compact oxide films have been employed with increasing success and oxidation of the semiconductor upon photoelectrochemical splitting of water could be avoided for extended periods of time [78, 80, 144, 147, 189-191]. Both protection schemes require individual considerations: metallic protection layers have to be devised sufficiently thick in order to compensate structural flaws upon unwanted self-oxidation. Increased thickness, however, attenuates the light reaching the absorber. Sufficiently pin-hole free oxide films, on the other hand, can introduce non-negligible serial resistance to the electrode and, also require mild and complex preparation conditions in order not to compromise the substrate. For both materials, metals and oxides, junction formation with the semiconductor is critical since the achievable photovoltage is easily reduced by partial Fermi-level pinning at the interfacial region [192]. A third material class, organic overlayers is considered a promising alternative route for semiconductor protection: surface terminal groups obtained by alkylation procedures offer nearly ideal electronic passivation and ensure maximum in-built potentials and therefore highest photovoltages [193-195]. Moreover, junction formation with single layers of graphene have been suggested which can help overcoming intricate preparation steps associated with chemical surface functionalization [77]. So far, improved stability could be shown only in aqueous electrolytes where the redox reactions occur at potentials considerably smaller than the water oxidation potential. Therefore, an organic protection scheme for state-of-the-art semiconductors, applicable to solar water splitting, still remains a major challenge.

In the following first part the effect of the organic solvents is investigated upon deposition of ZnO:Co on fluorinated tin oxide supports (FTO). The results section will be finally completed by analysis of the corresponding deposition process of RuO_2 onto silicon.

5.2.1 ZnO:Co on FTO as electrocatalyst in alkaline electrolytes

Three organic solvents (ethanol, acetone and acetonitrile) with varied electrophoretic mobility have been employed for deposition of nanocrystalline ZnO:Co particles onto fluorinated tin oxide supports using the electrophoretic deposition technique. The deposition method is described in section 4.1.2. For fundamental investigations, the catalysts were deposited on FTO. The results is expanded for deposition of presenthesized RuO_2 on n-Si (section 5.2.3) in order to prepare a photoanode working in acidic electrolyte.

5.2.1.1 Effect of the electrophoretic mobility on the quality of the EPD process

In Figure 5.21(a), the effect of the organic solvent on the film thickness (left axis,solid lines) and the density of the layers (right axis, dashed lines) is summarized for varied deposition times. The red, blue and green colors are used for samples prepared in ethanol, acetone and acetonitrile, respectively. Thicknesses of the layers were measured by DEKTAK profilometry and the density of the layers was calculated by measuring the deposited mass. In total, nine samples were prepared by suspending ZnO:Co electrocatalysts in ethanol, acetone and acetonitrile. Electrophoretic deposition was carried out for 4, 7 and 10 min each. As shown in Figure 5.21(a), the resulting layer thicknesses are lowest for ethanol and highest for acetonitrile for each deposition time. The inverse dependence is observed for the calculated density. In general, the deposition rate for each solvent is observed to be constant, i.e. the layer thickness increases linearly with time. The lowest deposition rate occurs in ethanol solution and the highest in acetonitrile solution [196]. The visual appearance of the samples after 10 min is depicted as inset in Figure 5.21(b). An obvious color variation is observed from dark green after deposition from acetonitrile to light green after deposition from ethanol. As shown in Figure 5.21(a), as dashed lines, the variation of the density of the layers proves an increasing porosity with deposition time. This finding is particularly important for electrocatalytic processes where an increased active surface area is crucial for an enhanced electrochemical activity. This observed trend implies that under the applied deposition potential smallest particles reach the substrate first, forming thereby a compact layer, while bigger particles are subsequently deposited with a large number of voids in between. Figure 5.21(a) shows that the densities of the layers prepared in ethanol (red dashed line) are higher than the corresponding densities of those samples prepared in acetone (blue dashed line) and acetonitrile (green dashed line). In the following, the measured layer properties are discussed in terms of EPD theory, i.e. electrophoretic mobility and EPD deposition rate, respectively. By measuring the deposited mass and using Eq.(1) (Hamaker law),[176] the electrophoretic mobility of ZnO:Co in different solvents can be calculated by equation (4.1).

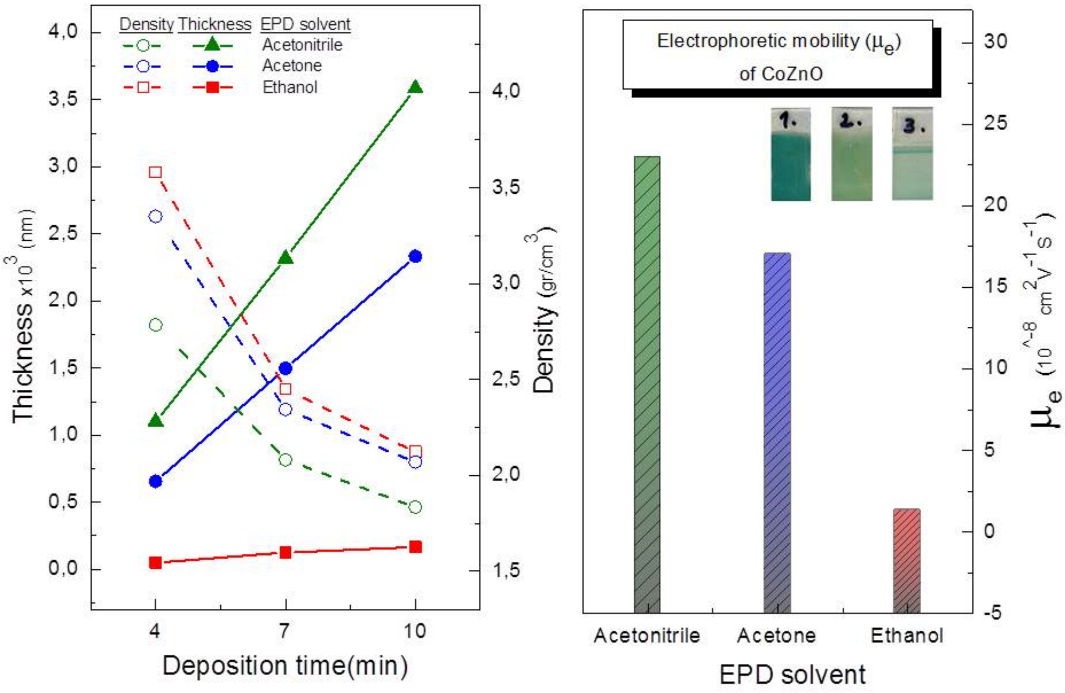

Figure 5.21: (a) Effect of the organic solvent and the deposition time on the thickness and the density of the layers. (b) Role of the organic solvent on the electrophoretic mobility of ZnO:Co particles in the suspension [196].

As described in section 4.1.2, electrophoretic mobility influences the speed of the particles in the media. The results of μ_e for ZnO:Co particles are shown in Figure 5.21(b) and Table 5.1. Higher μ_e values for samples prepared in acetonitrile solvent indicates that the ZnO:Co catalysts are moving with higher velocities in this solution in comparison to acetone and ethanol solvents. The lowest velocity of the particles is observed for the ethanol solvent. This velocity depends on the interaction of the particles with the applied field.
When the catalysts are suspended in the solvent, surface charges are forming around them. These charges are responsible for stabilization and movements of the particles under an applied electric field present in the suspension. Four types of forces can affect the behavior of the particles.

1. Electromagnetic force (E_f) which corresponds to the interaction of the surface charges with the electric field and is equal to the product of the number of charges and the electric field strength (E_f). The magnitude of the electric field was kept constant ($10\,\mathrm{Vcm}^{-1}$) during the EPD process.

2. Drag force (F_d) : this force exerts a force on the particle in opposite direction of its motion. The magnitude of the drag force depends on the velocity of the particle and the properties of the fluid (density) and the size of the particles.

3. Gravitation force (F_g): this force points downwards and depends on the mass of the particles.

4. Buoyancy force (F_b): this force points upwards and is caused by the fluid, reducing thereby the weight of an immersed particle. It is equal to the product of the fluid's viscosity (ρ_f), g (9.8 ms^{-2}) and the volume of the particles.

The schematic of these forces is shown in Figure 5.22. If the electromagnetic force is larger than the sum of the three other forces, the particle moves toward the anode and is deposited there. Otherwise the particle settles at the bottom of the beaker in the case of a buoyancy force lower than the gravitational force.

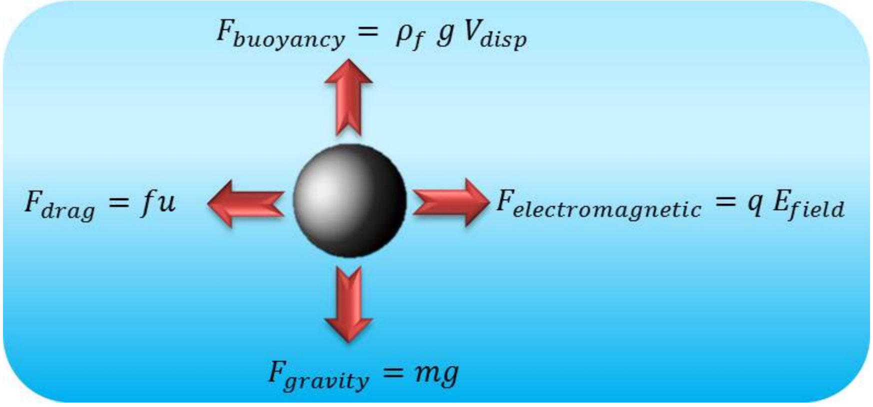
$F_{buoyancy} = \rho_f \, g \, V_{disp}$
$F_{drag} = fu$
$F_{electromagnetic} = q \, E_{field}$
$F_{gravity} = mg$

Figure 5.22: Diagram of forces influencing the movement of the dispersed particle.

Since the magnitude of the electric field was kept constant (10 Vcm^{-1}) during the EPD process, the magnitude of the electromagnetic force depends on the amount of charges induced at the surface of the particle built upon electrochemical equilibration with the solvent. Different parameters like polarity and viscosity of the suspension also influence the amount of induced charges. All these parameters are summarized as zeta potential parameter (ζ) in the Smoluchowski correlation, given by Eq.(4.2) described in section 4.1.2.

The electrophoretic mobility and the zeta potential of ZnO:Co particles in different solvents were accordingly calculated by Eq. 4.1 and Eq. 4.2 and are given in Figure 5.23. As shown in this figure, both the electrophoretic mobility and the zeta potential decreased slightly during increasing deposition times for all the solvents [196]. This effect is accounted for by the progressive consumption of iodine which is required to induce a positive charge at the surface of the particles. The decreasing iodine concentration then results in a lower zeta potential and, consequently, smaller deposition rates.

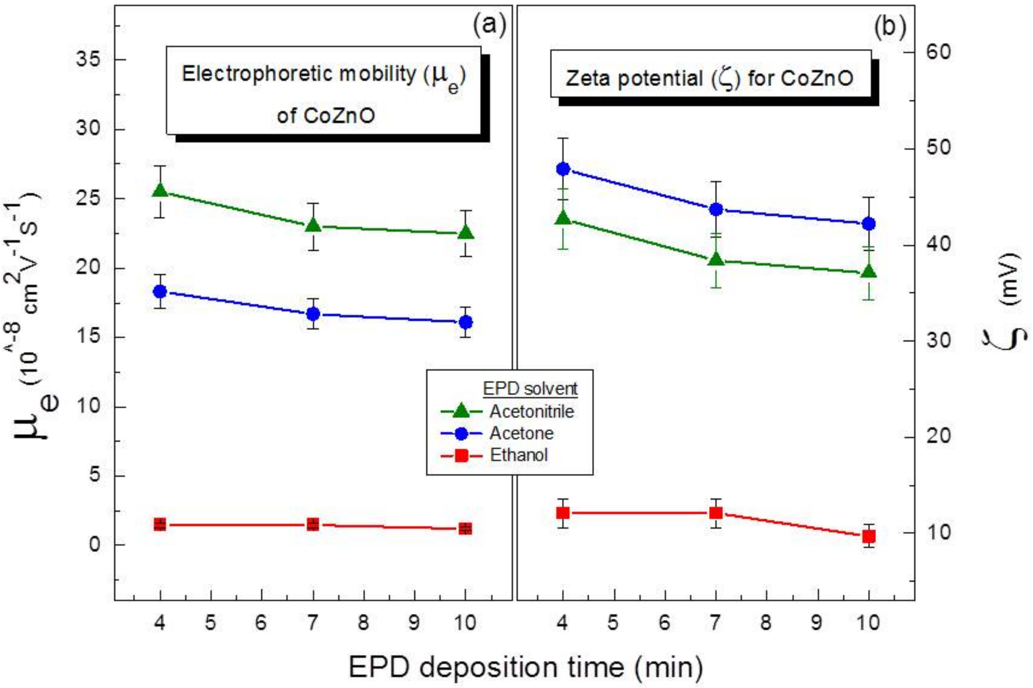

Figure 5.23: (a), (b) Effect of the organic solvent as a function of deposition time on the electrophoretic mobility and the zeta potential of the ZnO:Co particles [196].

As shown in Figure 5.23, there is a big difference between the zeta potential of ZnO:Co particles dissolved in ethanol and those dissolved in acetone and acetonitrile. This effect can be understood by the different activity of the solvents towards iodine and finally the suspended particles. Acetonitrile and acetone are polar aprotic solvents; the nitrile group in acetonitrile and the carbonyl group in acetone are proton acceptors. Polar aprotic solvents cannot participate in hydrogen bonding because of lack of O-H or N-H groups. Therefore, iodine in the solution is free and induces a positive charge at the ZnO:Co particles. In the case of ethanol, the polar-protic solvent participates in hydrogen bonding which is a powerful intermolecular force. Hydrogen bonds are more easily formed between hydrogen of the hydroxyl group and the nucleophile iodine. Therefore the concentration of iodine in the ethanol solution decreases in comparison to acetonitrile and acetone. As a consequence, the amount of positive surface charge at the surface of the ZnO:Co particles is lowered and the horizontal movement of the particles towards the cathode is more impeded by vertical forces, i.e. gravitation. As a further consequence, formation of hydroiodic acid is facilitated in ethanol. The generation of acid can influence the deposition of the layers in two ways: firstly, the ZnO:Co particles are partially etched, i.e. they decrease in size; secondly, already deposited particles can be released from the surface if the etching process affects the interface between the FTO support and the particles. Both effects therefore contribute to an overall limited layer thickness. Moreover, the apparent film porosity is reduced since small particles can be immobilized in a denser layer structure than larger particles. It should be noted that also for acetone formation of hydroiodic acid can be expected: due to the keton-enol tautomerism of acetone, a small fraction of -OH bonds are present in solution. It is assumed that the kinetics of this transformation is shifted towards the enol species in the presence of iodine. Therefore, film properties of acetone-prepared samples, i.e. the density of the films, as well as electrophoretic parameters, i.e. the EPD deposition rate, are expected to reveal the impact of minute concentrations of hydroiodic acid. In fact, the data of Figure 5.21 demonstrate that layer thickness and porosity as well as electrophoretic mobility are all slightly smaller than observed for acetonitrile. Only the calculated zeta potential in Figure 5.23(b) appears increased which has to be attributed to the larger dielectric constant of acetonitrile. The results are summerized in table 5.1.

	ZnO:Co in Ethanol	ZnO:Co in Acetone	ZnO:Co in Acetonitrile
$\mu(cm^2V^{-1}S^{-1}) \times 10^{-8}$			
4 min EPD	1.46	18.3	25.5
7 min EPD	1.46	16.7	23
10 min EPD	1.17	16.1	22.5
ζ potential(mv)			
4 min EPD	12.1	47.9	42.7
7 min EPD	12.1	43.7	38.4
10 min EPD	9.7	42.2	37.1
Deposited Mass(mg)			
4 min EPD	0.04	0.5	0.7
7 min EPD	0.07	0.8	1.1
10 min EPD	0.08	1.1	1.5
Thickness(nm)			
4 min EPD	49	654.58	1102.74
7 min EPD	125.29	1496.94	2318.36
10 min EPD	165.34	2330.87	3585.11

Table 5.1: Electrophoretic deposition data

5.2.1.2 Effect of the organic solvent on the catalytic activity of ZnO:Co electrodes

The electrochemical behavior of nanocrystalline ZnO:Co particles deposited onto fluorinated tin oxide supports (FTO) samples was investigated by cyclic voltammetry in 1N KOH, pH14. Under these conditions, the redox potential for oxygen evolution is at $E_0 = +\ 0.2$ V versus Ag/AgCl. Figure 5.24(a) shows the current-voltage behavior in a three-electrode arrangement for the samples prepared in acetone (blue curve), acetonitrile (green curve) and ethanol (red curve). Corresponding two-electrode measurements are shown in Figure 5.24(b). Evaluation of the electrochemical activity for evolution of oxygen proves a clear solvent-dependence with highest activity upon deposition from acetonitrile and lowest activity upon deposition from ethanol. Pronounced oxidation and reduction peaks around 0.4 V Ag/AgCl are visible for samples prepared in acetone and acetonitrile. XPS results, As already reported earlier[47], a transition of Co(II) to Co(III) occurs upon OER. For ethanol-prepared samples this reversible oxidation-reduction behavior is much less visible. These observations are clearly related to the difference in porosity of the respective samples and therefore the difference in active surface area. Correspondingly, the current onset potentials are visibly improved for acetonitrile and acetone in comparison to ethanol. Galvanostatic determination of the potential corresponding to 1 $mAcm^{-2}$ therefore proves the enhanced activity over ethanol-prepared samples (see inset in Figure 5.24(a)): the respective potentials are 362, 300 and 290 mV, confirming thereby the slight improvement by usage of acetonitrile-based suspensions.

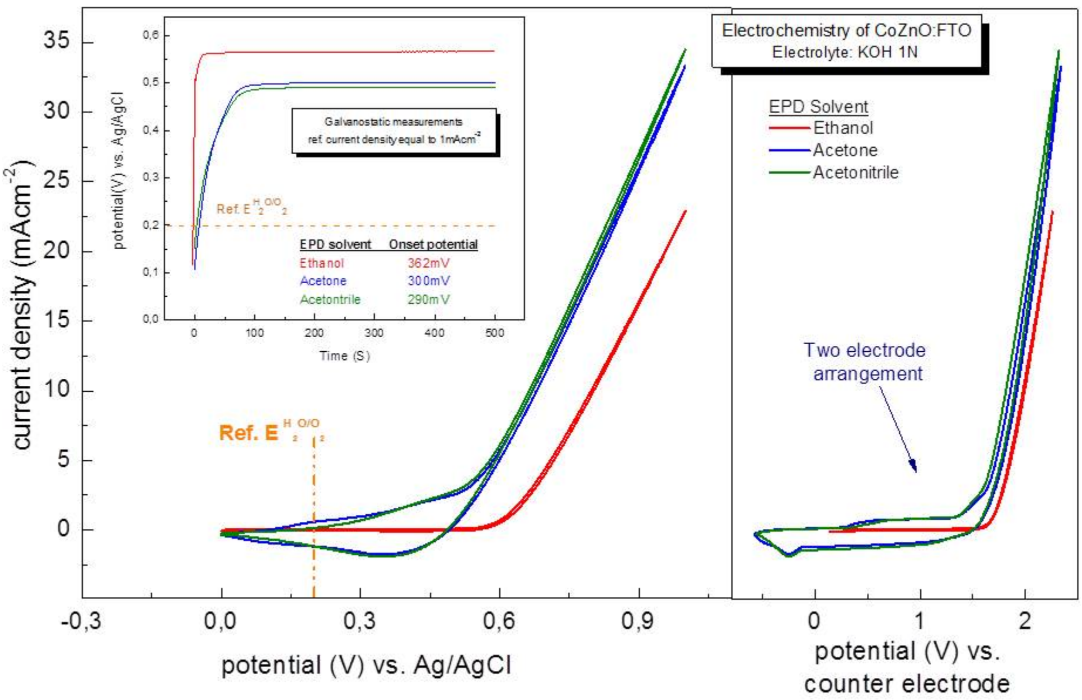

Figure 5.24: (a) Current voltage behavior of ZnO:Co prepared in different organic solvents ethanol (red line), acetone (blue line) and acetonitrile (green line) and deposited on FTO substrates. (b) Galvanostatic measurements of the layers corresponding to a current density of 1 $mAcm^{-2}$. Electrolyte: KOH 1N.

Using differential electrochemical mass spectroscopy it is finally proven that commencing evolution of oxygen is detected beyond potentials measured above (Figure 5.25). The right curve shows the O_2 mass signal for a sample prepared in acetonitrile (Figure 5.25(a)) and the left curve shows the O_2 mass signal for a sample prepared in ethanol (Figure 5.25(b)). Since the performance of the samples prepared in acetone and acetonitrile are very similar, corresponding mass signals are only shown for the acetonitrile and ethanol solvent. Putting the observation of thicker and more porous films, prepared in acetonitrile and acetone (Figure 5.25a), into relation with higher OER activity (Figure 5.24) and lower overpotentials (inset in Figure 5.24), it is concluded that the size of the active surface area is the most crucial distinguishing film property. This property, in turn, is directly related to the difference in electrophoretic mobility of the ZnO:Co particles in the respective organic solvent. It should be noted that due to the specifics of the DEMS setup diffusion-related additional overpotentials are present and have to be related to the small spacing between the sample and the used membrane.

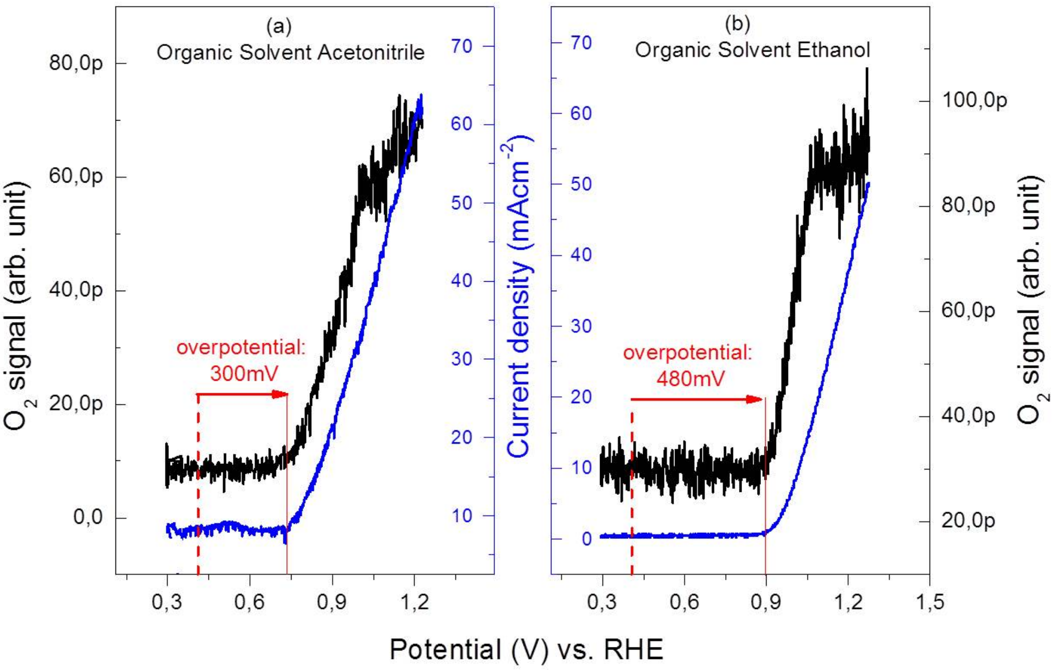

Figure 5.25: Differential electrochemical mass spectroscopy (DEMS) measurements for O_2 evolution on ZnO:Co deposited on FTO, dissolved in acetonitrile (a) and ethanol (b). Electrolyte: KOH 1N.

Stability of the respective ZnO:Co films in 1N KOH, pH14, was measured over a period of 24 hours and is shown in Figure 5.26. Potentials were adjusted such that current densities are close to 4 $mAcm^{-2}$ in the beginning. For clarity, the curves in Figure 5.26(a) are presented after applying a positive small shift. For all samples a current decrease by about 10% is observed. Cross-check analysis of the behavior of bare FTO in 1N KOH, however, proved pronounced instability of the support (Figure 5.26(a)). In order to achieve more insight into the long-term behavior, an ethanol-prepared sample was additionally tested over 72 hours (Figure 5.26(b)). After that time, the electrolyte was renewed as indicated by an arrow. It can be seen that the renewed electrolyte permits partial compensation of the current decrease. Initial high values, however, are not reached anymore. This finding can be attributed either to a loss in activity of the catalytic material or to structural flaws within the film which lead to progressive degradation of the FTO support. These results point to an efficient protection of the FTO support by the ethanol-prepared film which is, according to the analysis above, characterized by the highest structural density of the investigated films.

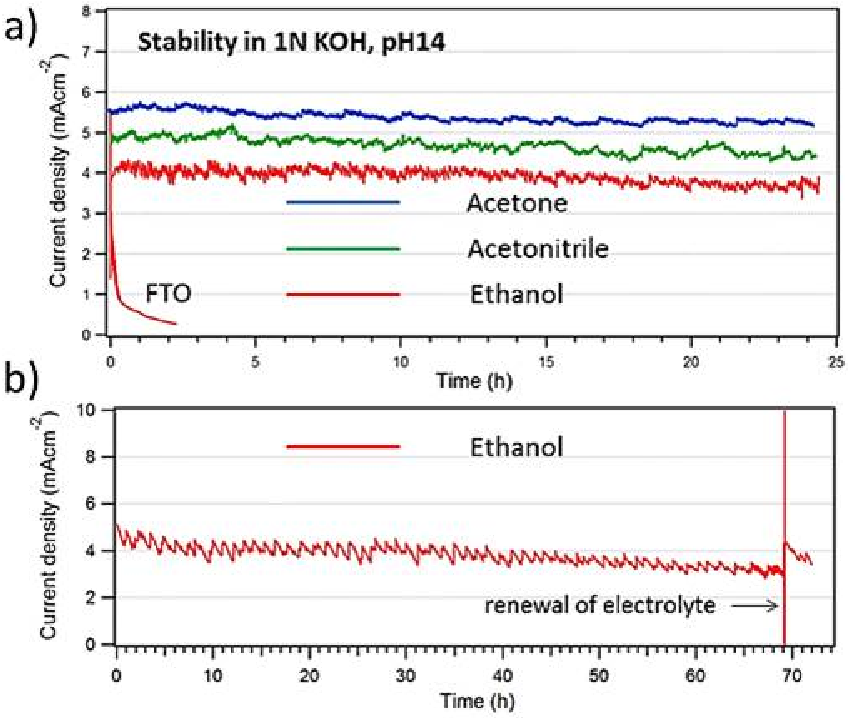

Figure 5.26: Stability assessment of ZnO:Co, prepared from ethanol-containing suspensions, at pH14. For comparison, the rapid degradation of a bare FTO substrate is indicated.

The nature of these protecive properties for the support have been recently investigated by M. Lublow who suggested the formation of a carbonnaceous oxyhydroxide, concomitantly forming at the support's surface during EPD (see planned publication No. 6 in section 7.3). As precursor material for the formation of the oxyhydroxide, dissolution products of ZnO:Co in the presence of hydroiodic acid appear likely. It can be therefore assumed that the prepared ZnO:Co/FTO electrodes enclose an interfacial region of carbon-containing composite material with amorphous zinc and cobalt oxyhydroxides rather than to be composed of pure ZnO:Co nanocrystals. This finding of a dense carbonaceous oxide layer with protective properties was inspirational for direct deposition of water oxidation catalysts onto oxidation-sensitive semicundoctor supports to be discussed further below with the example of RuO_2/Si. The investigation of the role of carbon (both sp^3 and sp^2 hybridized) as addition to transition oxide metal layers is continued.

5.2.1.3 Optical analysis of ZnO:Co on FTO by UV-VIS and SPV

Optical measurements include transmission spectroscopy and normalized SPV amplitudes of ZnO:Co films prepared in different solvents for 7 min deposition time each. The results are shown in Figure 5.27(a-b), respectively. The red, green and blue curves show the behavior of the samples prepared in ethanol, acetonitrile and acetone, respectively. The samples were illuminated from the front side, i.e. light passed through the ZnO:Co film first and only photons, not absorbed by ZnO:Co reached the FTO support. Optical transmittance spectra for ZnO:Co films prepared in different solvents for 7 min are shown in Figure 5.27(a). While acetonitrile-and acetone-prepared samples show strong attenuation of the incident light, highest transmittance is achieved with samples prepared from ethanol solutions. Transmittance values near 70% therefore suggest this preparation method as suitable for photoactive supports to be discussed further below. The optical band gap of ZnO:Co, obtained by extrapolation of the low-energy feature to the x-axis is about 2 eV. The second absorption edge near 3.3 eV corresponds to the optical band gap of the FTO support. In Figure 5.27(a), the SPV response indicates that photo-induced excess charge carriers are separated in space [197-198]. The SPV amplitude for all the samples exhibited two response peaks (as in corresponding UV-VIS spectra), the curves increased sharply at a photon energy of about 1.7-1.8 eV indicating the onset of tail states (defect levels) within the band gap of the material (see extrapolated straight lines in Figure 5.27(b)). The second structure, to be attributed to FTO, is not shown in Figure 5.27(b) for clarity. It should be noted that the onset energy of electronic states extending into the band gap is always lower than the corresponding optical band gap.

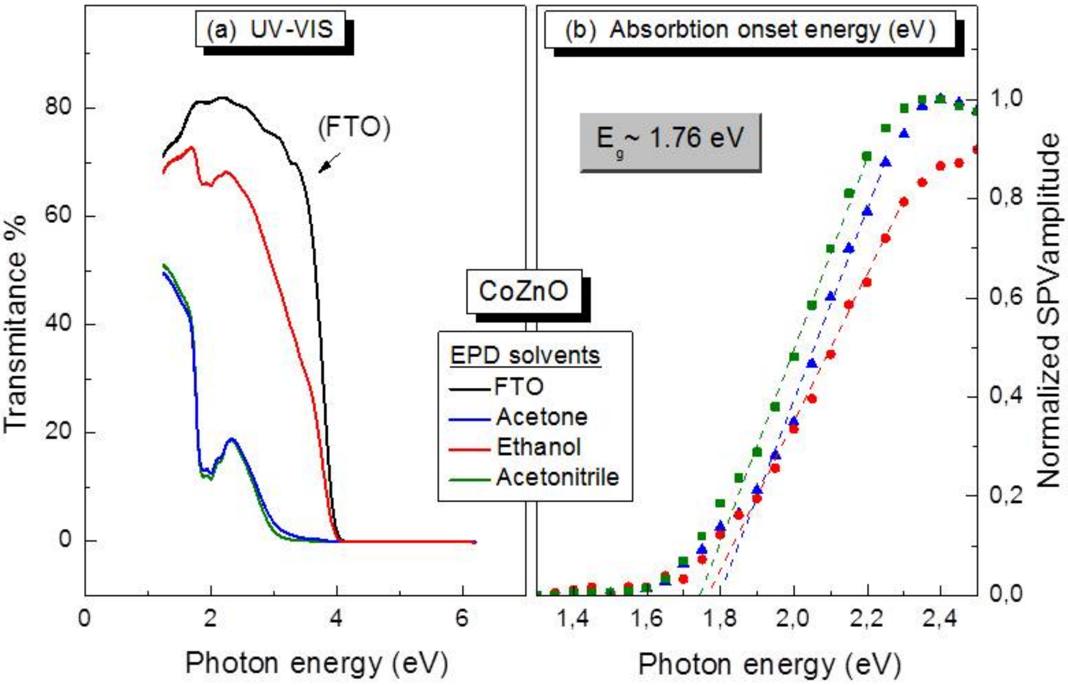

Figure 5.27: optical characterization of ZnO:Co deposited on FTO substrates (a) Transmission spectra as a function of wavelength.

X-ray diffraction patterns of ZnO:Co powder (before deposition) and ZnO:Co/FTO junctions before and after electrochemical measurements (EC) are shown in Figure 5.28. GIXRD measurements were carried out at 0.2° angle of incidence. The results reveal a polycrystalline, highly oriented film directly after electrophoretic deposition. The dominant peaks are assigned to 101, 100 and 002 reflections. Using the Scherrer equation, average particle sizes of 24, 17 and 21 nm were calculated for the corresponding peaks, respectively. After EC measurements there is a visible change in the X-ray reflection spectra (Figure 5.28 (b)). The intensity of the peaks appears reduced and crystal sizes of 18, 12 and 16 nm are obtained. In correspondence to earlier findings by Pfrommer et al. [47], this change has to be attributed to a continuous transformation of the crystalline into an amorphous phase, i.e. the nanocrystalline powder acts as a core-precatalyst whose surface area continuously transforms to the final electrocatalytic material upon evolution of oxygen.

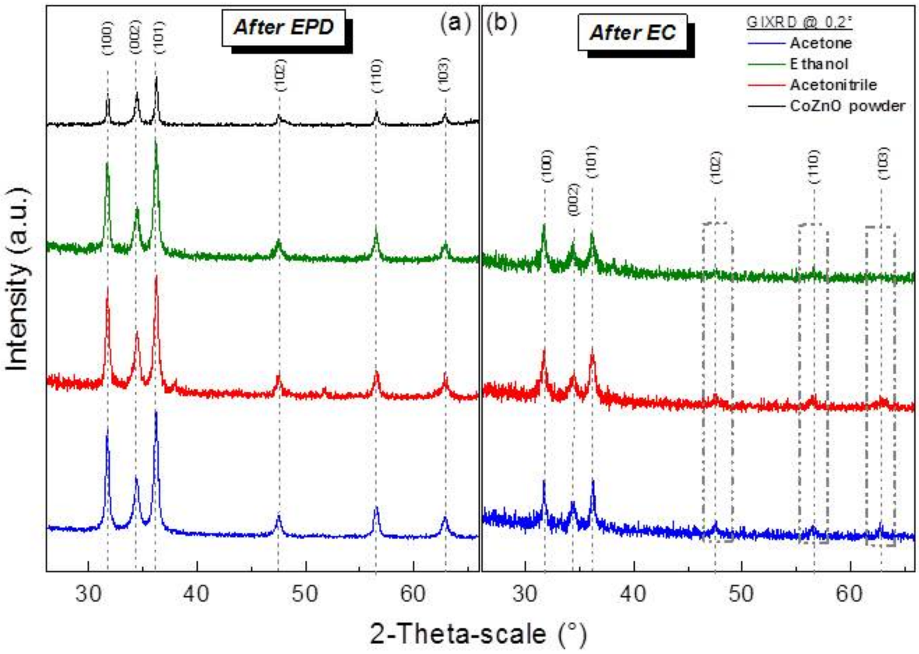

Figure 5.28: GIXRD diagram of ZnO:Co prepared in ethanol (red line), acetone (blue line) and acetonitrile (green line) (a) after electrophoretic deposition and (b) after electrochemical measurements.

Correspondingly, elemental analysis by EDX proves considerable differences in the Zn:Co ratio before and after OER. The results are shown in Figure 5.29, the colored lines show the EDX pattern for as-prepared samples and the black line indicates the sample after electrochemistry. For all samples, a decreased Zn:Co ratio is observed pointing to preferential dissolution of zinc oxide. Before electrochemical testing, the respective Zn:Co ratios for acetone-, acetonitrile- and ethanol-prepared samples were: 2.5:1, 2.5:1, and 2.6:1, respectively. After EC, ratios of 0.4:1, 0.5:1 and 0.1:1 were calculated. The variation of these latter numbers can be understood by the difference of the respective (Zn-poor) surface to (Zn-rich) volume ratio after electrochemistry. According to Figure 5.21, ethanol prepared samples show the lowest film thickness and porosity, i.e. only small nanoparticles are deposited with a smaller surface-to-volume ratio than acetonitrile- and acetone-prepared films. Consequently, the Zn-poor surface after OER region has a stronger impact on the overall Zn:Co ratio.

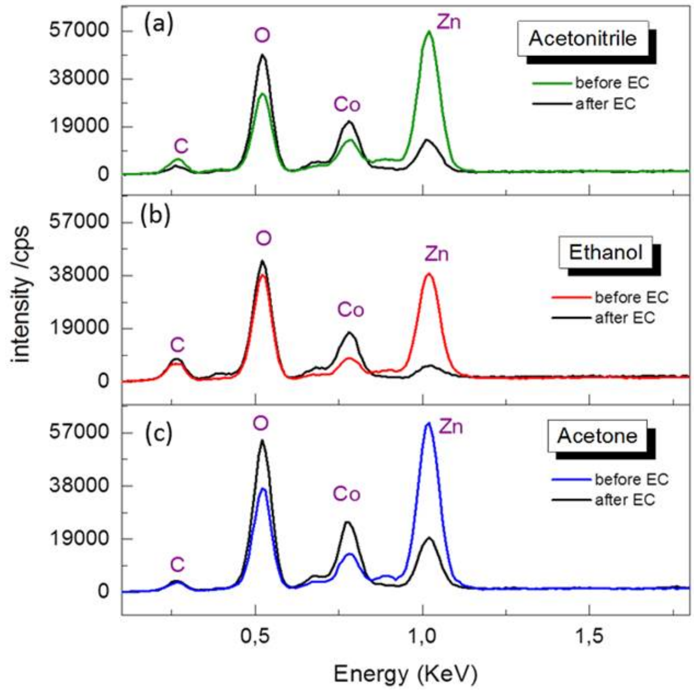

Figure 5.29: EDX spectra of ZnO:Co deposited on FTO in acetonitrile (a), ethanol (b) and acetone (c) before and after electrochemistry measurements.

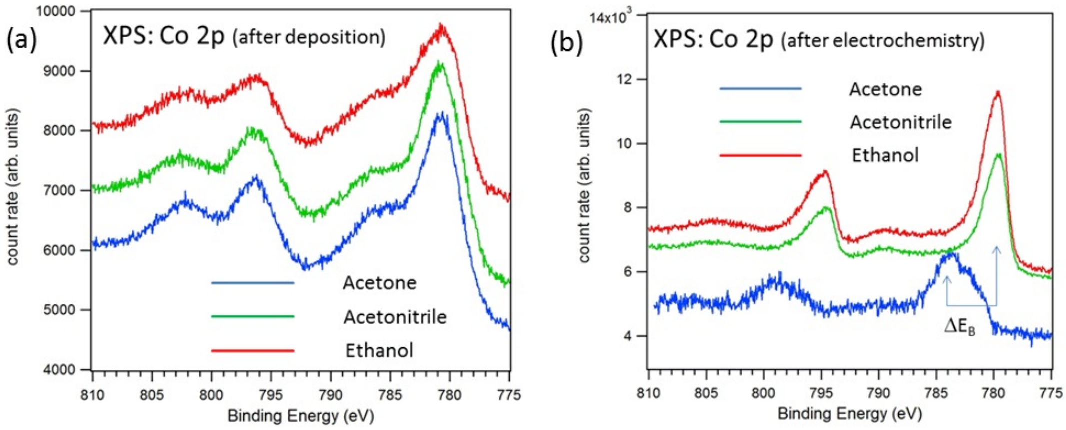

(c) Acetone-prepared

(d) Ethanol-prepared

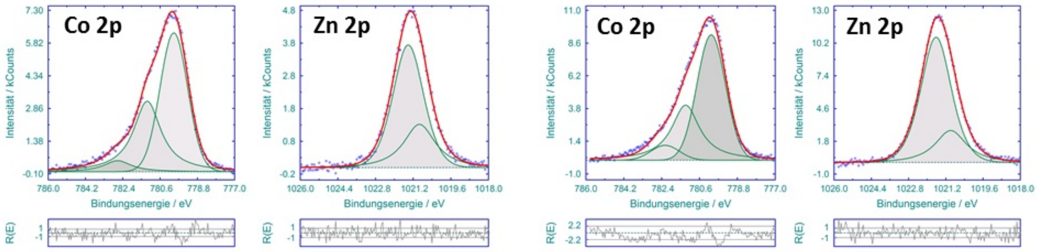

Figure 5.30: XPS analysis of Co 2p signal (a) before electrochemistry for samples prepared in acetone (blue curve), acetonitrile (green curve) and ethanol (red). (b) XPS results for the Co 2p signal for acetone prepared sample before and after electrochemistry (c) and (d) comparative deconvolution of the Co 2p and Zn 2p signals for samples prepared in acetone and ethanol, respectively.[196].

In Figure 5.30, XPS analysis of ZnO:Co is shown after deposition on FTO from acetone-, acetonitrile- and ethanol-prepared suspensions. The as-prepared samples (Figure 5.30 a) showed high resistivity of the films. As a consequence, photoelectron emission resulted in electrostatic charging, and the spectra were apparently shifted to higher binding energies. The respective shifts (about 3 eV for acetonitrile and acetone and about 10 eV for acetone) were corrected using the C 1s core-level signal of adventitious carbon as reference energy. For all samples, pronounced shake-up signals were detected at binding energies of about 787 and 803 eV. The presence of these features is attributed to a Co(II) oxidation state [199]. After evolution of oxygen in 1N KOH, acetonitrile- and ethanol-prepared samples did not show any charging while binding energies of the acetone-prepared sample still were shifted by about 3 eV (Figure 5.30 b). Detailed quantitative analysis was therefore carried out only for the Co 2p and Zn 2p signals, measured for acetonitrile- and ethanol-prepared films (Figures 5.30 c and d). Shake-up satellite features are much less pronounced, indicative for the transition of the cobalt oxidation state from Co(II) to Co(III). Deconvolution of the Co 2p signal resulted in three substructures. The main peak lines at about 779.9 and 781.2 eV are attributed to $\mathsf{Co_3O_4}$ and $\mathsf{Co(OH)_2}$, respectively. A third structure at about 782.5 eV results from imperfect subtraction of the 2p signal from the measured curve, i.e. this feature indicates the onset of the following satellite structure. The corresponding Zn 2p signals exhibit two sub-structures at about 1021 and 1021.5 eV. The main struture at 1021.5 eV is attributed to ZnO. The smaller feature at lower binding energy cannot be unambiguously identified. In order to determine the Co:Zn ratio of the films within the escape depth of photoelectrons, i.e. within about 1 nm [200], the integral areas, I_{Co} and I_{Zn}, beneath the curves were calculated and normalized by the corresponding photoionization cross sections of the 2p core-level signals for an excitation energy of 1486.3 eV ($\sigma_{Co} = 0.26$, $\sigma_{Zn}=0.39$). The ratio can then be expressed as $\sigma_{Co}^{-1} \times I_{Co}/\sigma_{Zn}^{-1} \times I_{Zn}$. For the acetonitrile-prepared sample, a ratio of 3:1 was calculated in approximate agreement of corresponding EDX analysis which resulted in a (more volume-sensitive) value of 2:1. The deviation in the ratio, obtained by the two methods, can be explained by the fact that XPS probes more the active surface area, i.e. the sites where Zn is leaching into the electrolyte upon evolution of oxygen. For the ethanol-prepared sample, the corresponding XPS-determined ratio is 1.7:1. This value is smaller than for the acetonitrile-prepared sample (3:1) and much smaller than the one obtained by EDX analysis (10:1). Two effects become thereby apparent: firstly, the ethanol-prepared sample is less active, in correspondence with measured C-V curves, and leaching of Zn proceeds at a slower rate; secondly, the volume of the film suffered from loss of Zn already upon preparation. Probably, the HI-containing suspension dissolved considerable amounts of the ZnO:Co particles, and the molecular dissolution products were deposited as an amorphous Zn-poor film. The amorphous morphology was already suggested by TEM analysis. Remnant particles, finally, were deposited on the top of this amorphous layer due to slower deposition kinetics in comparison to molecular material. Thereby, XPS detects the stoichiometric ratio of these particles at the surface while EDX probes more the volume of the film which appears to strongly deviate from the presynthesized ZnO:Co particles. These findings help clarifying the lower performance of the ethanol-prepared sample: while the surface area appears to consist of the same active phase as in the case of acetonitrile-prepared samples, the amorphous sub-layer structure may introduce either structural impediments, i.e. the film is to smooth to introduce an enlarged surface area, or an additional barrier for charge transfer, caused by the amorphous film, lowers the activity. (XPS measurments were done by Ch. Höhn at HZB and

XPS analysis was carried out under supervision of Dr. M. Lublow)

5.2.1.4 Morphological analysis by SEM/ EDX/ TEM

SEM and TEM images for ZnO:Co are shown in Figures 5.31-33 deposited from the three different solvents, acetonitrile, acetone and ethanol, respectively. Left-row images depict the materials structure before electrochemical operation. Right-row images show the corresponding analyses after electrochemistry. On the larger scale of the SEM images, the least changes are visible with samples deposited from ethanol (Figure 5.33 (a/b)). Due to the higher porosity and therefore higher active surface area, those changes are more pronounced for samples prepared from acetonitrile and acetone (Figure 5.31 and 5.32, respectively). Closer inspection by TEM analysis of small lamellae (and selected area electron diffraction images) reveals the commencing transition to an amorphous phase by exposure to the electrolyte under anodic potential (compare the respective images c through f). This transition is almost completed with ethanol-prepared samples while with acetonitrile and acetone prepared samples, distinguishable diffraction patterns can still be observed. (TEM measurements were done by C. GÃűble Pfrommer at TU-Berlin)

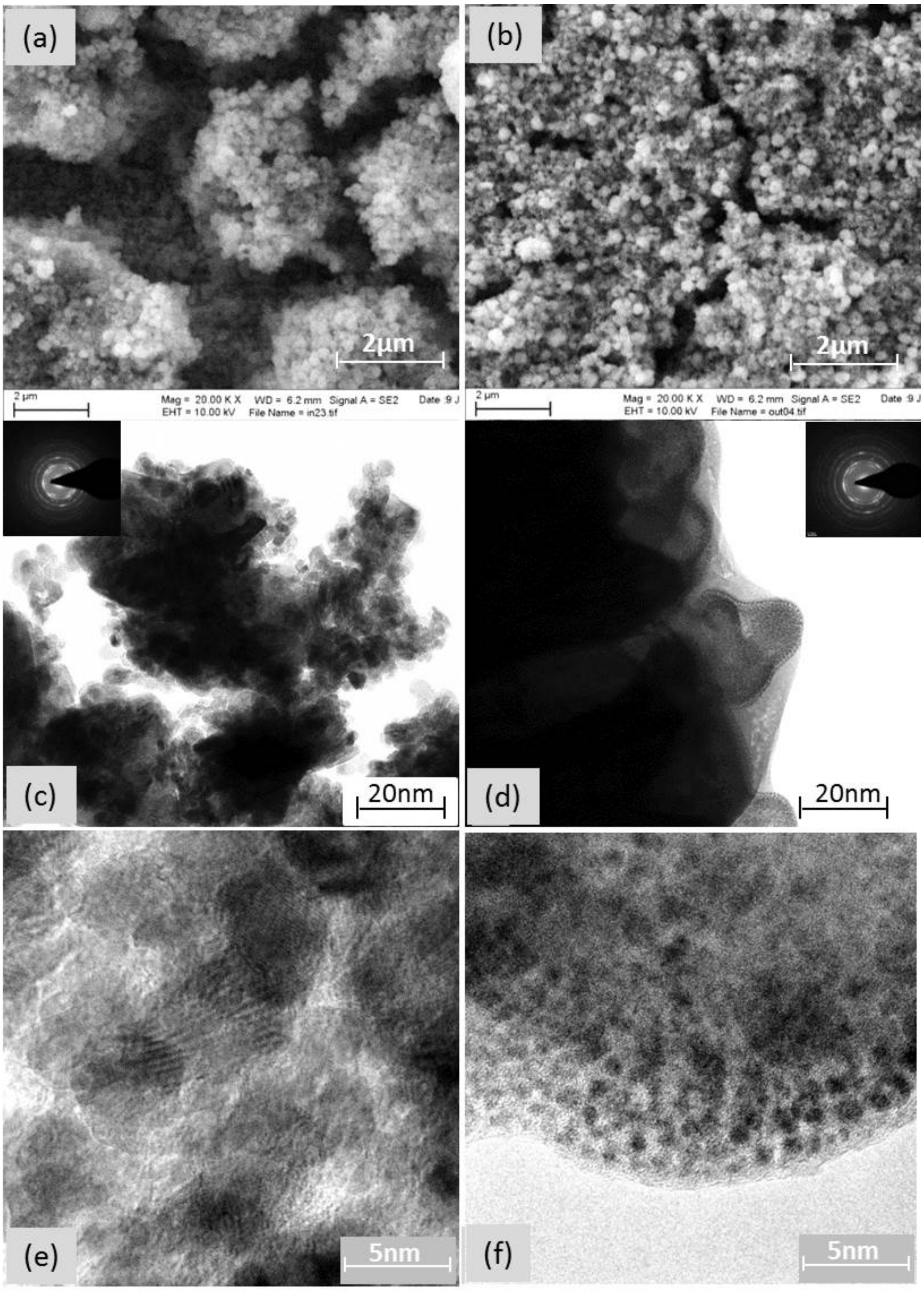
(a)
2µm
2 µm
Mag = 20.00 K X WD = 6.2 mm Signal A = SE2 Date :9 J
EHT = 10.00 kV File Name = in23.tif
(b)
2µm
2 µm
Mag = 20.00 K X WD = 6.2 mm Signal A = SE2 Date :9 J
EHT = 10.00 kV File Name = out04.tif
(c)
20nm
(d)
20nm
(e)
5nm
(f)
5nm

Figure 5.31: Microscopy characterization of ZnO:Co morphologies after EPD using acetonitrile as solvent. (a) and (b) SEM surface view before and after electrochemistry, respectively. (c) and (d) corresponding TEM images of ZnO:Co lamellae before and after electrochemistry, respectively. (e) and (f) Magnified TEM images of ZnO:Co lamellae before and after electrochemistry, respectively [196].

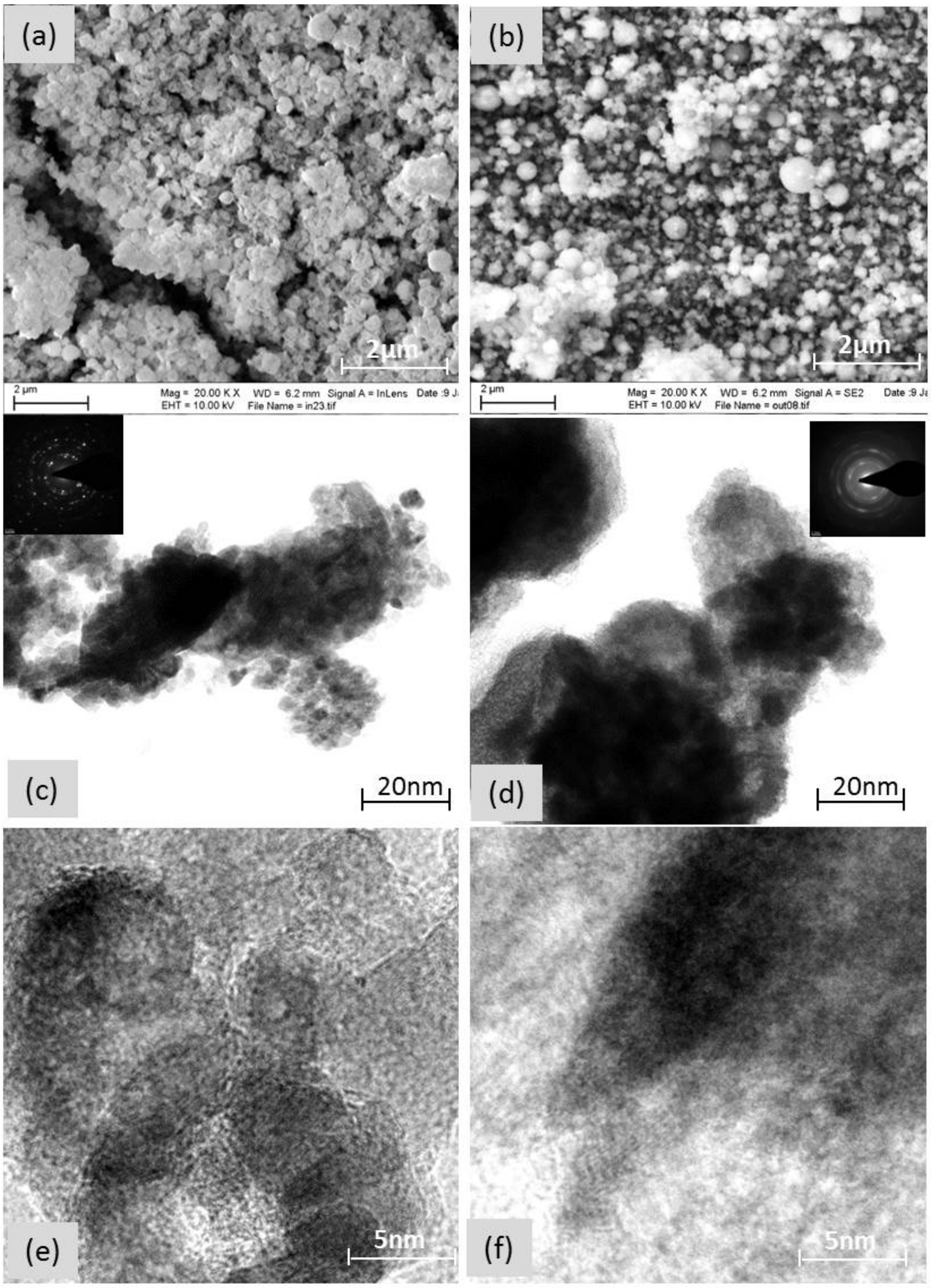
(a)
2µm
2 µm
Mag = 20.00 K X
WD = 6.2 mm
Signal A = InLens
Date :9 J
EHT = 10.00 kV
File Name = in23.tif
(b)
2µm
2 µm
Mag = 20.00 K X
WD = 6.2 mm
Signal A = SE2
Date :9 Ja
EHT = 10.00 kV
File Name = out08.tif
(c)
20nm
(d)
20nm
(e)
5nm
(f)
5nm

Figure 5.32: Microscopy characterization of ZnO:Co morphologies after EPD using acetone as solvent. (a) and (b) SEM surface view before and after electrochemistry, respectively. (c) and (d) corresponding TEM images of ZnO:Co lamellae before and after electrochemistry, respectively. (e) and (f) Magnified TEM images of ZnO:Co lamellae before and after electrochemistry, respectively [196].

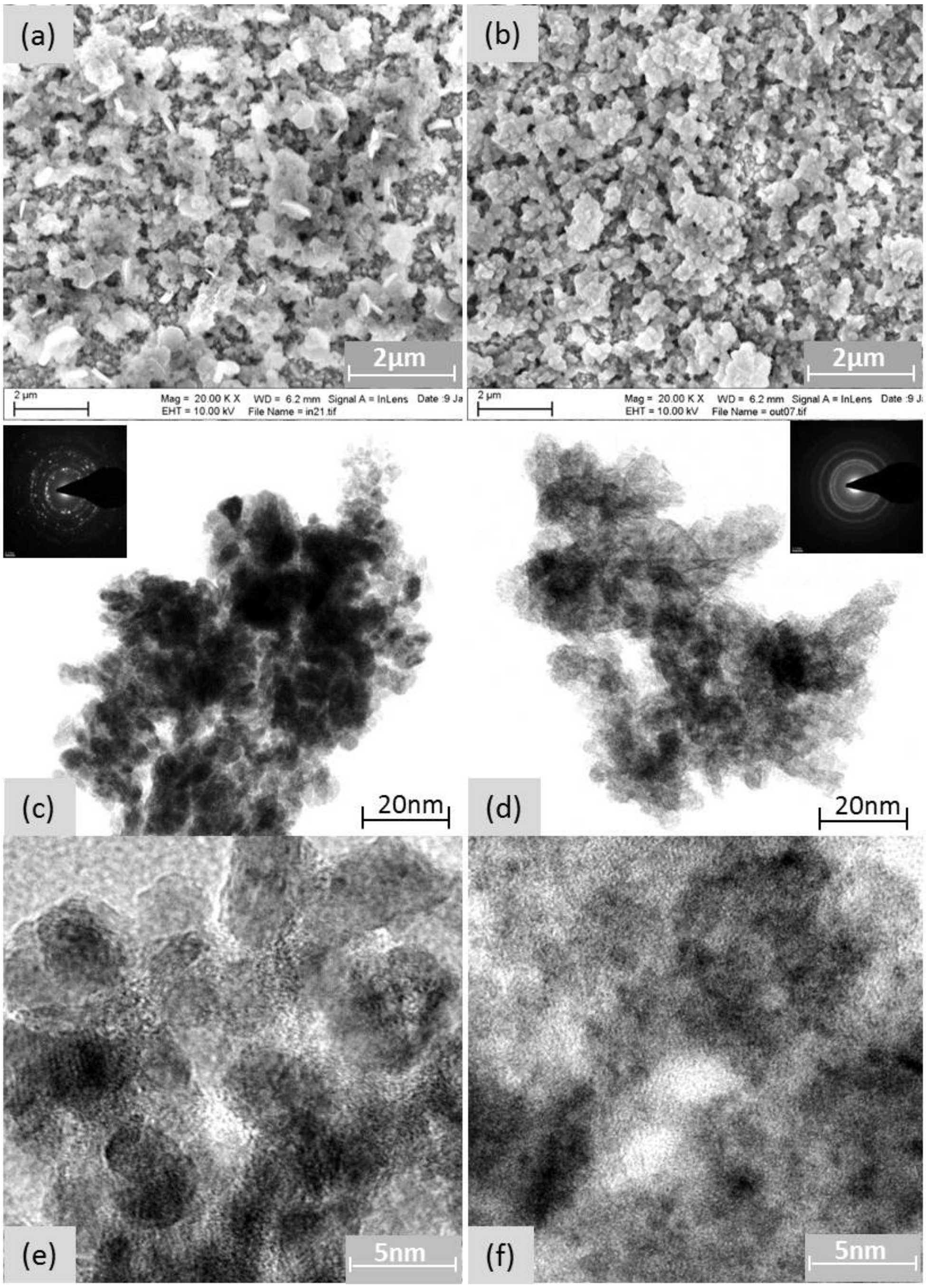
(a)
(b)
2µm
2µm
2 µm
Mag = 20.00 K X WD = 6.2 mm Signal A = InLens Date :9 Ja
EHT = 10.00 kV File Name = in21.tif
2 µm
Mag = 20.00 K X WD = 6.2 mm Signal A = InLens Date :9 J
EHT = 10.00 kV File Name = out07.tif
(c)
20nm
(d)
20nm
(e)
5nm
(f)
5nm

Figure 5.33: Microscopy characterization of ZnO:Co morphologies after EPD using ethanol as solvent. (a) and (b) SEM surface view before and after electrochemistry, respectively. (c) and (d) corresponding TEM images of ZnO:Co lamellae before and after electrochemistry, respectively. (e) and (f) Magnified TEM images of ZnO:Co lamellae before and after electrochemistry, respectively [196].

It is finally shown that the enhanced optical transparency of ethanol-prepared samples can be successfully employed for solar-cell controlled direct water splitting. The schematic of the setup with a triple-junction solar cell (amorphous silicon) is depicted in Figure 5.34. The solar cell characteristic under illumination of 100 $\mathrm{mWcm^{-2}}$ is shown in black.

The electrocatalytic layer is fixed to the photoactive glass front-side of the triple-junction silicon solar cell. Short-circuit photocurrent densities of about 4.2 $\mathrm{mAcm^{-2}}$ results in an efficiency of 5% for direct photo-assisted water splitting. Corresponding photocurrent-voltage curves, measured with Pt-counter electrode, are presented in Figure 5.35. Due to the only small light attenuation by ZnO:Co (prepared in ethanol), about 70% of the short circuit photocurrent can be exploited for light-driven evolution of oxygen. The efficiency thereby amounts to:

$$\eta = \frac{1.23\mathrm{V} \times J_0}{A \times 100\ \mathrm{mWcm^{-2}}} \tag{5.1}$$

Here, J_0 denotes the short-circuit photocurrent density.

Corresponding measurements with acetonitrile- and acetone-prepared samples are also shown with green and blue curves in Figure 5.35(b). They exhibit much lower efficiencies due to large light absorption in the thick electrocatalytic layers. It is worth noting that the modular architecture presented here allows for simple exchange of the ZnO:Co/FTO top-layer once its activity has fallen below a minimum threshold value. By considering the use of low-cost electrocatalysts, this approach appears to be an attractive alternative to approaches where the catalysts are permanently fixed to the photoactive supports.

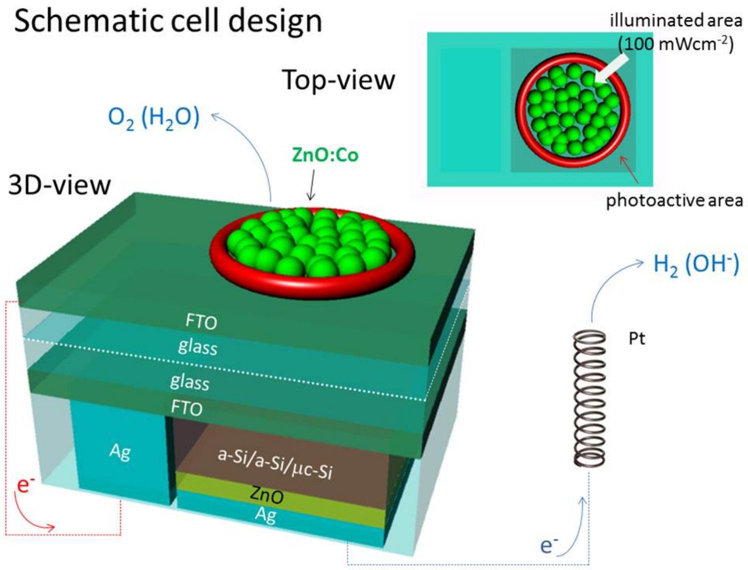

Figure 5.34: Schematic setup of the combined supports, an amorphous/microcrystalline silicon solar cell (bottom) and a ZnO:Co/FTO heterojunction (top). In the top-view, the O-ring is depicted in decreased size in order to stress the photoactive area beneath.

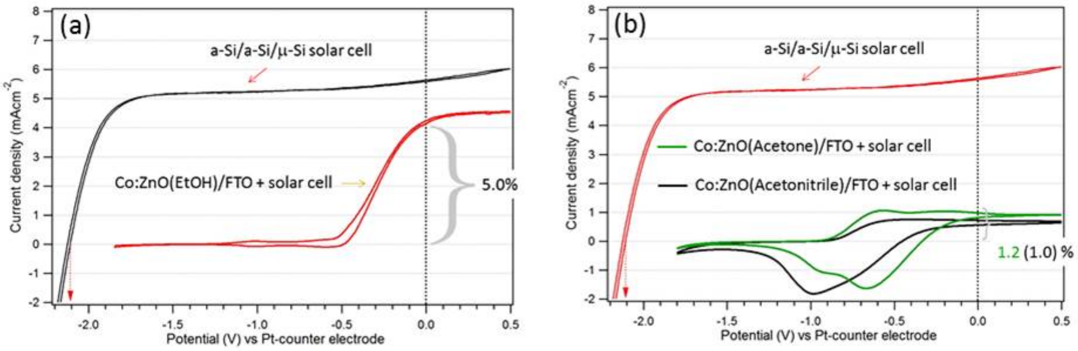

Figure 5.35: (a) Photocurrent-voltage behavior of the silicon triple-junction solar cell (black curve) and the stacking configuration with a top ZnO:Co/FTO layer, prepared from ethanol (red curve). (b) Corresponding stacking configurations with ZnO:Co/FTO layers prepared from acetone (green curve) and acetonitrile (black curve). For comparison the solar cell behavior without electrocatalysts is shown in red [196].

5.2.2 Characterization of RuO_2 on FTO as electrocatalyst in acidic electrolytes

The harsh acidic and oxidizing conditions at the anode render most catalysts inactive or unstable, except for oxides of Ir or Ru. It turns out that RuO_2 is more active than IrO_2 [42], but it is somewhat unstable towards degradation towards RuO_4 [155]. According to the theoretical "volcano" model developed by Rossmeisl, Norskov and coworkers[201], RuO_2 is the most active pure metal oxide catalyst for OER, because it exhibits optimal binding behavior to reaction intermediates [42]. Consequently, in this section presynthesized RuO_2 catalyst was used instead of ZnO:Co on FTO and n-Si substrates in order to prepare (photo-)anodes for acidic electrolytes. EPD deposition parameters were kept constant as in the case of ZnO:Co particles. Firstly, the effect of the chosen organic solvent on the electrode performance was investigated using ethanol, acetone and acetonitrile and FTO substrates. Figure 5.36(a) shows the performance of the RuO_2/FTO electrode tested in H_2SO_4 0.5M in a three electrode configuration and with Ag/AgCl reference electrode. The green, blue and red curves show the current-voltage behavior of the samples prepared in acetonitrile, acetone and ethanol, respectively. As shown in this graph, the electrocatalytic activity of the samples prepared in acetonitrile and acetone show pronounced oxidation-reduction peaks in comparison to the sample prepared in ethanol. Again, as for ZnO:Co, acetonitrile-prepared electrodes (on FTO) prove lowest overpotentials (about 320 mV for 10 $mAcm^{-2}$). The trend of the C-V curves for RuO_2 for the other organic solvents is similar to the behavior observed for ZnO:Co catalysts.

Figure 5.36(b) shows the effect of the organic solvent on the density and thickness of the deposited layers. Similar to ZnO:Co, the sample prepared in ethanol has the thinnest layer (17 nm) and the sample prepared in acetonitrile has the highest thickness (500 nm). The sample prepared in acetone has a thickness of 226 nm. The calculated densities demonstrate that, as expected, the deposited layer in ethanol has the highest density while the acetonitrile-prepared sample has the lowest density. Corresponding conclusions with respect to the porosity hold true as in the case of ZnO:Co.

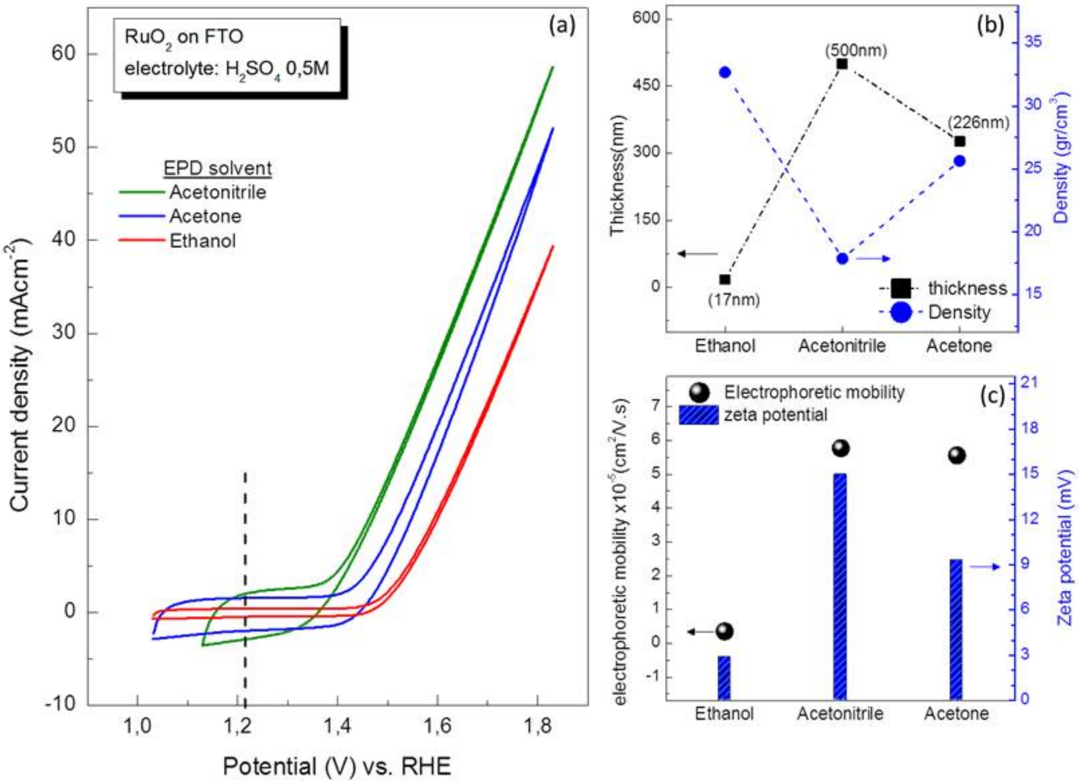

Figure 5.36: (a) Current-voltage behavior of ethanol (red curve), acetone (blue curve) and acetonitrile (green curve) prepared samples in H_2SO_4 0.5 M. (b) Effect of the organic solvent on the thickness and the density of the layers. (c) Role of the organic solvent on the electrophoretic mobility of RuO_2 particles in the suspension.

Electrophoretic mobilities and zeta potentials of RuO_2 were calculated according to Eq. (4.1) and Eq. (4.2). The results (Figure 5.36(c)) are in good agreement with the trends of the thickness and density of the layers. According to these results, RuO_2 particles have highest electrophoretic mobility and zeta potential in the acetonitrile solvent that means the particles gain more charges in the solution. Therefore, under an external electric field the particles have higher speed (higher electrophoretic mobility) and reach sooner the electrode (FTO). Particles in ethanol solvent has the least amount of charges (lowest zeta potential), therefore interaction with the external electric field is low.

5.2.3 RuO_2 /Si photoanode for acidic electrolytes

As shown in Figure 5.36(a), the RuO_2/FTO electrodes have approximately 200-300 mV overpotential. To overcome this overpotential the RuO_2 catalyst were deposited on n-Si to form a hetero-junction photoanode. In this preparation two critical points should be considered. Firstly, RuO_2 is a black powder and absorbs the entire incident light. If it completely covers the absorber (n-Si), the efficiency of the photoanode decreases dramatically. Therefore the aim is to prepare a thin layer, which is less light absorbing. Secondly, Si is well known to be unstable under anodic conditions. Therefore, the deposited layer not only should be catalytically active for OER but also should be pinhole-free to protect the Si substrate from corrosion under anodic condition. It will be shown that the EPD deposition of RuO_2 results in an polymeric interface that integrates near-ideal electronic and electrochemical passivation in an ultrathin layer of 3-4 nm overall thickness (Figure

5.38).

In order to prepare photoanodes from RuO_2 electrocatalyst, presynthesized RuO_2 was dissolved in three organic solvents (ethanol, acetone and acetonitrile) and deposited on n-Si by EPD under cathodic voltage of -10 V for 20 min. Subsequently, the photoanodes were tested in H_2SO_4 0.5M under illumination (AM1.5). The current-voltage behavior of the photoanodes is shown on the left-hand side of Figure 5.37(a-c). The electrocatalytic activity was assessed after deposition on FTO (dashed curves) and n-Si (solid curves) substrates. Red, green and blue curves show the performance of the sample prepared in ethanol, acetonitrile and acetone, respectively. After deposition on silicon supports, the performance of the sample prepared in ethanol (red solid curve) was completely different from samples prepared in acetone and acetonitrile. The sample prepared in ethanol under illumination reaches a saturation current density of 12 $mAcm^{-2}$ at the redox potential. But under illumination the photoelectrodes prepared in acetonitrile and acetone show only a sluggish current increase and are susceptible to degradation within minutes. Since all the materials and procedures were kept constant and only the organic solvent was varied, it is assumed that the major difference of these samples is related to different interfacial regions formed during EPD.

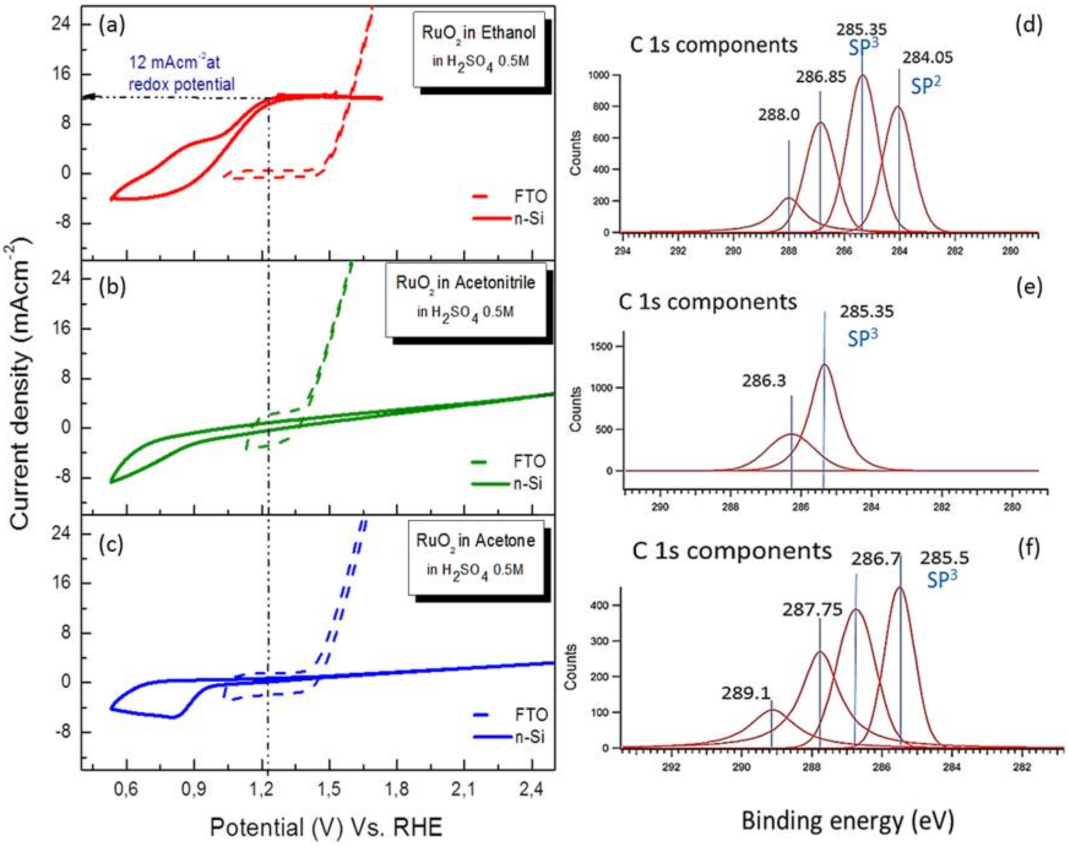

Figure 5.37: (a-c) Current-voltage behavior of ethanol (red curve), acetone (blue curve) and acetonitrile (green curve) prepared samples. Dashed lines refer to FTO substrates, solid lines to the corresponding behavior for silicon substrates. (d-f) corresponding XPS analysis of the carbon C 1s signal [202].

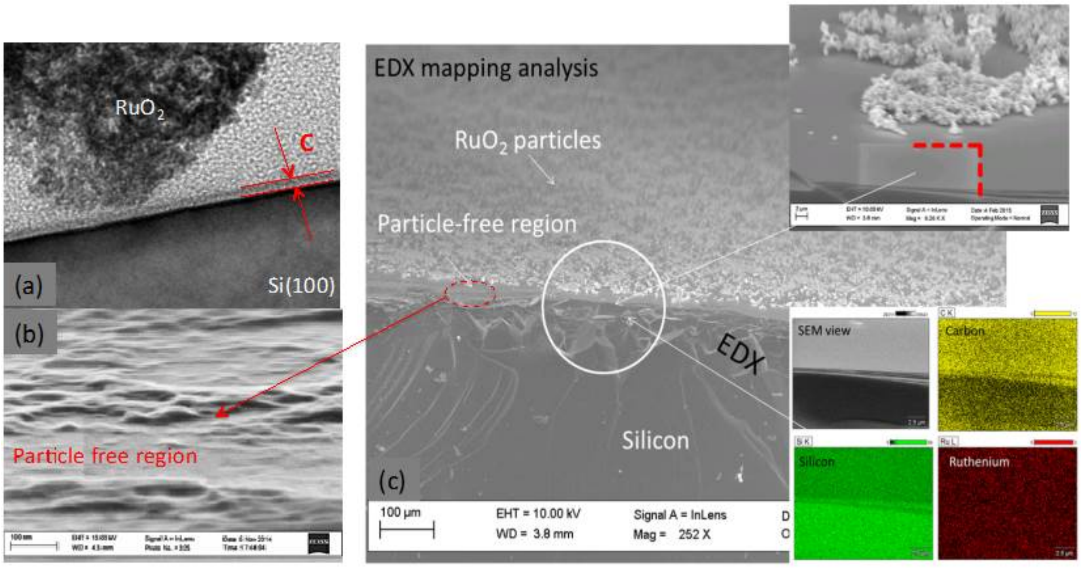

Figure 5.38: (a) TEM image of Si/Carbon/RuO_2, (b) SEM image of a particle-free region (resolution 100 nm) and (c) EDX mapping of a Si/RuO_2 edge [202].

In order to identify the chemical and electronic composition of the respective interfaces, XPS analysis was carried out (XPS measurements were done by Ch. Hohn at HZB and analyses were done under supervision of Dr. M. Lublow). Results are shown on the right-hand side of Figure 5.37(d-f). Deconvolution of the XPS Ru 2p/ C 1s signal for ethanol-prepared samples reveals that the interface formed between H- terminated silicon and the RuO_2 particles shows mainly sp^3 and sp^2-carbon [202]. It shows furthermore contributions of C-OH and C=O bonds. In contrast, acetone and acetonitrile-prepared samples do not show any sp^2-carbon.

Figure 5.38(a) shows a TEM cross section image of an ethanol-prepared sample. A weak but visible contrast between the thin (~3-4 nm) very smooth top-surface layer and the carbon-containing glue (used for preparation for cross-sectional TEM analysis) points to formation of a homogeneous film between the silicon support and the RuO_2 particles. Figure 5.38 (b) shows an SEM image recorded at a tilt angle of the detector with respect to the surface normal by 30°. It can be seen that some parts of the surface are covered by RuO_2 particles. A cross-sectional sample was prepared and analyzed for three hours by EDX surface mapping. Upon cutting and breaking of the sample, particles near the edge came off by tensile stress forces exerted on the support. Thereby, a particle-free region was exposed. There, and also between the particles, the microscopic probe reaches the silicon surface and its interface. A clear contrast in both, the carbon and the Si signal was obtained suggesting a homogeneous organic interfacial region.

5.2.3.1 RuO_2/Si: formation principles

In order to gain insight into the actual structure of this interfacial region, several model experiments were carried out. The results, to be discussed in the following, suggest the presence of a Si/SiO_2 junction with an adjacent organic film encompassing two distinguishable sub-layers with different electronic and electrochemical properties. According to the XPS results for sample prepared in ethanol (Figure 5.37 (d)), a scheme of this entire structure is presented in Figure 5.39. It depicts in (a) the entire device structure comprising the n-Si(100) substrate, an interfacial silicon dioxide layer and the organic junction containing carbon-sp^3 and carbon-sp^2 sub-layers. Grey spheres indicate RuO_2 nanoparticles at the top as prepared by electrophoretic deposition. In (b), the respective interfaces and their functions within the device structure are shown. The device and the interfaces were individually analyzed by the indicated electrochemical reactions: evolution of oxygen in acidic electrolytes (H_2SO_4 0.5 M) and conversion to electrical energy using an I^-/I_3^- redox couple (section 5.2.3.4). These individual interfaces result from the combined electrochemical and electrophoretic reactions under cathodic conditions as identified by the following step-wise analysis [202].

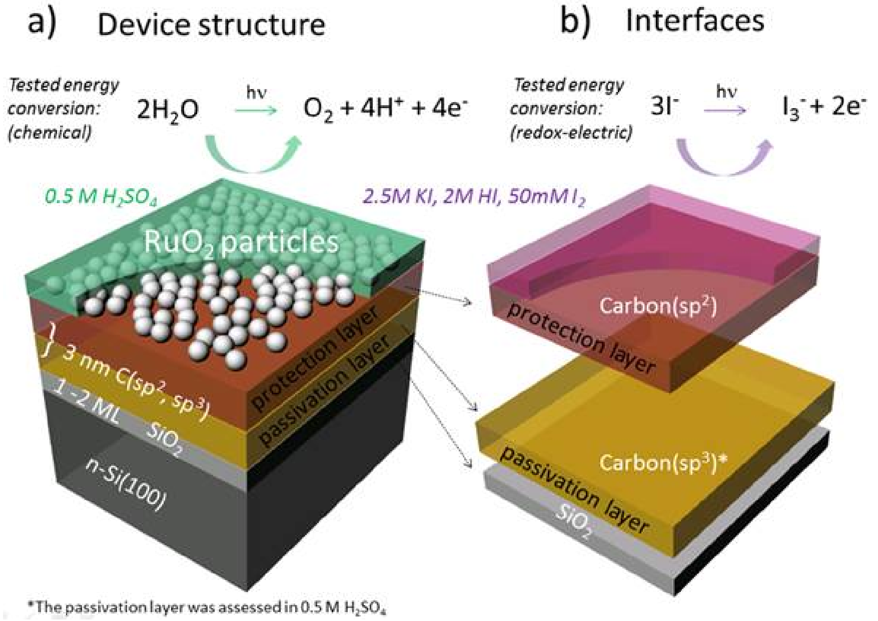
a) Device structure
b) Interfaces
Tested energy conversion: (chemical)
$2H_2O \xrightarrow{h\nu} O_2 + 4H^+ + 4e^-$
Tested energy conversion: (redox-electric)
$3I^- \xrightarrow{h\nu} I_3^- + 2e^-$
0.5 M H_2SO_4
2.5M KI, 2M HI, 50mM I_2
RuO_2 particles
3 nm C(sp^2, sp^3)
1-2 ML SiO_2
n-Si(100)
protection layer
passivation layer
Carbon(sp^2)
protection layer
Carbon(sp^3)*
passivation layer
SiO_2

*The passivation layer was assessed in 0.5 M H_2SO_4

Figure 5.39: Device scheme and interfaces of Si/SiO_2/Carbon(sp^3)/Carbon (sp^2)/RuO_2.

Step I: Role of iodine

Firstly, an H-terminated n-Si electrode was exposed to pure ethanol for 15 min at -10 V. Secondly, another H-terminated n-Si sample was exposed to a mixture of ethanol and iodine under the same electrochemical conditions. The photocurrent-voltage behavior of these samples is shown in Figure 5.40 (a) and (b). The results show that while cathodic polarization of silicon in ethanol yields a low open circuit photovoltage (140 mV) and no surface protection in 0.5 M H_2SO_4 (fast degradation), the corresponding treatment in ethanol-iodine results in a high photovoltage of 550 mV and initial surface protection during anodic cyclovoltammetry. It is thereby demonstrated that the combination of ethanol with iodine introduces high-quality electronic surface passivation to the silicon surface, i.e. the surface is defect-free and the surface recombination velocity, the most crucial parameter for photoelectrode applications, is extremely low. XPS analysis, obtained for the sample prepared in the mixture of ethanol and iodine, is shown in Figure 5.41 for C 1s (a), Si 2p (b) and I 3d (c). Deconvolution of the XPS C 1s signal (Figure 5.41(a)) shows three binding energies at 287.4 eV, 286.8 eV and 285.55 eV. Please note that carbon Auger analysis was added as inset to serve as comparative reference signal for corresponding results obtained for samples with deposited RuO_2. Deconvolution of the C 1s signal in Figure 5.41(a) suggests the presence of sp^3-carbon with C-O and

C-OH bonds. The Si 2p signal in Figure 5.41(b) shows that only minute amounts of SiO_2 is formed during preparation. Distinctive amounts of I 3d, however, are observed. Iodine appears in three different bonding states. The largest contribution near 621 eV (3d 5/2) has to be attributed to molecular iodine. Two further levels at 619.5 and near 620 eV are detected to be assigned to reaction of iodine with the organic solvent. It is therefore assumed that coupling of ethyl groups to the silicon surface occurs during the electrochemical treatment at -10 V and that this surface conditioning stabilizes the sample initially under anodic conditions in H_2SO_4 at pH0.3. This sp^3-carbon layer forms the organic interface directly adjacent to the Si/SiO_2 interface depicted in the scheme of Figure 5.39(b).

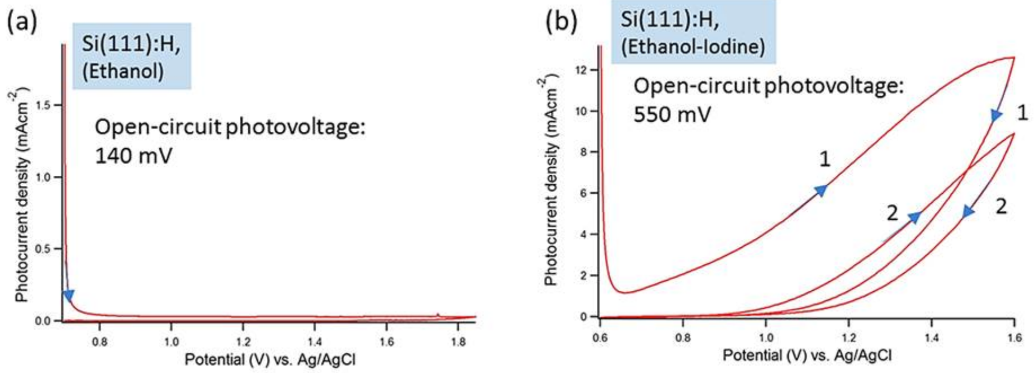

Figure 5.40: Photocurrent-voltage behavior of Si(100) in 0.5 M H_2SO_4 after electrochemical surface conditioning in ethanol and ethanol-iodine, respectively.

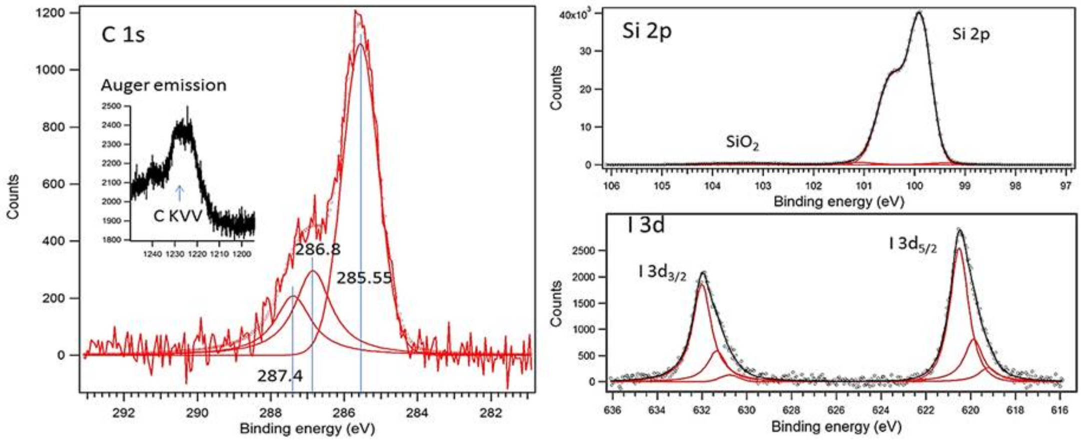

Figure 5.41: XPS C 1s, Si 2p and I 3d signals of Si(100) after electrochemical surface conditioning in ethanol-iodine [202].

Figure 5.42 shows UPS analysis of the cut-off region of secondary electrons of H-terminated (a) and ethanol-iodine-prepared silicon (b), respectively. After etching in HF (50%), the hydrogen-terminated surface shows two work-function features in the cut-off region: the higher value of 4.15 eV is indicative for the position of the Fermi-level of n-doped Si. The low-energy shoulder is assigned to partial surface coverage of the sample causing a surface dipole with reduced work function energy. After conditioning in ethanol-iodine, a reverse dipole is observed by ultra-violet photoelectron spectroscopy, pointing to partial coverage of the surface with a different terminal group, decreasing thereby the silicon work function of 4.3 eV to about 4.1 eV.

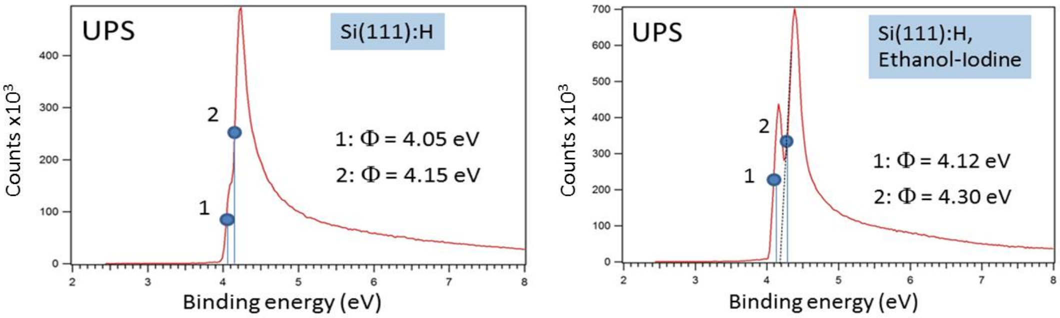

Figure 5.42: UPS analysis of the cut-off region of secondary electrons of (a) H-terminated silicon and (b) ethanol-iodine-prepared silicon.

The bonding to ethyl groups to the silicon surface under the applied electrochemical conditions is conceived as follows: remnant water in the ethanol solvent, introduces slightly acidic conditions by hydroiodic acid formed due to disproportionation of iodine into iodide, hypoiodite and protons. Under cathodic polarization (-10 V versus counter electrode), ethanol molecules are considered to undergo substitution reactions to form ethyl iodide: $CH_3 - CH_2 - OH + HI \longrightarrow CH_3 - CH_2 - I + H_2O$, activating thereby the molecules for reaction with the H-terminated silicon surface.

Step II: Role of RuO_2

In order to identify the role of RuO_2 upon formation of the organic interface, a corresponding XPS analysis was carried out after EPD-deposition of RuO_2 onto silicon. As an XPS reference, RuO_2 powder was physically adsorbed from a water solution, i.e. the powder was neither subject to electrochemical processing nor in contact with an organic solvent. The results are shown in Figure 5.43(a/b). It should be noted that XPS carbon-analysis of the surface area in the presence of RuO_2 requires particularly careful deconvolution of the binding energy range between 270 and 290 eV: in this range, the respective signals of the Ru 3d and the C 1s level are superimposed on each other. The individual components are therefore separately depicted in the figure. Furthermore, the complex surface chemistry of ruthenium oxide gives rise to satellite structures, whose origin is still debated. In order to facilitate disentanglement of the respective contributions of carbon and ruthenium, also Auger C KVV and Ru MNN emission signals were measured and presented as insets in the corresponding figures. These signals appear at distinguishable energies and allow assessing the relative strength of carbon and ruthenium contributions, respectively. Analysis of the C 1s core-level signal demonstrates that after electrophoretic deposition, carbon appears in sp^2-hybridization (at 284.05 eV in Figure 5.43 (b)). No corresponding signal is observed for RuO_2 physically adsorbed on silicon (Figure 5.43(a)). Additionally, carboxyl (C-OH) and carbonyl groups (C=O) are present as detected by the corresponding signals at 286.85 and 288.0 eV, respectively. The surface of the sample was covered by about 50% with RuO_2 nanoparticles. UPS measurements in Figure 5.43 show that the measured work function increases after electrophoretic deposition from about 5 eV (corresponding to the work function of RuO_2) to 5.7 eV.

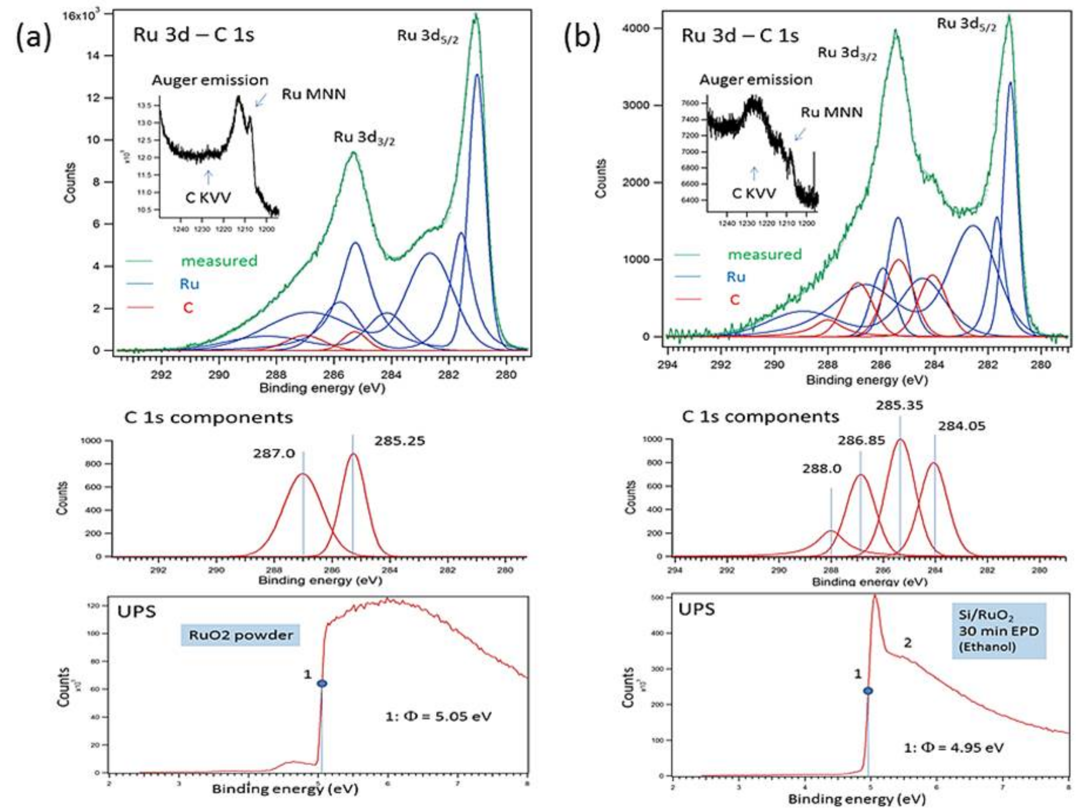

Figure 5.43: XPS analysis of the Ru 3d and C 1s core-level signals of (a) RuO_2 powder after physical adsorption from aqueous particle suspensions onto silicon and (b) RuO_2 deposited for 30 min onto silicon from ethanol-iodine containing suspensions. The C 1s deconvoluted signals and UPS analysis of the cut-off region of secondary electrons of each case are shown below [202].

Figure 5.44 shows the XPS analysis of the Ru 3d and C 1s core-level signals of Si/RuO_2 after extended deposition for 60 min onto silicon from ethanol-iodine containing suspensions. With longer deposition times, the silicon surface is increasingly covered by RuO_2 (the coverage increases to about 80%). This increase can also be deduced from the respective signal intensities of the carbon and ruthenium Auger emission lines shown as insets. Despite lower photoelectron emission strength of the C 1s electrons, carbon is again clearly detected in sp^2-hybridization at 284.2 eV. The respective ratios of C-H, C-OH and C=O have slightly changed in comparison to Figure 5.43(b). Furthermore, a low contribution of metallic ruthenium (about 0.1%) suggests the involvement of the catalyst in reductive electrochemical reactions which lead to the observed sp^2-rich organic interface. It is this sp^2-containing interface that forms the second sub-layer within the organic film depicted in Figure 5.39(b).

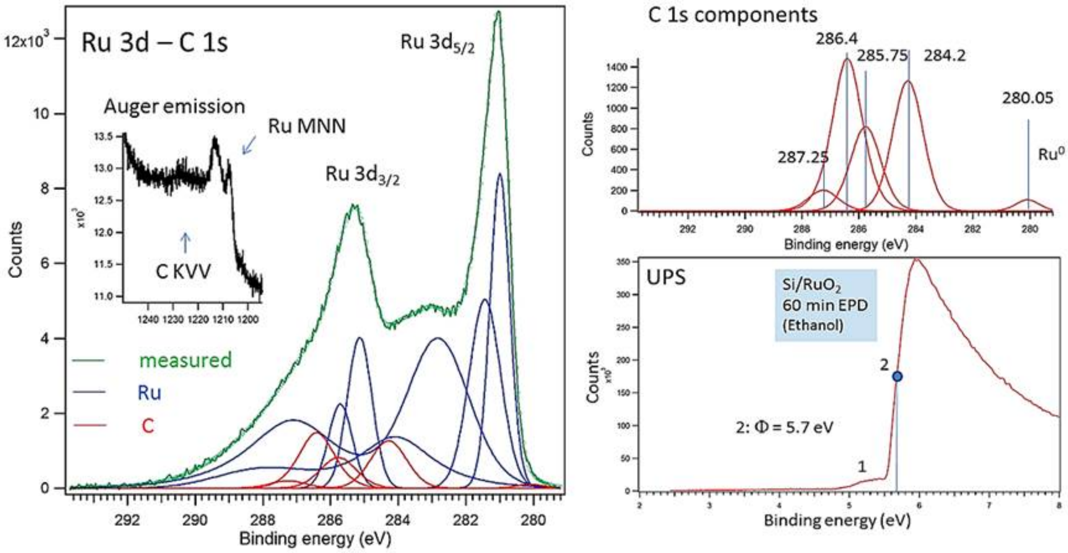

Figure 5.44: XPS analysis of the Ru 3d and C 1s core-level signals and UPS analysis of RuO_2 deposited for 60 min onto silicon from ethanol-iodine containing suspensions [202].

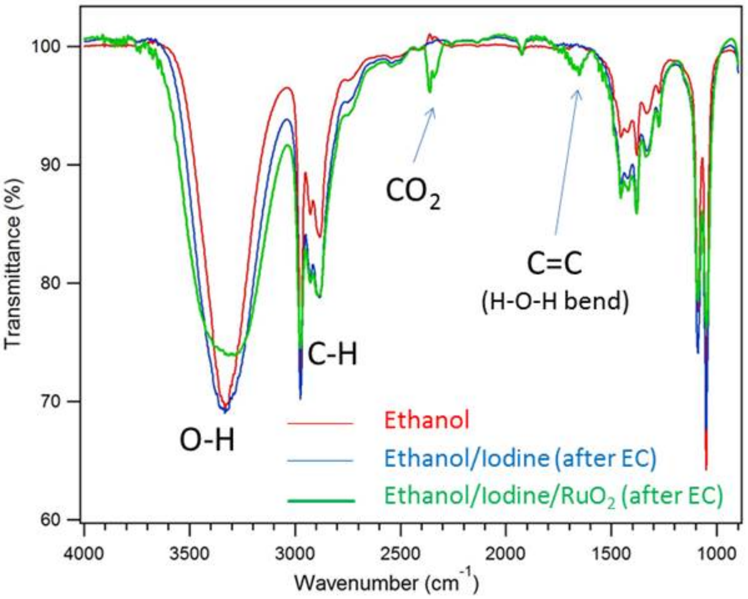

Figure 5.45: FTIR analysis of the used solutions, ethanol (red), ethanol/iodine after electrochemistry (blue) and ethanol/iodine/RuO_2 after electrochemistry (green).

As independent further analysis method, FTIR spectra were recorded for the three different solutions after deposition or surface conditioning, respectively. The spectra are shown in Figure 5.45 for ethanol (red curve), mixture of ethanol/iodine (blue curve) and mixture of ethanol/iodine/RuO_2 (green curve). Surface conditioning of silicon in ethanol-iodine containing solutions results in only small changes in comparison with pure ethanol [202]. The OH-vibration signal near 3400 cm^{-1} appears slightly broadened and may give an indication for a different OH-containing species in solution, presumably H_2O produced by ethanol dehydration. After deposition from suspensions of RuO_2 powder in ethanol-iodine, FTIR proves the presence of C=C double bonds (signal near 1600 cm^{-1}),

CO_2 (signal near 2400 cm^{-1}) and a considerably broadened OH-vibration, indicative for a strong increase of water concentration. The C=O bonds are thought to result from a different reaction mechanism that may involve intermediate formation of acetaldehyde. In Figure 5.46 analysis of the I 3d signal is presented for samples prepared in ethanol for 30 min (a), for 60 min (b), acetone (c) and acetonitrile (d). A very low I 3d signal is detected after deposition from ethanol-iodine solutions. In the case of acetone and acetonitrile, the large signals near 620 and 619 eV indicate high reactivity of iodine towards the organic solvent molecules.

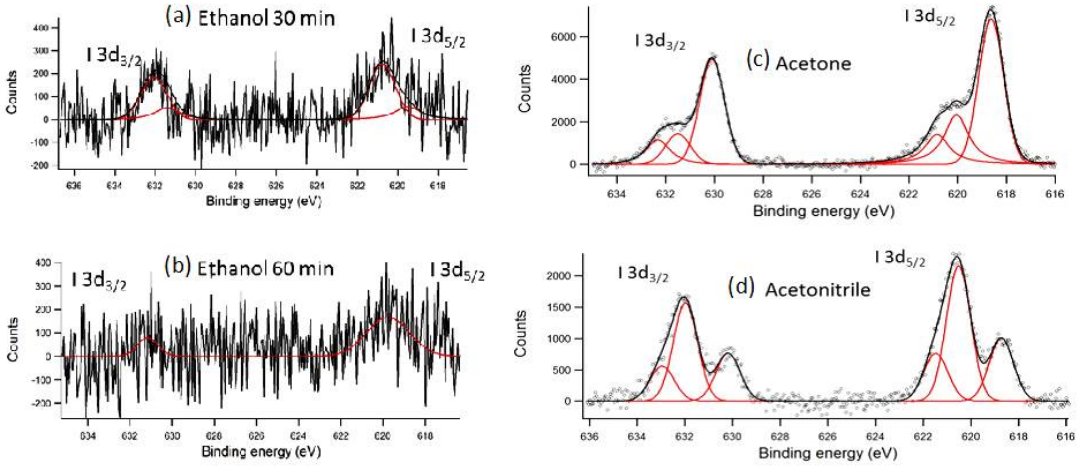

Figure 5.46: XPS Iodine I 3d analysis after deposition from ethanol- (a/b), acetone- (c) and acetonitrile- (d) iodine suspensions of RuO_2.

Figure 5.47 shows the XRD spectrum of the sample prepared in a RuO_2 /ethanol/iodine mixture. The blue curve shows the XRD spectrum of an as-prepared sample and the red curve shows the corresponding spectrum after annealing of the sample at 580° C in air. In the upper image of Figure 5.47, lines to be attributed to the organic interface are labeled as 1 and 2, respectively. A pronounced peak near 21° is accompanied by a weaker structure around 44°. The reflection pattern at 22° lies between those measured for polyethylene and doped polyacetylene, i.e. the two potential building blocks of the polymeric material [203-204]. After transformation to CO_2 by annealing in air, these lines are not visible anymore (lower images 5.47). In contrast to (undoped) polyacetylene, however, the d-spacing is larger and the main XRD line is shifted by about 2° towards lower angles.

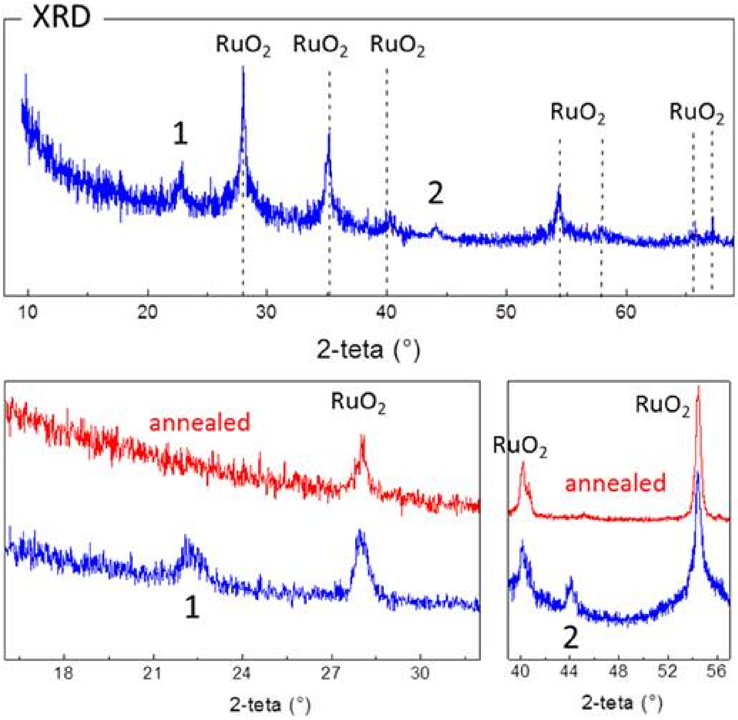

Figure 5.47: XRD analysis of Si/RuO_2, prepared from ethanol-iodine containing suspensions before (blue) and after annealing (red).

Based on these observations, the mechanism that leads to the formation of the protection layer is assumed to follow two main reaction routes[202]:

1. in the presence of RuO_2, dehydration of ethanol proceeds at an elevated rate according to FTIR analysis. Coupling of ethyl iodide ions results in a $(CH_2)_n$ network with substitutions of hydrogen for iodine ($-H_2C-HI-CH_2-$). The process follows likely a RuO_2-surface-mediated pathway as recently reported for ethyl iodides on Au-surfaces where ethyl iodide bonds to surface oxygen by release of iodine from C-I bonds [203].

2. Under the applied reducing conditions, formation of an ethoxide is supported, i.e. ethanol in the presence of RuO_2 and under cathodic conditions forms the anion $CH_3 - CH_2 - O^-$. It should be noted that this reaction is the cathodic counterpart to alkoxide formation by anodic dissolution of metallic species. Ethoxide acts as a strong base which suppresses, by steric hindrance, substitution reactions and favors E2 elimination (dehydrohalogenation) to produce carbon double bonds within the $(CH_2)_n$ network at sites where hydrogen is substituted by iodine: $I^- + -CH_2 - CHI^- \longrightarrow -HC = CH - +HI + I^-$. Consequently, and in agreement with XPS analysis, iodine is removed from the network by this process (Figure 5.46). Finally, formation of acetaldehyde introduces C=O bonds which connect to the layer as terminal groups. These bonds, and remnant C-OH bonds, are stabilizing the carbon atoms against electrophilic attack in the acidic solution. In fact, a dehydrohalogenation process of the alcohol appears essential for carbon-sp^2 formation: corresponding experiments with acetone and acetonitrile did not show any significant formation of carbon double bonds (Figure 5.37 C 1s signals)

while iodine is detected in high concentrations (Figure 5.46(c/d)). Accordingly, the resulting photoelectrochemical performance as water splitting photoelectrode remained insufficient in these cases (Figure 5.37(b/c)). In order to account for the assumed p-type conductivity of the organic interface, terminal oxygen-containing groups, withdrawing electrons from carbon, may be identified as possible cause.

5.2.3.2 Characterization of the RuO_2/Si photoanode

The photoelectrochemical performance for light-induced splitting of water at pH0.3 (0.5 M H_2SO_4) is depicted in Figure 5.48 (a). The red curve is related to a surface coverage of RuO_2 by about 80% when prepared from RuO_2/ethanol/iodine solution. The high open-circuit photovoltage (400 mV) results in a pronounced shift of the photocurrent onset with respect to the thermodynamic potential for water splitting (1.23 V RHE). Photocurrent densities near 10 $mAcm^{-2}$ are reached at this potential, i.e. without overpotential. Auger analysis (shown as inset in figure 5.55(a)) shows predominantly ruthenium MNN emission (near 1210 eV), confirming the high coverage with the catalyst. The carbon signal is low due to high coverage of RuO_2 on the surface.

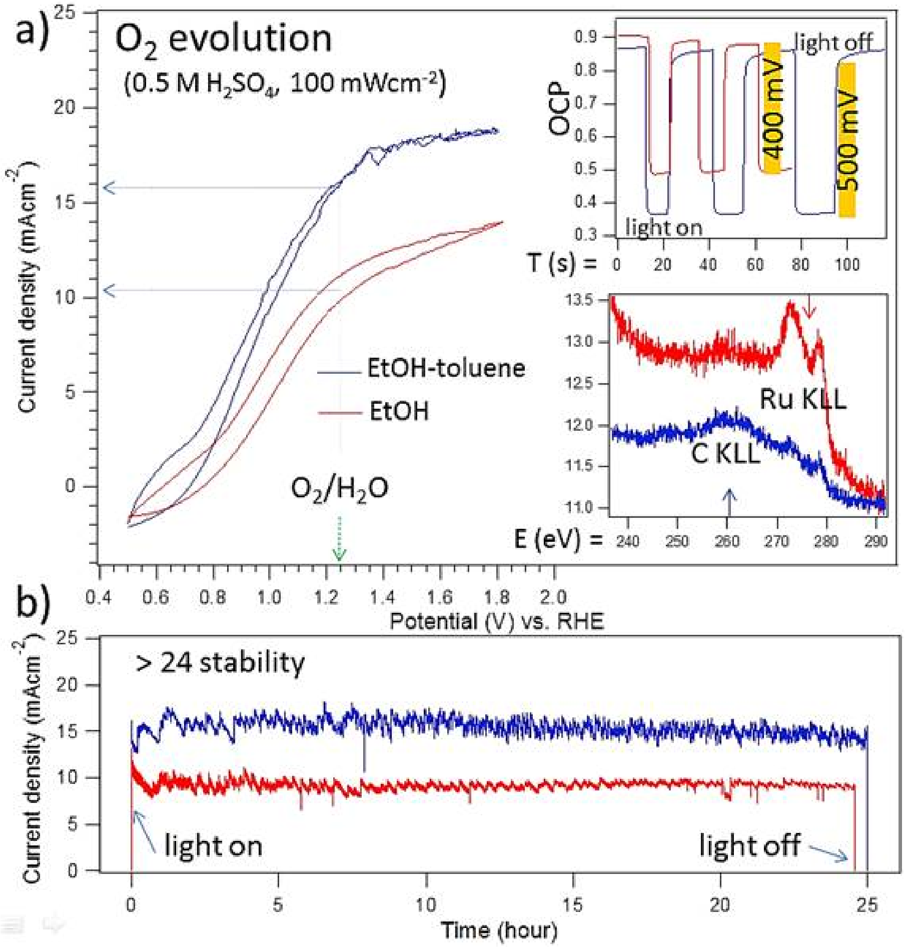

Figure 5.48: Operation of the Si/SiO_2/RuO_2 electrode for photo-assisted water splitting. (a) The photocurrent-voltage behavior is shown for two different distributions of RuO_2 particles. (b) Constant potential measurements in 0.5M H_2SO_4 under illumination (AM1.5)[202].

In order to increase the light absorption by silicon substrate, a non-polar solvent, toluene, was added to the solution. The surface morphology thereby changes such that instead of a homogeneously distribution of RuO_2 particles, RuO_2 clusters are formed (SEM picture in Figure 5.49). Thereby, larger areas of the silicon substrate are accessible to illumination by the used white-light source.

These results are also confirmed by XPS analysis of the Ru 3d and C 1s signals of the sample (Figure 5.50). XPS analysis also confirmed the lower coverage of the surface by RuO_2 particles. Deconvolution of the XPS Ru 3d, C 1s core-level signals and UPS measurements of Si/RuO_2 after deposition for 30 min onto silicon from ethanol-toluene-iodine containing suspensions is shown in Figure 5.50. Comparison of the C 1s signals measured for samples prepared from ethanol-iodine (Figure 5.43(b)) and from ethanol-toluene-iodine show that the carbon $sp^2 : sp^3$ ratio has decreased. This effect is attributed to a decrease in dehydrogenation reactions caused by the more scattered distribution of the catalytic RuO_2 particles (SEM image in Figure 5.49) [202]. The UPS cut-off region (Figure 5.50)shows similar features as observed after preparation in ethanol-iodine (without toluene) but the measured work function has decreased to 4.9 eV.

This improved light-management with RuO_2 cluster formation, leads consequently to a higher open-circuit photovoltage, increased photocurrent densities at the water splitting potential and finally to higher saturation photocurrent densities (blue curve in Figure 5.48(a)). It should be noted that the open-circuit photovoltage of 500 mV is close to corresponding value after surface alkylation from ethanol/iodine solutions as described above. Auger analysis (blue curve in the inset) confirms a larger carbon emission at 1225 eV, confirming higher exposure of the carbon-covered interface to the electrolyte. SEM surface analysis (images in Figure 5.49) confirms that addition of toluene results in particle aggregation with an overall more scattered distribution. Thereby, light reaches the silicon interface more easily. Corresponding IPCE measurements confirm the increased generation of electron-hole pairs under illumination of the sample prepared in the mixture of ethanol/toluene/idonine. Figure 5.49 shows the comparative surface and IPCE analysis of Si/RuO_2 after deposition from ethanol-iodine containing suspensions with (red), without toluene addition (blue) and of bare Si (black). The analysis shows that the sample with lower coverage reached 40% efficiency and with higher coverage only 20%. For comparison, the immediate degradation of bare silicon is depicted as black curve. In Figure 5.48(b), finally, the photocurrent behavior during 24 (25) hours of operation at a constant potential of 1.1 V (RHE) is depicted for ethanol and ethanol-toluene prepared samples. Both preparation routes result in stable operation during this period of time and maintain high photocurrent densities. The samples thereby greatly surpass reported stabilities of organic protection schemes employing chemical surface alkylation or graphene layers.[77]

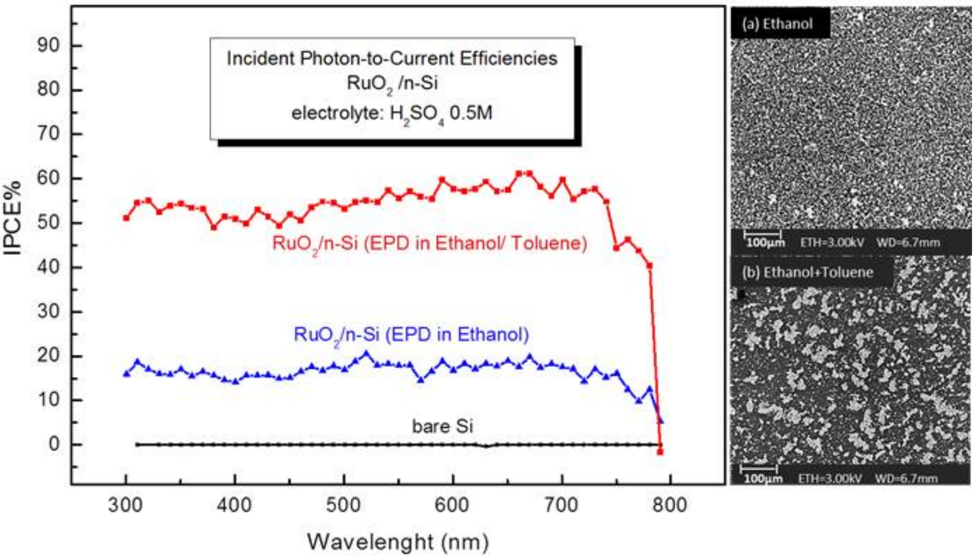

Figure 5.49: Comparative surface and IPCE analysis of Si/RuO_2 after deposition from ethanol-iodine containing suspensions with (red) and without toluene addition (blue). SEM surface analysis (upper images) confirms that addition of toluene results in particle aggregation with an overall more scattered distribution.

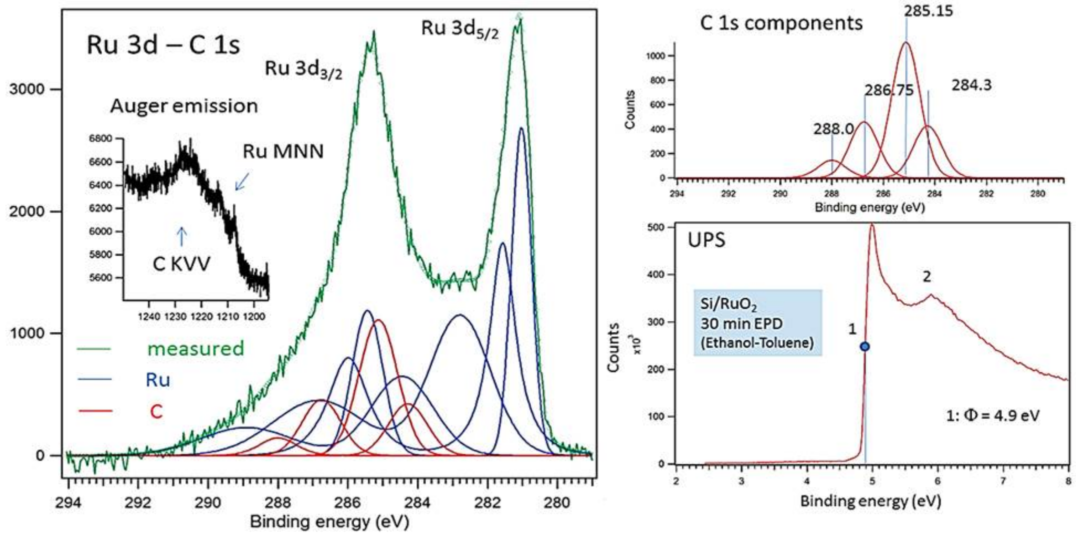

Figure 5.50: XPS analysis of the Ru 3d and C 1s core-level signals of Si/RuO_2 after deposition for 30 min onto silicon from ethanol-toluene-iodine containing suspensions [202].

It should be noted, however, that further decrease of the RuO_2 surface coverage increases the risk for photodegradation. This observation suggests that carbon-sp^2 formation requires a sufficient spatial distribution of the catalyst and a sufficiently high catalytic surface area. Otherwise diffusion of reaction intermediates toward the silicon surface is limited, inhibiting thereby pinhole free growth of the protection layer.

The scheme for the RuO_2-catalyzed formation of an organic interface is depicted in figure 5.51. Red circular areas indicate the spatial distribution of reaction intermediates produced in the presence of the RuO_2 catalyst. Aggregations of particles consequently result in wider radii of the circular areas. It is assumed that, for successful protection of the silicon surface, these areas have to overlap in order to achieve a nearly pin-hole free surface layer. The use of ethanol-toluene mixtures allows more scattered distribution of particle clusters due to the wider range of diffusion of reaction intermediates.

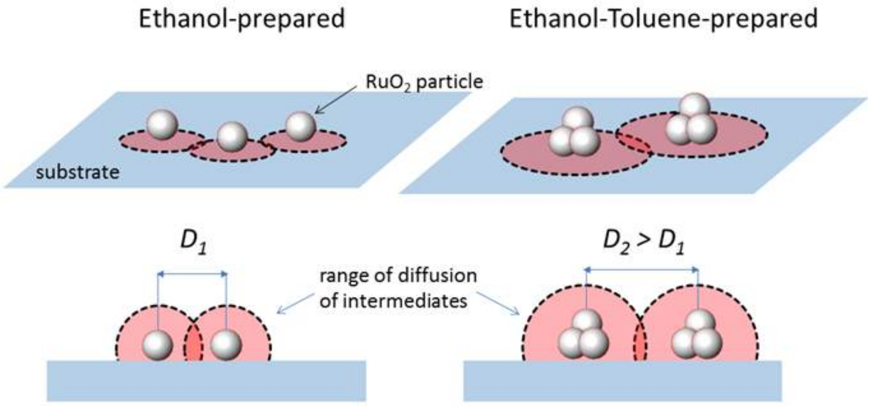
Ethanol-prepared
Ethanol-Toluene-prepared
RuO_2 particle
substrate
D_1
$D_2 > D_1$
range of diffusion of intermediates

Figure 5.51: Scheme for the RuO_2-catalyzed formation of an organic interface.

Figure 5.52 shows differential electrochemical mass spectroscopy measurements (DEMS) for RuO_2/n-Si under illumination (AM1.5). The blue and black curves show the C-V behavior and the O_2 mass signals respectively. It is proven that oxygen evolution is commencing before the redox potential (at 1053 mV vs. RHE). The difference in the onset potential in these measurements and figure 5.48 is due to the potential drop across the membrane in the DEMS setup during the measurement. This membrane is in close contact to the sample, limiting thereby mass transport to the sample and causing an additional overpotential.

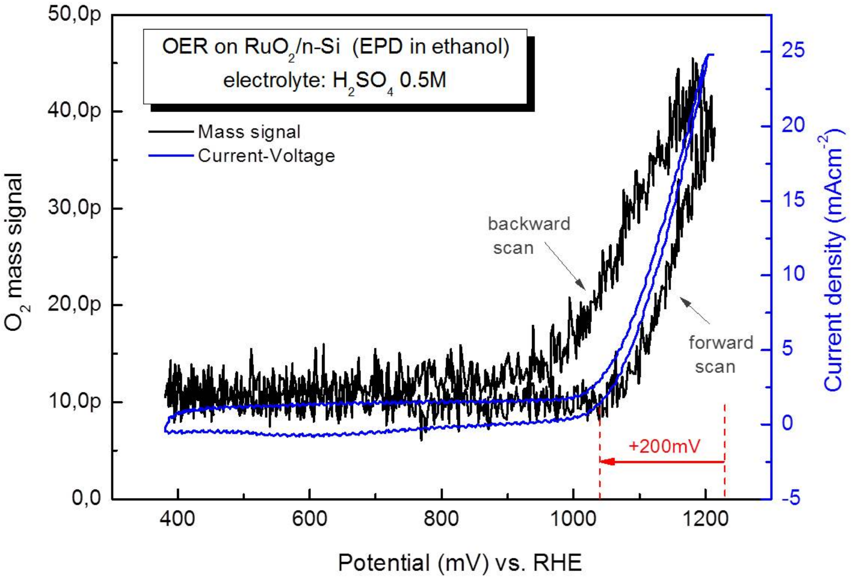

Figure 5.52: Differential electrochemical mass spectroscopy (DEMS) measurements for O_2 evolution on RuO_2/ n-Si photoanode, electrolyte H_2SO_4 0.5 M.

5.2.3.3 pH dependent performance of the RuO_2/n-Si photoanodes

The performance of the RuO_2/n-Si photoanode was tested in different electrolytes, KOH pH14 (blue curve), Kpi pH7 (green curve) and compared with the current-voltage behavior of the photoanode in acidic electrolyte (H_2SO_4 pH0.3 red curve). Figure 5.53 (a) shows the current-voltage behavior of the photoanode under illumination (AM1.5) and in a three-electrode configuration with Ag/AgCl reference electrode. In KOH the current density reaches 7 $mAcm^{-2}$ at the redox potential and in the KPi electrolyte the current reaches 1.7 $mAcm^{-2}$. At pH7, due to the low conductivity of the electrolytes, the resistivity is higher. Therefore, the current increases very slowly. Figure 5.53(b) shows the corresponding stability assessment at a constant potential for the three pH values. The photoanode proves stability from neutral to acidic electrolytes. It has a high stability (25 h) in acidic electrolytes (red curve) and moderate stability for around 5 h at pH7 (green curve). The stability of the sample at pH14 (blue curve) is shown for two cases: freshly prepared (blue dashed line) and after operation at pH0.3 for several hours (blue solid curve). As demonstrated by the respective curves, the rate of degradation depends on the history of the sample: the freshly prepared sample degrades fast upon exposure to the electrolyte at anodic potentials. A sample pre-conditioned (for 15 hours) in acidic electrolytes shows short-term stability for about one hour. The greater susceptibility to degradation in alkaline solutions is attributed to nucleophilic attack of carbon in the organic layer.

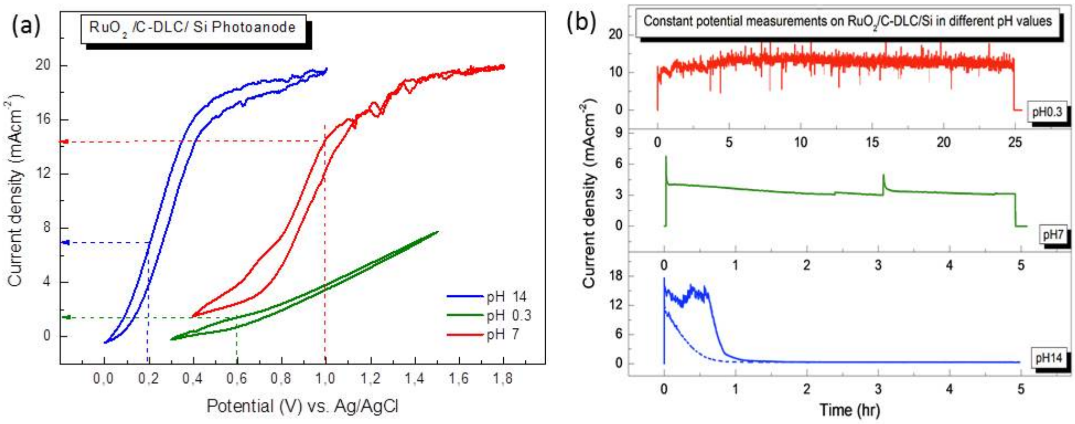

Figure 5.53: (a) current-voltage behavior of RuO_2/Si photoanode in H_2SO_4 (red), Kpi pH7 (green) and KOH pH14 (blue). (b) Constant potential measurements of the photoanodes in the corresponding electrolytes.

5.2.3.4 Photoelectrochemical solar cell application

The entire device structure, as shown in Fig. 5.39, operates efficiently for solar-driven evolution of oxygen. RuO_2 particles withstand mechanical stress forces upon oxygen gas evolution and cover also after 24 hours of operation the entire silicon surface area. In contact with an I^-/I_3^- electrolyte, however, the RuO_2 surface layer is easily removed, exposing thereby the top carbon surface to the solution. This effect provides a unique opportunity to characterize the electrochemical properties of this film individually. Figure 5.54 summarizes the behavior of the heterojunction in contact with the I^-/I_3^- redox couple after removal of RuO_2. The incident light excites the semiconductor electrode and photogenerated electrons and holes are separated in the space charge region. Electrons leave the silicon and travel to the Pt (counter electrode) to reduce I_3^- and generated holes travel to the surface of Si and oxidize I^- to I_3^-. Here, solar energy is converted to electrical energy by the process of oxidation of I^- to I_3^- [206-207]. Data shown in Fig. 5.54(a) were measured in a two-electrode arrangement vs Pt-counter electrode, and are indicated with respect to the measured redox potential (0.35 V vs. RHE).

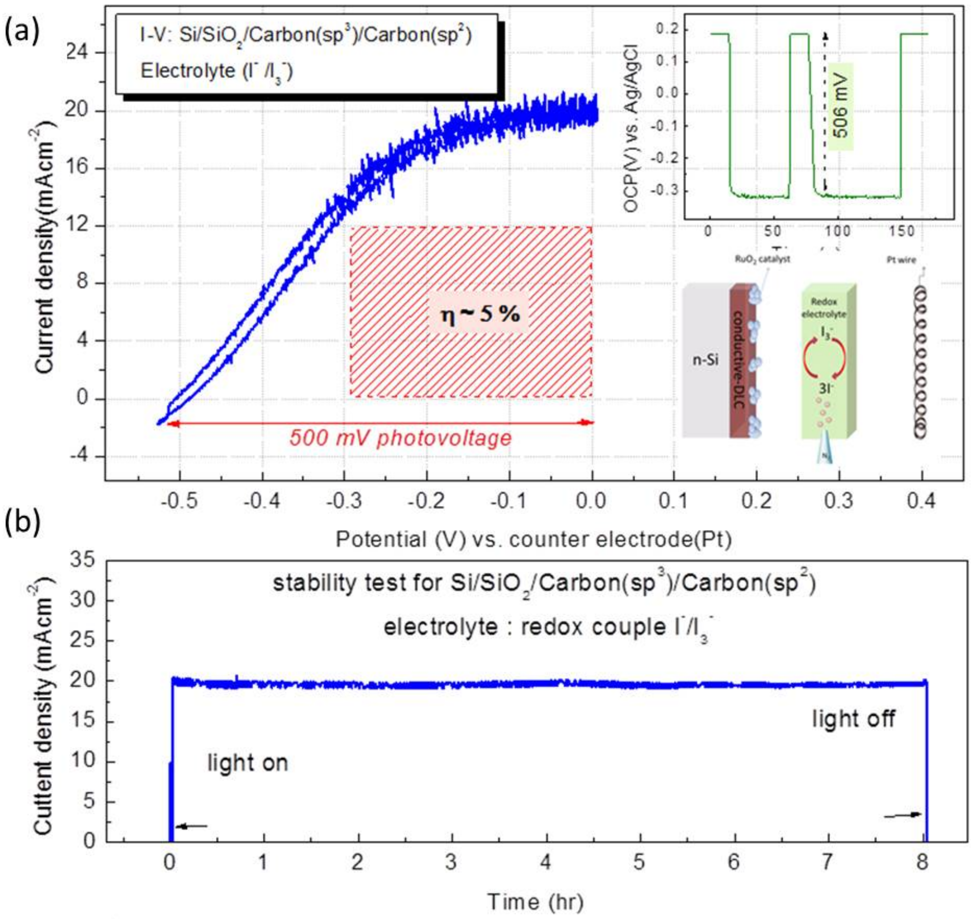

Figure 5.54: Operation of the $Si/SiO_2/RuO_2$ electrode as photoelectrochemical solar cell: In (a), two-electrode measurements in a iodide/triiodide electrolyte are shown using a Pt-counter electrode. The sensitive electrolyte was purged by nitrogen during both current-voltage cycling and long-time assessment of the short-circuit photocurrent (b).

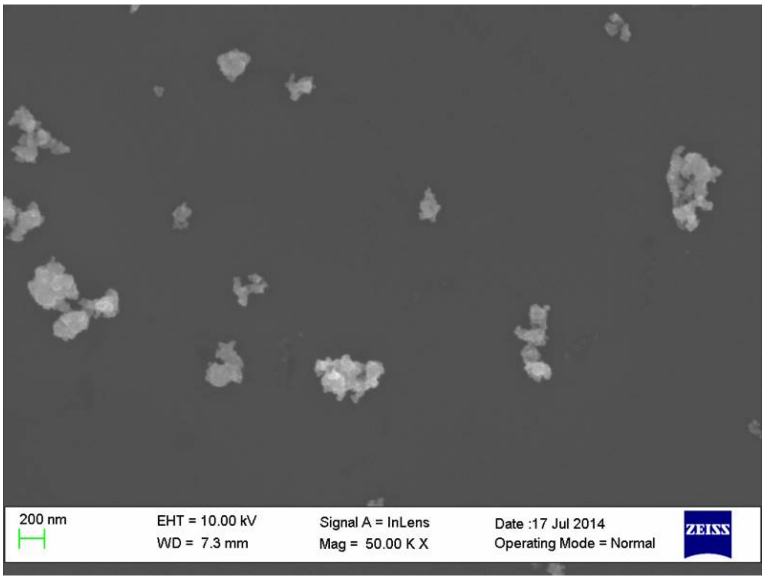

Figure 5.55: SEM surface analysis of the Si photoelectrochemical solar cell.

Upon operation in the iodide/triiodide electrolyte, most of the RuO_2 particles are removed from the surface. Only scattered small aggregations are still visible(Figure 5.55). The stable and efficient operation of the cell, after removal of most of the RuO_2 particles, is attributed to the pronounced hole-conductivity of the Carbon(sp^3)/ Carbon(sp^2) junction.

The photocurrent-voltage behavior indicates that also in this case high open-circuit photovolategs of 500 mV are reached. Since our standard electrochemical cell was used, a large volume of the (red colored) I^-/I_3^- electrolyte was required, thereby considerably attenuating the incoming light. Consequently, short-circuit photocurrent densities were limited to about 20 $mAcm^{-2}$. As Figure 5.54(b) shows even in this photovoltaic mode, extended operation is realized without loss in performance (8 hours) and the results demonstrate the good conduction properties for holes across the about 3-4 nm thick organic heterointerface. This good p-type conductivity is attributed to the presence of C=O and C-OH terminal groups with their electron-withdrawing properties. Effects by iodine incorporation, as observed for iodine-doped polyethylene, appear of minor importance due to the very low signal strength of corresponding XPS I 3d signals. The developed hybrid heterojunction allows therefore for efficient and stable operation in both, the photovoltaic and the photoelectrocatalytic (water splitting) solar energy conversion mode. By combining interfacial surface alkylation with adjacent carbon-sp^2 protection layers, the derived architecture competes successfully with recent inorganic photoelectrodes and surpasses existing benchmarks of the photovoltage in solar-driven water splitting. The high photovoltages of up to 500 mV are attributed to an inorganic-organic n-p heterojunction where the p-type polymeric protection layer induces a large in-built potential within the silicon surface region.

6 Summary and outlook

1. In the first part of this work, it has been shown for the first time that the device-grade thin film solar cell concept based on p-type chalcopyrite thin film absorbers can be successfully transferred to photoelectrodes for the visible-light driven hydrogen evolution. In order to achieve efficient and stable photocathode devices, new TCO thin films based on photo-resistant Pt-doped $\mathsf{TiO_2}$ were developed as substitute of standard and chemically unstable ZnO window layers. Spray ILGAR deposition was applied to deposit $\mathsf{TiO_2}$ on $\mathsf{Cu(In, Ga)Se_2}$. For increase of the conductivity and catalytic activity of the TCO layer, 5 vol.% Pt was added to the $\mathsf{TiO_2}$ precursor solution. The conductivity of the layers was measured by four-probe-technique and it could be shown that there is a linear correlation between Pt concentration and conductivity of the layer up to 5% loading. Beyond this value, the conductivity decreased due to agglomeration of Pt-nanoparticles. In acidic electrolyte, the most efficient and long-term stable Pt:$\mathsf{TiO_2}$ -$\mathsf{Cu(In, Ga)Se_2}$ heterojunction allowed generation of solar hydrogen under visible light illumination by 1 equivalent sun ($\sim 100\,\mathsf{mWcm^{-2}}$) with an onset potential of about +300 mV with respect to the thermodynamic potential for $\mathsf{H_2}$-evolution (0 V RHE). Furthermore, the stable photocathode devices proved efficient solar hydrogen evolution with an IPCE of about 80 % in the complete visible light range. Photocurrent densities of $\sim 15\mathsf{mAcm^{-2}}$ at the thermodynamic potential for $\mathsf{H_2}$-evolution were achieved. High turn-over-numbers of $\sim 2.5 \times 10^6$ per active site were calculated. Further device improvements are in progress: (i) interface engineering of the Pt:$\mathsf{TiO_2}$-$\mathsf{Cu(In, Ga)Se_2}$ heterojunction by introducing a thin layer of $\mathsf{TiO_2}$ by ALD in order to avoid formation of deleterious metal-semiconductor junctions, (ii) doping of the $\mathsf{TiO_2}$ thin films with earth-abundant elements such as V and Cr as substitutes of cost-extensive Pt, and (iii) the utilization of chalcopyrite thin films with higher band gap energies such as $\mathsf{CuInS_2}$ and $\mathsf{CuGaSe_2}$ in order to increase the built-in driving potential upon contact formation with $\mathsf{TiO_2}$. [183]

2. In the second part of this work, electrophoretic deposition was introduced as a promising method for deposition of presynthesized catalysts on conductive substrates. Fundamental research was performed to elucidate the effect of different organic solvents, used upon EPD, on the device performance. A systematic study was presented to correlate the deposition rates and film structure properties of ZnO:Co and $\mathsf{RuO_2}$ thin films with the electrophoretic mobility and the Zeta potential in different organic solvents. The electrocatalytic activity of these particles on FTO supports was shown to depend on the size of the active surface area of the resulting films. It could be shown that the use of acetonitrile results in a surface morphology with highest active surface area. Consequently, the overpotentials for evolution of oxygen (OER), observed at 1 $\mathsf{mAcm^{-2}}$, could be reduced from 360 mV to 290 mV. Combining ZnO:Co electrocatalysts and low-cost photovoltaic triple-junctions (a-Si), a proof-of-concept could be successfully demonstrated for an efficient modular architecture for generation of solar hydrogen (up to 5% STH and long-term stability for more than 25 hours). [196]

3. $\mathsf{RuO_2}$ as a well-known catalyst for OER was tested instead of ZnO:Co in order to prepare a stable photoanode for acidic electrolytes. An activity-solvent correlation carried out for $\mathsf{RuO_2}$ /FTO proved equivalent results as in the case of ZnO:Co/FTO.

Highest activity in acetonitrile was observed due to the higher surface area while ethanol-prepared samples showed lowest activity, i.e. highest overpotentials. Using n-type silicon as deposition supports, however, the role of the organic solvent greatly differed from corresponding results obtained for ZnO:Co. Samples prepared in acetonitrile and acetone proved to be unstable and showed no photoactivity. Samples prepared in ethanol, in turn, proved unprecedented high photovoltages of 500-550 mV, high saturation photocurrent densities and long-term stability. TEM cross section analysis revealed the formation of an ultra-thin polymeric layer of 3-4 nm thickness which guaranteed the stable operation of the oxidation-sensitive silicon support. XPS analysis, FTIR and Grazing-Incidence X-ray Diffraction investigations were carried out in order to conceive the generation of polymeric protection layers from alcohols in the presence of $\mathsf{RuO_2}$. A complex reaction scheme could be thereby deduced, involving dehydration of the alcohol, formation of terminal aldehyde groups and $\mathsf{sp}^3 - \mathsf{sp}^2$ transformations under electrochemical conditions. The photoanode showed high stability in acidic electrolyte for more than 24 hours. Addition of toluene to the precursor solution finally allowed for improvement of the light-absorbing properties, and photocurrent densities at the redox potential could be increased to 12 mAcm^{-2}. The prospect of future developments is appealing: new reaction schemes, to be developed, may allow to more efficiently synthesizing this novel type of polymer. Further fundamental investigations are expected to provide schemes for doping and for stabilizing of the material also in alkaline media. [202]

7 Appendices

7.1 References

[1] Statistical Review of World Energy 2013, http://www.bp.com / statisticalreview
[2] D. G. Nocera, ChemSusChem 2009, 2, 387-390.
[3] R. van de Krol, "Photoelectrochemical measurements,in Photoelectrochemical Hydrogen Production" (R. van de Krol and M. Grätzel), vol. 102 of Electronic Materials: Science & Technology, ch. 3, pp. 69, 117, Springer US,2012.
[4] J. Petrasch, J. Klaisner, WIREs Energy and Environment 2012, 1, 347-361.
[5] I. Dincer, A. S. Joshi, "Solar based hydrogen production systems" Springer 2013.
[6] S. Z. Baykara, E. Bilgen, Hydrogen energy 1989, 14, 881-891.
[7] R. H. Crabtree, Energy Production and Storage: Inorganic Chemical Strategies for a Warming World; 2010.
[8] K. Maeda, K. Domen, J. Phys. Chem. C 2007, 111(22), 7851.
[9] M. Bledowski,"Visble light-driven photooxidation of water at hybride photoanodes", 2013.
[10] A. Fujishima and K. Honda, B Chem. Soc. Jpn. 1971, 44, 1148- 1150.
[11] A. Fujishima and K. Honda, Nature 1972, 238, 37.
[12] A. Heller, Acc. Chem. Res. 1981, 14, 154-162.
[13] H. J. Lewerenz, C. Heine, K. Skorupska, N. Szabo, T. Hannappel, T. Vo-Dinh, S. A. Campbell, H. W. Klemm, A. G. Munoz, Energy Environ. Sci. 2010, 3, 748-760.
[14] O. Khaselev, A. Bansal and J. A. Turner, Int J Hydrogen Energ, 2001, 26, 127-132.
[15] O. Khaselev and J. A. Turner, Science, 1998, 280, 425-427.
[16] S. Licht, B. Wang, S. Mukerji, T. Soga, M. Umeno and H. Tributsch, J. Phys. Chem. B, 2000, 104(38), 8920-8924.
[17] M. M. May, H. J. Lewerenz, D. Lackner, F. Dimroth, T. Hannappel, Nature Communications 2015, 6, 8286.
[18] S. Y. Reece, J. A. Hamel, K. Sung, T. D. Jarvi1, A. J. Esswein, J. J. H. Pijpers, D. G. Nocera, Science 2011, Vol. 334 no. 6056 pp. 645-648.
[19] F. F. Abdi, L. Han, A. H. M. Smets, M. Zeman, B. Dam, R. van de Krol, Nature Communications 2013, 4, 2195.
[20] E. L. Miller, B. Marsen, D. Paluselli, R. Rocheleau, Electrochemical and Solid-State Letters 2005, 8, A247-A249.
[21] K. Sivula, F. L. Formal, M. Grätzel, ChemSusChem 2011, 4, 432-449.
[22] H. Kaneko, T. Minegishi, K. Domen, Coatings 2015, 5, 293-311.
[23] R. Klenk, J. Klaer, R. Scheer, M. C. Lux-Steiner, I. Luck, N. Meyer, U. Ruhle, Thin Solid Films 2005, 480, 509.
[24] J. Haarstrich, H. Metzner, M. Oertel, C. Ronning, T. Rissom, C. A. Kaufmann, T. Unold, H. W. Schock, J. Windeln, W. Mannstadt, E. Rudigier-Voigt, Sol. Energy Mater. Sol. Cells 2011, 95, 1028-1030.
[25] R. Caballero, C.A. Kaufamnn, V. Efimova, T. Rissom, V. Hoffmann, H. W. Schock, Prog. in Photovolt: Res. Appl. 2013, 21, 30-46.
[26] M. Rusu, S. Wiesner, R. Wurz, S. Lehmann, S. Doka-Yamigno, A. Meeder, D. F. Marron, M. Bar, V. Koteski, H. E. Mahnke, E. Arushanov, J. Beckmann, K. Hohn, W. Fritsch, W. Bohne, P. Schubert-Bischoff, M. Heuken, A. Jager-Waldau, A. Rumberg, Th. Schedel-Niedrig, Sol. Energy Mater. Sol. Cells 2011, 95, 1555-1580.

[27] P. Jackson, D. Hariskos, E. Lotter, S. Paetel, R. Wuerz, R. Menner, W. Wischmann, M. Powalla, Prog. in Photovolt: Res. Appl. 2011, 19, 894-897.
[28] F. Yang, M. Lublow, S. Orthmann, C. Merschjann, T. Tyborski, M. Rusu, S. Kubala, A. Thomas, R. Arrigo, M. HÃďvecker, T. Schedel-Niedrig, ChemSusChem 2012, 5, 1227.
[29] F. Yang, V. Kuznietsov, M. Lublow, C. Merschjann, A. Steigert, J. Klaer, A. Thomas, Th. Schedel-Niedrig, J. Mater. Chem. A 2013, 1, 6407.
[30] D. Yokoyama, T. Minegishi, K. Maeda, M. Katayama, J. Kubota, A. Yamada, M. Konagai, K. Domen, Electrochem. Commun. 2010, 12, 6, 851-853.
[31] B. Neumann, P. Bogdanoff, H. Tributsch, J. Phys. Chem.C 2009, 113(49), 20980-20989.
[32] T. J. Jacobsson, C Platzer-Björkman, M. Edoff, T. Edvinsson, Int. J. Hyd. Ener. 2013, 38, 15027-15035.
[33] M. W. Kanan, D. G. Nocera, Science 2008, 321, 1072-1075.
[34] Y. Surendranath, M. Dinca, D. G. Nocera, J. Am. Chem. Soc. 2009, 131, 2615-2620.
[35] N. D. Morris, M. Suzuki, T. E. Mallouk, J. Phys. Chem. A 2004, 108, 9115-9119.
[36] P. G. Hoertz, Y. Kim, W. J. Youngblood,T. E. Mallouk, J. Phys. Chem. B 2007, 111, 6845-6856.
[37] W. J. Youngblood, S.- H. A. Lee, Y. Kobayashi, E. A. Hernandez-Pagan, P. G. Hoertz, T. A. Moore, A. L. Moore, D. Gust, T. E. Mallouk, J. Am. Chem. Soc. 2009, 131, 926-927.
[38] B. O'Regan, M. Gräetzel, Nat. 1991, 353, 737-740.
[39] H. Dau, C. Limberg, T. Reier, M. Risch, S. Roggan, P. Strasser, ChemCatChem 2010, 2, 724-761.
[40] H. Dau, I. Zaharieva, Acc. Chem. Res. 2009, 42, 1861-1870.
[41] H. Inoue, T. Shimada, Y. Kou, Y. Nabetani, D. Masui, S. Takagi, H. Tachibana, ChemSusChem 2011, 4, 173-179.
[42] C. C. L. McCrory, S. Jung, I. M. Ferrer, S. M. Chatman, J. C. Peters, T. F. Jaramillo, J. Am. Chem. Soc. 2015, 137, 4347-4357.
[43] S. Trasatti, G. Lodi, "in electrodes of conductive metallic oxides" Elsevier 1981, 521-626.
[44] M. Risch, A. Grimaud, K. J. May, K. A. Stoerzinger, T. J. Chen, A. N. Mansour, Y. Shao-Horn, J. Phy. Chem. C 2013, 117, 8628-8635.
[45] A. Grimaud, C. E. Carlton, M. Risch, W. T. Hong, K. J. May, Y. Shao-Horn, J. Phy. Chem. C 2014, 117, 25926-25932.
[46] S. W. Lee, C. Carlton, M. Risch, Y. Surendranath, S. Chen, S. Furutsuki, A. Yamada, D. G. Nocera, Y. Shao-Horn, J. Am. Chem. Soc. 2012, 134, 16959-16962.
[47] J. Pfrommer, M. Lublow, A. Azapira, C. Göbel, M. Lücke, A. Steigert, M. Pogrzeba, P. W. Menezes, A. Fischer, T. Schedel-Niedrig, M. Driess, Angew. Chem. Int. 2014, 53, 5183-5187.
[48] D. M. Jang, I. H. Kwak, E. L. Kwon, C. S. Jung, H. S. Im, K. Park, J. Park, J. Phys. Chem. C 2015, 119, 1921-1927.
[49] L. Besra, M. Liu, Materials Science 2007, 52, 1-61.
[50] M. Ammam, RSC Advances 2012, 2, 7633-7646.
[51] F. Begona, M. Rodrigo, J. Eur. Ceram. Soc. 2010, 30, 1069-1078.
[52] I. Corni, M. P. Ryan, A. R. Boccaccini, J. Eur. Ceram. Soc. 2008, 28, 1353-1367.
[53] O. Van der Biest, L. J. Vandeperre, Annu. Rev. Mater. Sci. 1999, 29, 327-352.
[54] J. Tsukada, H. Zanin, L. C. A. Barbosa, G. A. da Silva, H. J. Ceragioli, A. C.

Peterlevitz, R. F. Teo'filo, V. Baranauskasa, J. Electro chem. Soc. 2012, 159, D159-D161.
[55] H. Wang, M. R. Shen, Z. Y. Ning, C. Ye, C. B. Cao, H. Y. Dang, H.S. Zhu, Appl. Phys. Lett. 1996, 69, 1074-1077.
[56] A. H. C. Sirk, D. R. Sadoway, J. Electrochem. Soc. 2008, 155, E49-E55. [57] Y. Namba, J. Vac. Sci. Technol. A 1992, 10, 3368-3370.
[58] B. Seger, S. D. Tilley, Th. Pedersen, P. C. K. Vesborg, O. Hansen, M. Grätzel, I. Chorkendorff, J. Mater. Chem. A, 2013,1, 15089-15094.
[59] J. E. Thorne, S. Li, C. Du, G. Qin, D. Wang, J. Phys. Chem. Lett. 2015, 6, 4083-4088.
[60] S. Avasthi, Y. Qi, G. K. Vertelov, J. Schwartz, A. Kahn, J. C. Sturm, Appl. Phys. Lett. 2010, 96, 222109-222111.
[61] R. Har-Lavan, O. Yaffe, P. Joshi, R. Kazaz, H. Cohen, D. Cahen, AIP Advances 2012, 2, 012164 .
[62] N.A. Allsop, A. Schönmann, A. Belaidi, H.-J. Muffler, B. Mertesacker, W. Bohne, E. Strub, J. Röhrich, M. C. Lux-Steiner, Ch.-H. Fischer, Thin Solid Films 2006, 513, 52-56.
[63] Ch. H. Fischer, N.A. Allsop, S.E. Gledhill, T. Köhler, M. Krüger, R. Sa'ez-Araoz, Y. Fu, R. Schwieger, J. Richter, P. Wohlfart, P. Bartsch, N. Lichtenberg, M. Ch. Lux-Steiner; Sol. Energy Mater. Sol. Cells 2011, 95, 1518-1526.
[64] X. Liao, X. Zhang, K. Takai, T. Enoki, J. Appl. Phys. 2010, 107, 013709.
[65] M. Ni, M. K. H. Leung, D. Y. C. Leung, K. Sumathy, Renewable and Sustainable Energy Reviews 2007, 11, 401-425.
[66] S. Licht, , B. Wang, S. Mukerji, T. Soga, M. Umeno, H. Tributsch, Int. J. Hydrogen Energy, 2001, 26, 653-659.
[67] G. Peharz, F. Dimroth and U. Wittstadt, Int. J. Hydrogen Energy, 2007, 32, 3248-3252.
[68] S. Hu, Ch. Xiang, S. Haussener, A. D. Bergercd, N. S. Lewis, Energy Environ. Sci., 2013, 6, 2984-2993.
[69] R. van de Krol, Y. Liang, J. Schoonman, J. Mater. Chem., 2008, 18, 2311-2320.
[70] P. Hillebrand, "Structure-function relationships of cobalt and manganese oxides as catalysts for (photo-) electrochemical water splitting", TU-Berlin 2015.
[71] W. Shockley, H. J. Queisser, J. Appl. Phys. 1961, 32, 510-519.
[72] K. S. Joy, y. F. Joya, K. Ocakoglu, R. V. de Krol, Angew. Chem. Int. Ed., 2013, 52, 10426-10437.
[73] J. Luo, J. H. Im, M. T. Mayer, M. Schreier, M. K. Nazeeruddin, N. G. Park, S. D. Tilley, H. J. Fan, M. Grätzel, Science, 2014, 345, 1593-1596.
[74] K. S. Joya, H. J. M. de Groot, ChemSusChem, 2014, 7, 73-76.
[75] R. Cao, W. Laia, P. Du, Energy Environ. Sci. 2012, 5, 8134-8157.
[76] M. G. Walter, E. L. Warren, J. R. McKone, S. W. Boettcher, Q. X. Mi, E. A. Santori, N. S. Lewis, Chem. Rev. 2010, 110, 6446-6473.
[77] A. C. Nielander, M. J. Bierman, N. Petrone, N. C. Strandwitz, S. Ardo, F. Yang, J. Hone, N. S. Lewis, J. Am. Chem. Soc. 2013, 135, 17246-17249.
[78] S. Hu, M. R. Shaner, J. A. Beardslee, M. Lichterman, B. S. Brunschwig, N. S. Lewis, Science 2014, 344, 1005-1009.
[79] D. G. Nocera, Acc. Chem. Res. 2012, 45, 767-776.
[80] B. Mei, B. Seger, T. Pedersen, M. Malizia, O. Hansen, I. Chorkendorff, P. C. K. Vesborg, J. Phys. Chem. Lett. 2014 5, 1948-1952.

[81] A. G. Scheuermann, J. D. Prange, M. Gunji, C. E. D. Chidsey, P. C. McIntyre, Energy Environ. Sci 2013, 6, 2487-2496.
[82] T. P. Luxton, M. J. Eick, K. G. Scheckel, J. Coll. Int. Sci. 2011, 359, 30-39.
[83] J. R. McKone, R. A. Potash, F. J. DiSalvoa , H. D. Abruña, Phys. Chem. Chem. Phys. 2015, 17, 13984-13991.
[84] M. Nose, T. Kinumoto, H. S. Choo, K. Miyazaki, T. Abe, Z. Ogumi, FUEL CELLS, 2009 9, 284-290.
[85] M. Schriver, W. Regan, W. J. Gannett, A. M. Zaniewski, M. F. Crommie, A. Zettl, ACS Nano 2013, 7, 5763-5768.
[86] J. Yang, D. Wang, H. Han, C. Li, Accounts of Chemical Research 2013, 1900-1909.
[87] H. Dotan, N. Mathews, T. Hisatomi, M. Grätzel, A. Rothschild; J. Phys. Chem. Lett. 2014, 5, 3330-3334.
[88] F. Lin, S.W. Boettcher, Nature material 2014, 13, 81-86.
[89] C. C. L. McCrory, S. Jung, J. C. Peters, Th. F. Jaramillo, J. Am. Chem. Soc. 2013, 135, 16977-16987.
[90] M. Grätzel Acc. Chem. Res. 1981, 14, 376-384.
[91] U. Kölle, New J. Chem. 1992, 16, 157-169.
[92] A. J. Bard, M. A. Fox, Acc. Chem. Res. 1995, 28, 141-145.
[93] J. A. Turner, Science 2004, 305, 972-974.
[94] N. S. Lewis, D. G. Nocera, Proc. Natl. Acad. Sci. U. S. A. 2006,103, 15729-15735.
[95] N. S. Lewis, Science 2007, 315, 798-801.
[96] G. W. Crabtree, M. S. Dresselhaus, MRS Bull. 2008, 33, 421-428.
[97] H. B. Gray, Nat. Chem. 2009, 1, 7-8.
[98] T. R. Cook, D. K. Dogutan, S. Y. Reece, Y. Surendranath, T. S. Teets, D. G. Nocera, Chem. Rev. 2010, 110, 6474-6502.
[99] D. J. Walton, L. D. Burke, M. M. Murphy, Electrochim. Acta 1996, 41, 2747-2751.
[100] E. Navarro-Flores, Z. Chong, S. Omanovic, J. Mol. Catal. A: Chem. 2005, 226, 179-197.
[101] C. Fan, D. L. Piron, P. Paradis, Electrochim. Acta 1994, 39, 2715-2722.
[102] N. V. Krstajic', V. D. Jovic', L. Gajic'-Krstajic', B. M. Jovic', A. L. Antozzi, G. N. Martelli, Int. J. Hydrogen Energy 2008, 33, 3676-3687.
[103] J. M. Spurgeon, J. M. Velazquez, M. T. McDowell, Phys. Chem. Chem. Phys. 2014, 16, 3623-3631.
[104] E. Tsuji, A. Imanishi, K.-i. Fukui, Y. Nakato, Electrochim. Acta 2011, 56, 2009-2016.
[105] I. C. Man, H. Y. Su, F. Calle-Vallejo, H. A. Hansen, J. I. Martinez, N. G. Inoglu, J. Kitchin, T. F. Jaramillo, J. K. Nørskov, J. Rossmeisl, J. ChemCatChem 2011, 3, 1159-1165.
[106] J. Rossmeisl, A. Logadottir, J. K. Nørskov, J. Chem. Phys. 2005, 319, 178-184.
[107] J. Rossmeisl, Z. W. Qu, H. Zhu, G. J. Kroes, J. K. Nørskov, J. Electroanal. Chem. 2007, 607, 83-89.
[108] M. T. M. Koper, J. Electroanal. Chem. 2011, 660, 254-260.
[109] M. Jayalakshmi, W. Y. Kim, K. D. Jung, O. S. Joo, Int. J. Electrochem. Sci. 2008, 3, 908-917.
[110] S. M. Sze, K. K. Ng, " Physics of Semiconductor Devices", John Wiley & Sons Inc. 1969.
[111] K. Rajeshwar,"Fundamentals of Semiconductor Electrochemistry and Photo-electrochemistry" Wiley-VCH 2007

[112] J. R. Mott, P. J. Munson, R. A. Kreuter, B. S. Chohan, D. G. Sykes, J. Chem. Educ., 2014, 91 (7), pp 1028-1036.
[113] B.V. Van Zeghbroeck, ”Principles of Semiconductor Devices and Heterojunctions” 2010.
[114] A. W. Bott,”Electrochemistry of semiconductor” 1998.
[115] A. Chiril’a, S. Buecheler, F. Pianezzi, P. Bloesch, Ch.Gretener, A. R. Uhl, C. Fella, L. Kranz, J.Perrenoud, S. Seyrling, R. Verma, S. Nishiwaki, Y. E. Romanyuk, G. Bilger , A. N. Tiwari, Nature Materials 2011, 10, 857-861.
[116] P. Jackson, D. Hariskos, R. Wuerz, O. Kiowski, A. Bauer, Th. M. Friedlmeier, M. Powalla, Phys. Status Solidi RRL 2015, 9, 28-31.
[117] C. A. Kaufmann, R. Caballero, T. Unold, R. Hesse, R. Klenk, S. Schorr, M. Nichterwitz, H. W. Schock, Solar Energy Materials & Solar Cells 2009, 93, 859-863.
[118] A. M. Gabor, J. R. Tuttle, M. H. Bode, A. Franz, A. L. Tennant, M. A. Contreras, R. Noufi, D. G. Jensen, A. M. Hermann, Sol. Energy Mater. Sol. Cells 1996, 41, 247-260.
[119] R.Noufi,Y.Yan,J.Abu-Shama,K.Jones, M.Al-Jassim,B.Keyes, J. Alleman, R. Ramanathan, Proc.29^{th} IEEE PVSC,NewOrleans, 2002, NREL/CP-520-31430.
[120] C. A. Kaufmann, A. Neisser, R. Klenk, R. Scheer, Thin Solid Films 2005, 480, 515-519.
[121] R. Hesse, J. R. K. Kamdoum, R. Caballero, Ch. A. Kaufmann, Ch. Stephan, S. Schorr, D. Abou-Ras, Th. Unold, H. W. Schock, Phys. Status Solidi C 2009, 6, 1249-1252.
[122] X. Wang, G. Liu, G. Q. Lu, H. M. Cheng, J. of hydrogen energy 2010, 35, 8199-8205.
[123] A. A. Keller, H. Wang, D. Zhou, H. S. Lenihan, G. Cherr, B. J. Cardinale, R. Miller, Z. Ji, Environ. Sci. Technol. 2010, 44 (6), pp 1962-1967.
[124] K. Hashimoto, H. Irie, A. Fujishima, Japanese Journal of Applied Physics 2005, 44, 8269-8285.
[125] D. O. Scanlon, Ch. W. Dunnill, J. Buckeridge, S. A. Shevlin, A. J. Logsdail, S. M. Woodley, C. R. A. Catlow, M. J. Powell, R. G. Palgrave, I. P. Parkin, G. W. Watson, Th. W. Keal, P. Sherwood, A. Walsh, A. A. Sokol, Nature Materials 2013, 12, 798-801.
[126] Ch. H. Liao, Ch. W. Huang, J. C. S. Wu, Catalysts 2012, 2, 490-516.
[127] A. B. Murphy, P. R. F. Barnes, L. K. Randeniya, I. C. Plumb, I. E. Grey, M. D. Horne, J. A. Glasscock, Int. J. Hydrogen Energy 2006, 31, 1999-2017.
[128] A. Zaleska, Recent Patents on Engineering 2008, 2, 157-164.
[129] M. Anpo, Pure & Appl. Chem 2000, 72, 1787-1792.
[130] A. Fuerte, M. D. Hernàndez-Alonso, A. J. Maira, A. Martìnez-Arias, M. Fernàndez-Garcìa, J. C. Conesaa , J. Soria, Chem. Commun. 2001, 24, 2718-2719.
[131] H . Yamashita, M. Harada, J. Misaka, J. Synchrotron Rad 2001, 8, 569-571.
[132] T. Ihara, M. Miyoshi, M. Ando, S. Sugihara, Y. Iriyama, J. Mater. Sci. 2001, 4201-4207.
[133] K. Takeuchi, I. Nakamura, O. Matsumoto, S. Sugihara, M. Ando, T. Ihara, Chem. Lett. 2000, 29, 1354-1355.
[134] T. Ohno, T. Mitsui, M. Matsumura, Chem Lett 2003, 32, 364-365.
[135] Y. Liu, X. Chen, J. Li, C. Burda, J. Chemosphere 2005, 61, 11-18.
[136] J. C. Yu, L. Zhang, Z. Zheng, J. Zhao, J. Chem Mater 2003, 15, 2280 -2286.
[137] C. Sotelo-Vazquez, N. Noor, A. Kafizas, R. Quesada-Cabrera, D. O. Scanlon, A. Taylor, J. R. Durrant, I. P. Parkin, J. Chem. Mater. 2015, 27 (9), 3234-3242.
[138] T. Hirai, K. Suzuki, I. Komasawa, J. Colloid Interface Sci. 2001, 244, 262-265.
[139] D. Chatterjee, A. Mahata, Appl. Catal. B Environ. 2001, 33, 119-125.

[140] J. Wang, T. Ma, G. Zhang, Catal Commun 2007, 8, 607-611.
[141] W. Zhou, Y. Zheng, G. Wu, Appl. Surf. Sci. 2006, 253, 1387-1392.
[142] C. Kittel, Introduction to Solid State Physics, John Wiley & Sons,ISBN : 978-0-471-41526-8
[143] YH. Lai, HS. Park , JZ. Zhang , PD. Matthews , DS. Wright , E. Reisner, Chemistry. 2015 Mar 2; 21(10): 3919-3923.
[144] Y. W. Chen, J. D. Prange, S. Dühnen, Y. Park, M. Gunji, Ch. E. D. Chidsey, P. C. McIntyre, Nature Materials 2011, 10,539-544.
[145] Zh. Xia, X. Zhou , J. Li ,Y. Qu, Sci. Bull. (2015) 60(16):1395-1402.
[146] R. E. Rocheleau, E. L. Miller, A. Misra, Energy & Fuels 1998, 12, 3-10.
[147] F.R.F. Fan, R.G. Keil, A.J. Bard, J. Am. Chem. Soc. 1983, 105, 220-224.
[148] F. R. F. Fan, G. A. Hope, A. J. Bard, J. Electrochem. Soc. 1982, 129, 1647-1649.
[149] J. J. H. Pijpers, M. T. Winkler, Y. Surendranath, T. Buonassisic, D. G. Nocera, Proc. Natl. Acad. Sci. USA 2011, 108, 10056-10061.
[150] E. R. Young, R. Costi, S. Paydavosi, Energy Environ. Sci. 2011, 4, 2058-2061.
[151] X. Li, W. Lu, W. Dong, Nanoscale 2013, 5, 5257-5261.
[152] W. Cui, Zh. Xia, Sh. Wu, F. Chen, Y. Li, B. Sun, ACS Appl Mater Interfaces 2015, ACS Appl. Mater. Interfacesdoi:10.1021/acsami. 5b01393.
[153] S. Polarz, A. V. Orlov, M. W. E. van den Berg, M. Driess, Angew. Chem. Int. 2005, 44, 7892-7896.
[154] M. L. Tong, S. L. Zheng, J. X. Shi, Y. X. Tong, H. K. Lee, X. M. Chen, Journal of the Chemical Society, Dalton Transactions 2002, 1727-1734.
[155] J. C. Cruz, V. Baglio, S. Siracusano, V. Antonucci, A. S. Aricò, R. Ornelas, L. Ortiz-Frade, Int. J. Electrochem. Sci. 2011, 6, 6607 - 6619.
[156] Deutsches Patent für ILGAR-Oxid-Schichten: Nr. 198 16 403.7 für ILGAR-Oxid-Schichten
[157] H.-J. Muffler, C.-H. Fischer, K. Diesner, M.C. Lux-Steiner, Solar Energy Materials and Solar Cells, 67 (1-4), 121-127.
[158] P. S. Patil, Materials Chemistry and Physics 1999, 59, 185-198.
[159] J. J. Van Tassel, C. A. Randall, Key Engineering Materials 2006, 314 , 167-174.
[160] H. C. Hamaker, Trans Faraday Soc. 1940, 36, 279-87.
[161] T. Ishihara, K. Shimise, T. Kudo, H. Nishiguchi, T. Akbay, Y. Takita, J. Am. Ceram. Soc. 2000, 83(8), 1921-1927.
[162] F. Chen, M. Liu, J Eur Ceram. Soc. 2001, 21, 127-134.
[163] M. von Smoluchowski, URN: urn:nbn:de:hebis:30-84830 .
[164] B. M. Haines, A. L. Mazzucato, arXiv.org 2011 arXiv:1104.1102.
[165] D. Andrienko ”Cyclic Voltammetry” 2008.
[166] A. P. Singh, S. Kumari, R. Shrivastav, S. Dass and V. R. Satsangi, J. Phys. D: Appl. Phys., 2009, 42, 085303-085308.
[167] S. Ashton, Springer Theses (2012), ISBN 978-3-642-30550-4.
[168] P. Bogdanoff, N. Alonso-Vante, J. Electroanal. Chem.1994, 379, 415-421.
[169] T. G. Mendes-de-Sa, A. M. B. Goncalves, M. J. S. Matos, P. M. Coelho, R. Magalhaes-Paniago, R. G. Lacerda, Nanotechnology 2012, 23, 475602-475610.
[170] Y. Waseda, E. Matsubara and K. Shinoda, ”X-ray diffraction crystallography”, Springer, 201, DOI 10.1007/978-3-642-16635-8.
[171] Y. Li, D. Lu, C.P. Wong, ”Electrical conductive adhesives with nanotechnolgies”, Springer 2010.
[172] L. Scudiero, ”X-Ray PhotoelectronSpectroscopy (XPS)-2”.

[173] T. Haile, ”Photoelectron Spectroscopy , XPS & UPS, Addis Ababa University, 2014”.

[174]http://www.gla.ac.uk/schools/ges/research/researchfacilities/isaac/ services/scanningelectronmicr

[175] Herzog, ”Ultra-thin inorganic nanocomposites for photovoltaic applications” 2008.

[176] L. Kronik, Y. Shapira, Surface Science reports 1999, 37, 1-206.

[177] B. Goldstein and D. Szostk, Surface Science, 1980, 99, 235-258.

[178] J. Lagowski, C. Balestra, H. Gatos, Surface Science 1971, 27, 547-558.

[179] T. Dittrich, S. Bonisch, P. Zabel and S. Dube, Rev. Sci. Instrum. 2008, 79, 113903.

[180] A. O. Juma, PhD thesis ”Copper diffusion in In_2S_3 and charged separation at In_2S_3/CuSCN and TiO_2/In_2S_3 interfaces” FU Berlin 2013.

[181] J. Domenech, A. Prieto, J. Phys. Chem. 1986, 90 (6), 1123-1126.

[182] F. Mesa, W. Chamorro, W. Vallejo, R. Baier, Th. Dittrich, A. Grimm, M. C. Lux-Steiner, S. Sadewasser, J. Nanotechnology 2012, 3, 277-284.

[183] A. Azarpira , M. Lublow , A. Steigert , P. Bogdanoff , D. Greiner , Ch. A. Kaufmann , M. Krüger , U. Gernert , R. van de Krol , A. Fischer, Th. Schedel-Niedrig, Adv. Energy Mater. 2015, 1402148.

[184] R. Caballero, Ch. A. Kaufmann, T. Eisenbarth, Th. Unold, R. Klenk, H. W. Schock, Prog. Photovolt: Res. Appl. 2011, 19, 547-551.

[185] J. Choi, H. Park, M. R. Hoffmann, J. Phys. Chem. C 2010, 114, 783-792.

[186] Due to the deposition temperature used for $Cu(In, Ga)Se_2$ deposition, it is expected, that a strong in-depth double Ga-gradient is present within the absorber layer. Hence for the cut-off energy correlates rather to the optical band gap of the $Cu(In, Ga)Se_2$ near the TiO_2/ $Cu(In, Ga)Se_2$ interface.

[187] S. W. Boettcher, E. L. Warren, M. C. Putnam, E. A. Santori, D. Turner-Evans, M. D. Kelzenberg, M. G. Walter, J. R. McKone, B. S. Brunschwig, H. A. Atwater, N. S. Lewis, J. Am. Chem. Soc. 2011, 133, 1216-1219.

[188] A. G. Muñoz, C. Heine, M. Lublow, H. W. Klemm, N. Szabò, T. Hannappel, H. J. Lewerenz, ECS Journal of Solid State Science and Technology, 2013, 2 (4) Q51-Q58.

[189] R. C. Kainthla, B. Zelenay, J. O’M. Bockris, J. Electrochem. Soc., 1987, 134, 841-845.

[190] M. J. Kenney, M. Gong, Y. Li, J. Z. Wu, J. Feng, M. Lanza, H. Dai, Science 2013, 342, 836-840.

[191] K. Sun, N. Park, Zh. Sun, J. Zhou, J. Wang, X. Pang, Sh. Shen, S. Y. Noh, Y. Jing, S. Jin, P.K. L. Yua, D. Wang, Energy Environ. Sci. 2012, 5, 7872-7877.

[192] H. J. Lewerenz, J. Electroanal. Chem. 1993, 356, 121-143.

[193] E. J. Nemanick, P. T. Hurley, L. J. Webb, D. W. Knapp, D. J. Michalak, B. S. Brunschwig, N. S. Lewis, J. Phys. Chem., 2006, 110, 14770-14778 .

[194] L. J. Webb, N. S. Lewis, J. Phys. Chem., 2003, 107, 5404-5412.

[195] K. T. Wong, N. S. Lewis, Acc. Chem. Res. 2014, 47, 3037-3044.

[196] A. Azarpira, J. Pfrommer, K. Olech, Ch. Höhn, M. Driess, B. Stannowski, Th. Schedel-Niedriga and M. Lublow, J. Mater. Chem. A DOI: 10.1039/c5ta07329d.

[197] A. Juma, J. Kavalakkatt, P. Pistor, B. Latzel, K. Schwarzburg, T. Dittrich, Phys. Status Solidi A, 2012, 209, 663-668.

[198] L. Macor, M. Gervaldo, F. Fungo, L. Otero, T. Dittrich, C. Y. Lin, L. C. Chi, F.-C. Fang, S.-W. Lii, C.-H. Tsai, C.-C. Wu, RCS Advances, 2012, 2, 4869-4878.

[199] M. C. Biesinger, B. P. Paynec, A. P. Grosvenord, L. M. Laua, A. R. Gersonb, R. St. C. Smart, Appl. Surf. Sci. 2011, 257, 2717.

[200] M. P. Seah, W. A. Dench, Surface and Interface Analysis 1, 2 (1979).

[201] S. Trasatti, J. Electroanal Chem. 1972, 39, 163, doi: 10.1016/ S0022-0728(72)80485-6.
[202] A. Azarpira, Th. Schedel-Niedrig, H. J. Lewerenz, M. Lublow (submited to J. Adv. Eng. Mat. 2015).
[203] T. Akaishi, K. Miyasaka, K. Ishikawa, H. Shirakawa, S. Ikeda, J. Pol. Sci., 1980, 18, 745-750.
[204] P. Robin, J. P. Puget, A. J. Epstein, Polymer, 1983, 24, 1558-1564.
[205] B. Xu, R. J. Madix, C. M. Friend, Phys. Chem. Chem. Phys., 2013, 15, 3179-3185.
[206] M. Aggour, K. Skorupska, T. Stempel Pereira, H. Jungblut, J. Grzanna, H. J. Lewerenz, J. Electrochem. Soc. 2007, 154, H794-H797.
[207] M. Lublow, B. Bouabadi, S. Kubala, Sol. En. Mat. & Sol. Cells, 2012, 107, 56-62.

7.2 List of figures

List of Figures

1.1 solar to hydrogen pathways. 1
2.1 Position of conduction and valence band minima, C_B and V_B, of semiconductors with respect to the thermodynamic potentials for H_2 and O_2 evolution, respectively [69]. 8
2.2 Different configurations of PEC cell. 9
2.3 Activity of Various catalysts for HER and OER in acidic and alkaline electrolytes. 10
2.4 Comparison of V_B and C_B positions of a metal, a semiconductor and an insulator[3]. 11
2.5 Schematic diagram of the energy levels of an n-type semiconductor (a) and a p-type semiconductor (b). 12
2.6 energy levels in (a) p-type semiconductor, (b) n-type semiconductor and (c) redox electrolyte [113]. 13
2.7 Effect of the energy levels of semiconductor and electrolyte on the band edges in the interior of an n-type (a,c) and a p-type (d,f) semiconductor upon contact formation [114]. 14
2.8 Ideal current-voltage behavior of an n-type semiconductor (a) and p-type semiconductor (b) under illumination (solid blue curve) and in the dark (dashed green curve). 15
2.9 behavior of (a) n-type semiconductor, (b) p-type semiconductor under illumination (solid blue curve) and with co-catalysts (dashed red curve). . 16
3.1 (a) Light and dark C-V curves for an ideal solar cell. (b) External quantum efficiency of CIGSe-based solar cell devices with layers with different Cu/(In+Ga) ratios. (c) SEM cross section of a CIGSe solar cell. (d) Schematic band diagram of a CIGS solar cell under zero-bias voltage [115]. 18
3.2 TiO_2 band alignment [126]. 19
4.1 Schematic of the Ion-Layer-Gas (ILGAR) set-up for deposition of TiO_2. . 24
4.2 Schematic of the EPD process. 25
4.3 Schematic illustration of the electrophoretic deposition (EPD) set-up. . . 26
4.4 Typical cyclic voltammogram where i_{pc} and i_{pa} show cathodic and anodic peak currents, respectively, for a reversible reaction [165]. 27
4.5 Schematic of the photoelectrochemical cell. 28
4.6 IPCE set up [3]. 29
4.7 Schematic of the Differential Electrochemical Mass Spectroscopy (DEMS) setup. 30
4.8 (a) X-ray diffraction in reflection mode. (b) Grazing incidence X-ray diffraction (GIXRD) mode. 31
4.9 comparison between UPS and XPS[170]. 32
4.10 Relation between electron binding energies and atomic number (Z)[173]. . 34
4.11 Interaction of the electron beam with a sample in SEM [174]. 35
4.12 (a) Kelvin probe mode and (b) Fixed capacitor mode. 38
5.1 Current-voltage behavior (a) TiO_2:ZnO/CdS/CIGSe (solid line) and ZnO/CdS /CIGSe (dashed line), (b) TiO_2:CdS/CIGSe (solid line) and CdS/CIGSe and (c) TiO_2:CIGSe (solid line), bare CIGSe (dashed line). 41

5.2 Grazing incidence X-ray diffraction (GIXRD) at 0.3° angle of incidence of ILGAR TiO_2 deposited on FTO at different deposition temperatures: 250°C (black curve), 350°C (red curve), 400°C (green curve) and 450°C (blue curve). 42
5.3 Surface photovoltage measurements: (a) Normalized SPV amplitude and (b) normalized SPV divided by photon flux for $TiO_2 : CIGSe$ samples prepared at different deposition temperatures: bare CIGSe (purple curve), 250°C (black curve), 350°C (red curve), 400°C (green curve) and 450°C (blue curve). 43
5.4 Effect of deposition temperature on the current-voltage behavior of the $TiO_2/Cu(In, Ga)Se_2$ photocathode: TiO_2 sprayed at (a) 250°C (blue curve), 350°C (red curve) and (b) 400°C (green curve), 450°C (orange curve). Electrolyte: 0.5 M H_2SO_4, pH0.3. Photoelectrodes were measured under near AM1.5 (100 mW/cm^2) conditions, with Pt as counter electrode and Ag/AgCl as reference electrode. 44
5.5 (a) Current-voltage behavior of undoped $TiO_2 : Cu(In, Ga)Se_2$ (black curve) and Pt-implemented $TiO_2 : Cu(In, Ga)Se_2$ devices. The best current-voltage behavior shows an anodically shifted onset potential at +230 mV (green curve); Electrolyte: 0.5 M H_2SO_4, pH0.3. Photoelectrodes were measured under near AM1.5 (100 mW/cm^2) conditions. . . . 45
5.6 Surface morphology (SEM, left) and Pt-distribution (TEM, right) of TiO_2 thin films on CIGSe supports upon increasing Pt concentrations. Characterization by SEM clearly shows an increase of the anatase crystallite size for incremented Pt concentrations. For 5 and 10 vol.%, agglomeration of Pt to nano-clusters is visible in the corresponding TEM images [183]. . . 47
5.7 Resistivity and thickness of undoped and Pt-doped TiO_2. 48
5.8 (a) Grazing incidence X-ray diffraction (GIXRD) at 0.3° angle of incidence of undoped ILGAR TiO_2 paste (black curve), 2 vol.% Pt doped TiO_2 (red curve) and 5 vol.% Pt doped TiO_2 (green curve). All films were prepared on CIGSe substrates. 48
5.9 X-ray photoelectron spectroscopy of the Pt4 core level for the 5 vol. % Pt-TiO_2 film [183]. 49
5.10 X-ray photoelectron spectroscopy of the Ti 2p (a), O 1s (b) and N 1s (c) signals measured for 5% Pt-doped TiO_2 on CIGSe [183]. 49
5.11 XPS analysis of the C 1s signal measured for 5% Pt-doped TiO_2 on CIGSe. (a) before electrochemistry, (b) after electrochemistry, (c) comparison of the C 1s signals in (a) and (b)[183]. 50
5.12 UV-VIS transmission (a) and reflection (b) of undoped and Pt-doped TiO_2/CIGSe(c) Determination of the optical band gap of undoped and Pt-doped TiO_2/CIGSe. 51
5.13 Surface photovoltage measurements (SPV): (a) Normalized SPV amplitude, in-phase (blue curves) and phase shifted by 90° signals (red curves) for commercial TiO_2 paste (b), undoped TiO_2 (c) and 5%Pt:doped TiO_2 (d) prepared by the ILGAR process. 53

5.14 Incident-photon-to-charge-carrier conversion efficiency (IPCE) data of four different Pt-doped $\mathsf{TiO_2{-}Cu(In,Ga)Se_2}$ heterojunctions. (a) green squares: 5 vol.% Pt; (b) red squares: 2 vol.% Pt; (c) blue squares: 10 vol.% Pt compared with the undoped $\mathsf{TiO_2 - Cu(In,Ga)Se_2}$ heterojunction photocathode (d) black squares. The IPCE data have been measured at -0.4 V vs. RHE. Electrolyte: 0.5 M $\mathsf{H_2SO_4}$, pH0.3 [183]. 54
5.15 Hydrogen evolution behavior of the most efficient Pt-implemented $\mathsf{TiO_2}$-$\mathsf{Cu(In,Ga)Se_2}$ photocathode under illumination (red curve) and in the dark (blue curve) detected by differential photoelectrochemical mass spectroscopy (DEMS). The inset shows the hydrogen evolution with respect to CV curves under illumination. Electrolyte: 0.5 M $\mathsf{H_2SO_4}$, pH0.3. 55
5.16 Current-voltage behavior of 5 vol.% Pt doped $\mathsf{TiO_2}$-$\mathsf{Cu(In,Ga)Se_2}$ composite photocathode devices in different electrolytes: $\mathsf{H_2SO_4}$ 0.5M pH 0.3 (green curve), KOH 1N pH 14 (blue curve) and KPi buffer phosphate solution pH7 (red curve). All measurements were carried out in a three-electrode mode vs. Ag/AgCl reference electrode. 56
5.17 Photocurrent density time behavior over 25 (20) hours of the most efficient Pt-doped $\mathsf{TiO_2/Cu(In,Ga)Se_2}$ heterojunction photocathode in electrolytes of pH0.3 (pH7). Photoelectrodes were measured under near AM1.5 (100 $\mathsf{mW/cm^2}$) conditions at the hydrogen reduction potential 0 V vs. RHE. The spikes correspond to light on/light-off in order to assess the dark current density in a short time of several minutes. 57
5.18 (a) and (b) SEM / EDX image of a low efficient sample, with formation of Pt clusters on the surface of a $\mathsf{Cu(In,Ga)Se_2}$, (c) SEM image of cross section of the sample, (d) the top view SEM image of the sample shows formation of an interface layer with Pt nanoparticles. 58
5.19 Band alignment of a p-semiconductor with a metal for different work function relations (a) $\Phi_m < \Phi_p$, (b) $\Phi_m > \Phi_p$ and (c) Proposed band alignment of the 5%Pt-doped $\mathsf{TiO_2 - Cu(In,Ga)Se_2}$ [183]. 58
5.20 Comparison of the current-voltage behavior of the undoped $\mathsf{TiO_2{-}Cu(In,Ga)Se_2}$ (black curve), $\mathsf{Pt : TiO_2 - Cu(In,Ga)Se_2}$ compsoite photocathode with $\mathsf{Pt : TiO_2{-}TiO_2(ALD){-}Cu(In,Ga)Se_2}$ sample. The best current-voltage behavior is observed for the sample with $\mathsf{TiO_2}$ (by ALD) interface layer and shows an anodically shifted onset potential at +400 mV (brown curve); Electrolyte: 0.5 M $\mathsf{H_2SO_4}$, pH0.3. Photoelectrodes were measured under near AM1.5 (100 mW/$\mathsf{cm^2}$) conditions. 59
5.21 (a) Effect of the organic solvent and the deposition time on the thickness and the density of the layers. (b) Role of the organic solvent on the electrophoretic mobility of ZnO:Co particles in the suspension [196]. . . . 63
5.22 Diagram of forces influencing the movement of the dispersed particle. . . 64
5.23 (a), (b) Effect of the organic solvent as a function of deposition time on the electrophoretic mobility and the zeta potential of the ZnO:Co particles [196]. 65
5.24 (a) Current voltage behavior of ZnO:Co prepared in different organic solvents ethanol (red line), acetone (blue line) and acetonitrile (green line) and deposited on FTO substrates. (b) Galvanostatic measurements of the layers corresponding to a current density of 1 $\mathsf{mAcm^{-2}}$. Electrolyte: KOH 1N. 67

5.25 Differential electrochemical mass spectroscopy (DEMS) measurements for O_2 evolution on ZnO:Co deposited on FTO, dissolved in acetonitrile (a) and ethanol (b). Electrolyte: KOH 1N. 68
5.26 Stability assessment of ZnO:Co, prepared from ethanol-containing suspensions, at pH14. For comparison, the rapid degradation of a bare FTO substrate is indicated. 69
5.27 optical characterization of ZnO:Co deposited on FTO substrates (a) Transmission spectra as a function of wavelength. 70
5.28 GIXRD diagram of ZnO:Co prepared in ethanol (red line), acetone (blue line) and acetonitrile (green line) (a) after electrophoretic deposition and (b) after electrochemical measurements. 71
5.29 EDX spectra of ZnO:Co deposited on FTO in acetonitrile (a), ethanol (b) and acetone (c) before and after electrochemistry measurements. 72
5.30 XPS analysis of Co 2p signal (a) before electrochemistry for samples prepared in acetone (blue curve), acetonitrile (green curve) and ethanol (red). (b) XPS results for the Co 2p signal for acetone prepared sample before and after electrochemistry (c) and (d) comparative deconvolution of the Co 2p and Zn 2p signals for samples prepared in acetone and ethanol, respectively.[196]. 72
5.31 Microscopy characterization of ZnO:Co morphologies after EPD using acetonitrile as solvent. (a) and (b) SEM surface view before and after electrochemistry, respectively. (c) and (d) corresponding TEM images of ZnO:Co lamellae before and after electrochemistry, respectively. (e) and (f) Magnified TEM images of ZnO:Co lamellae before and after electrochemistry, respectively [196]. 75
5.32 Microscopy characterization of ZnO:Co morphologies after EPD using acetone as solvent. (a) and (b) SEM surface view before and after electrochemistry, respectively. (c) and (d) corresponding TEM images of ZnO:Co lamellae before and after electrochemistry, respectively. (e) and (f) Magnified TEM images of ZnO:Co lamellae before and after electrochemistry, respectively [196]. 76
5.33 Microscopy characterization of ZnO:Co morphologies after EPD using ethanol as solvent. (a) and (b) SEM surface view before and after electrochemistry, respectively. (c) and (d) corresponding TEM images of ZnO:Co lamellae before and after electrochemistry, respectively. (e) and (f) Magnified TEM images of ZnO:Co lamellae before and after electrochemistry, respectively [196]. 77
5.34 Schematic setup of the combined supports, an amorphous/microcrystalline silicon solar cell (bottom) and a ZnO:Co/FTO heterojunction (top). In the top-view, the O-ring is depicted in decreased size in order to stress the photoactive area beneath. 78
5.35 (a) Photocurrent-voltage behavior of the silicon triple-junction solar cell (black curve) and the stacking configuration with a top ZnO:Co/FTO layer, prepared from ethanol (red curve). (b) Corresponding stacking configurations with ZnO:Co/FTO layers prepared from acetone (green curve) and acetonitrile (black curve). For comparison the solar cell behavior without electrocatalysts is shown in red [196]. 79

5.36 (a) Current-voltage behavior of ethanol (red curve), acetone (blue curve) and acetonitrile (green curve) prepared samples in H_2SO_4 0.5 M. (b) Effect of the organic solvent on the thickness and the density of the layers. (c) Role of the organic solvent on the electrophoretic mobility of RuO_2 particles in the suspension. 80
5.37 (a-c) Current-voltage behavior of ethanol (red curve), acetone (blue curve) and acetonitrile (green curve) prepared samples. Dashed lines refer to FTO substrates, solid lines to the corresponding behavior for silicon substrates. (d-f) corresponding XPS analysis of the carbon C 1s signal [202]. 81
5.38 (a) TEM image of Si/Carbon/RuO_2, (b) SEM image of a particle-free region (resolution 100 nm) and (c) EDX mapping of a Si/RuO_2 edge [202]. 82
5.39 Device scheme and interfaces of Si/SiO_2/Carbon(sp^3)/Carbon (sp^2)/RuO_2. 83
5.40 Photocurrent-voltage behavior of Si(100) in 0.5 M H_2SO_4 after electrochemical surface conditioning in ethanol and ethanol-iodine, respectively. 84
5.41 XPS C 1s, Si 2p and I 3d signals of Si(100) after electrochemical surface conditioning in ethanol-iodine [202]. 84
5.42 UPS analysis of the cut-off region of secondary electrons of (a) H-terminated silicon and (b) ethanol-iodine-prepared silicon. 85
5.43 XPS analysis of the Ru 3d and C 1s core-level signals of (a) RuO_2 powder after physical adsorption from aqueous particle suspensions onto silicon and (b) RuO_2 deposited for 30 min onto silicon from ethanol-iodine containing suspensions. The C 1s deconvoluted signals and UPS analysis of the cut-off region of secondary electrons of each case are shown below [202]. 86
5.44 XPS analysis of the Ru 3d and C 1s core-level signals and UPS analysis of RuO_2 deposited for 60 min onto silicon from ethanol-iodine containing suspensions [202]. 87
5.45 FTIR analysis of the used solutions, ethanol (red), ethanol/iodine after electrochemistry (blue) and ethanol/iodine/RuO_2 after electrochemistry (green). 87
5.46 XPS Iodine I 3d analysis after deposition from ethanol- (a/b), acetone- (c) and acetonitrile- (d) iodine suspensions of RuO_2. 88
5.47 XRD analysis of Si/RuO_2, prepared from ethanol-iodine containing suspensions before (blue) and after annealing (red). 89
5.48 Operation of the Si/SiO_2/RuO_2 electrode for photo-assisted water splitting. (a) The photocurrent-voltage behavior is shown for two different distributions of RuO_2 particles. (b) Constant potential measurements in 0.5M H_2SO_4 under illumination (AM1.5)[202]. 90
5.49 Comparative surface and IPCE analysis of Si/RuO_2 after deposition from ethanol-iodine containing suspensions with (red) and without toluene addition (blue). SEM surface analysis (upper images) confirms that addition of toluene results in particle aggregation with an overall more scattered distribution. 92
5.50 XPS analysis of the Ru 3d and C 1s core-level signals of Si/RuO_2 after deposition for 30 min onto silicon from ethanol-toluene-iodine containing suspensions [202]. 92
5.51 Scheme for the RuO_2-catalyzed formation of an organic interface. 93
5.52 Differential electrochemical mass spectroscopy (DEMS) measurements for O_2 evolution on RuO_2/ n-Si photoanode, electrolyte H_2SO_4 0.5 M. . . . 93

5.53 (a) current-voltage behavior of $\mathsf{RuO_2}$/Si photoanode in $\mathsf{H_2SO_4}$ (red), Kpi pH7 (green) and KOH pH14 (blue). (b) Constant potential measurements of the photoanodes in the corresponding electrolytes. 94
5.54 Operation of the $\mathsf{Si/SiO_2/RuO_2}$ electrode as photoelectrochemical solar cell: In (a), two-electrode measurements in a iodide/triiodide electrolyte are shown using a Pt-counter electrode. The sensitive electrolyte was purged by nitrogen during both current-voltage cycling and long-time assessment of the short-circuit photocurrent (b). 95
5.55 SEM surface analysis of the Si photoelectrochemical solar cell. 96

7.3 List of publications

1. *Efficient and Stable* $\mathsf{TiO_2}$*:Pt-*$\mathsf{Cu(In,Ga)Se_2}$ *Composite Photoelectrodes for Visible Light Driven Hydrogen Evolution*

   Anahita Azarpira, Michael Lublow, Alexander Steigert, Peter Bogdanoff, Dieter Greiner, Christian A. Kaufmann, Martin Krüger, Ullrich Gernert, Roel van de Krol, Anna Fischer, Thomas Schedel-Niedrig (Adv. Eng. Mat. 2015, 1402148)

2. *Optimized immobilization of ZnO:Co electrocatalysts realizes 5% efficiency in photoassisted splitting of water*

   Anahita Azarpira, Johannes Pfrommer, Katarzyna Olech, Christian Höhn, Matthias Driess, Bernd Stannowski, Thomas Schedel-Niedriga and Michael Lublow, J. Mater. Chem. A (DOI: 10.1039/c5ta07329d)

3. *Sustained Water Oxidation by Direct Electrosynthesis of Ultrathin Organic Protection Films on Silicon*

   Anahita Azarpira, Thomas Schedel-Niedrig, Hans Joachim Lewerenz, Michael Lublow (revised manuscript submitted to Adv. En. Mat. 2015)

4. *Solvolytically prepared Ni:ZnO from heterobimetallic precursors as precatalysts for highly efficient and prolonged water oxidation catalysis*

   Johannes Pfrommer, Anahita Azarpira, Kasia Olech, Alexander Steigert, Thomas Schedel-Niedrig, Matthias Driess (manuscript submitted to Angewandte Chemie 2015)

5. *A Molecular Approach to Self-Supported Cobalt Substituted ZnO Materials as Remarkably Stable Electrocatalysts for Water Oxidation*

   Johannes Pfrommer, Michael Lublow, Anahita Azarpira, Caren Göbel, Marcel Lücke, Alexander Steigert, Martin Pogrzeba, Prash-anth W. Menezes, Anna Fischer, Thomas Schedel-Niedrig, Matthias Driess (Angewandte Chemie 53, 20, 5183-5187 (2014))

6. D*evelopment of Silicon-Supported ZnO:Co Heterojunctions for Photo-Assisted Water Splitting*

   Michael Lublow, Anna Fischer, Johannes Pfrommer, Anahita Azarpira, Alexander Steigert, Thomas Schedel-Niedrig, Matthias Driess (to be submitted)

7. *Novel electrocatalytic protection layers for photoassisted evolution of oxygen: carbonaceous transition-metal hydroxide films on silicon*

   Michael Lublow, I. Zaharieva, M. Driess, A. Azarpira, Th. Schedel-Niedrig, H. Dau, A. Fischer (to be submitted)

7.4 Patents

1. Verfahren zur Herstellung von photoelektrokatalytischen Elektroden aus industriellen Pigment-Pulvern TUB 1322 : M. Lublow, A. Azarpira, T. Schedel-Niedrig, A. Fischer, A. Azarpira, M. Dreiss, M. Kanis
   (Status: submitted to the Deutsches Patent und Markenamt (2015), in discussion with the patent examiner.)
2. Anorganisch-organische Mehrschicht-Photoelektrode für die solare Energieumwandlung HZB 2015-1: Lublow, Azarpira, Schedel-Niedrig
   (Status: in preparation with HZB experts for intellectual property rights. Envisaged submission date: February 2016.)
3. Verfahren zur Herstellung polymerartiger Schutzschichten auf Halbleiteroberflächen HZB 2015-2: Lublow, Azarpira, Schedel-Niedrig
   (Status: in preparation with HZB experts for intellectual property rights. Envisaged submission date: February 2016.)

7.5 Conference contributions

1. MRS Spring Meeting 2015, April 2015 in San Francisco
2. NanoGe Solar Fuel15, March 2015 in Mallorca
3. DFG Projekttreffen, September 2014 in Darmstadt
4. IPS 20, Juli 2014 in Berlin
5. E-MRS Spring Meeting 2014, Mai 2014 in Lille
6. DFG Projekttreffen, Oktober 2013 in Ellwangen

7.6 Curriculum Vitae

Personal Information

Name: Anahita Azarpira

Nationality: Iranian

Date of Birth: 10 September 1982

Education:

Technical University of Berlin (TU-Berlin) from March. 2013
"PhD student"
Place: Berlin, Germany
Thesis title: Synthesis and Characterization of Novel Composite Photoelectrodes based on Chalcopyrite and Silicon for the Visible Light-driven Hydrogen and Oxygen Evolution

Technical University of Berlin (TU-Berlin) Sep. 2010-Nov. 2012
"Master of Global Production Engineering in Solar Energy Engineering"
Place: Berlin, Germany
Thesis title: Proof of concept of ultra-thin nanocomposite solar cells based on nanoporous TiO_2 and sulfide (In_2S_3, Sb_2S_3) absorbers

Tehran University Sep. 2006-Feb. 2009
"Master of Chemical Engineering in Catalysis"
Place: Tehran, Iran
Thesis title: CFD modeling of slurry bubble column reactor

Iran university of science & Technology Sep. 2001-July 2006
"Bachelor of Chemical Engineering in Oil & Gas Process Design"
Place: Tehran, Iran
Thesis title: Modeling of FT synthesis by MATLAB

Nyayesh Highschool Sep. 1997 - July 2000
Place: Tehran, Iran
Title: Mathematics-Physics

Work Experience:

Helmholtz Zentrum Berlin March 2012-present
Place: Berlin, Germany
Title of Position: PhD student

Helmholtz Zentrum Berlin May 2012-November 2012
Place: Berlin, Germany
Title of Position: Master student

GFE Gesellschaft für Energieeffizienz mbH October 2011-February 2012
Place: Berlin, Germany
Title of Position: internship

Parsikan Iran Consultant Engineers Co. 2009-2010
Place: Tehran, Iran
Title of Position: Safety Engineer / Process Senior Engineer
(Client: Iranian Oil Pipeline and Telecommunication Co.)

Faranegar Sanaat Design & Engineering Co. 2008 - 2009
Place: Tehran, Iran
Title of Position: Process Senior Engineer (Client: Iranian Petrochemical Co.)